# POLITECNICO DI TORINO
# GRENOBLE-INP PHELMA
# EPFL

**Master's Degree in Nanotechnologies for ICT's**

**Master's Degree Thesis**

# DUV lithography for UHF resonator


**Supervisors**

**Prof. Guillermo VILLANUEVA**

**Prof. Carlo RICCIARDI**

**Marco LIFFREDO**

**Candidate**

**Federico PERETTI**


**February-August 2022**

# Summary

The key concept related to the most impressive advancement in terms of technology in the recent past is related to the concept of miniaturization. In fact, scaling down the device dimensions, it is possible to explore many different additional application respect to the macro scale. This possibility has led to the realization of Microelectromechanical systems (MEMS) and Nanoelectromechanical systems (NEMS) which corresponds to devices whose dimensions are, respectively, in the micron or nanometer range. These kind of devices are not only smaller, they often exhibit better performances or allow additional opportunity compared to their bigger counterparts. These reasons explain why MEMS are capturing the research effort in many field such as automotive, medical, communications defense and aerospace. Putting the focus on the communication market, it is in strong development due to growing need of high connectivity, fast exchange and quantity of data. Part of this market is represented by the RF-MEMS based front-end which have been proposed with the aim to target at the same time: low power consumption, small size and a CMOS compatible system so that is possible to have an easy integration with the rest of the circuitry. The central element in the RF-MEMS front-end is represented by piezoelectric MEMS resonators that are mainly employed for the realization for filters and oscillators. In this category, among other researches, contour mode resonators (CMRs) represent a significant field of study since they allow to modify the working frequency by design with a single lithographic step.

In this thesis, starting from the work already done by the supervisor Marco Liffredo and the CMRs knowledge present in the ANEMS Lab, the goal is to develop a new generations of CMRs able to reach the 5G frequency range up to 4GHz (the generation already fabricated works around 150MHz). To achieve that result, the impact of the most important design parameters have been investigated. First of all a preliminary set of 2D simulations have been performed to get as much information as possible without a heavy computational cost. Then a further set of 3D simulations have been done to analyze the missing parameters and obtain a model affordable enough to be considered for the development of a new layout. Since to increase the resonance frequency of the devices is required to scale down

the critical dimension and because of the purpose of the device itself, which target the batch fabrication for front-end application, the ASML PAS 5500/350C DUV stepper has been selected as lithographic tool. Hence the process flow have been modified to allow the use of that machine and to fulfil the new design requirements. To prove the effectiveness of these changes, some fabrication test where performed and finally, once concluded, the stepper reticle have been written. This last step has been performed in CMi through direct laser writing exploiting the Heidelberg Instruments VPG200 tool.

**Sommario**

Negli ultimi anni, il concetto chiave legato agli avanzamenti tecnologici più significativi è legato all'idea di miniaturizzazione. Infatti, riducendo le dimensioni di un dispositivo è possibile esplorare una vasta scala di applicazioni aggiuntive rispetto alla macroscala. Questa possibilità ha portato alla realizzazione di Microelectromechanical systems (MEMS) and Nanoelectromechanical systems (NEMS) che corrispondono a dispositivi le cui dimensioni sono rispettivamente, nella scala micrometrica e nanometrica. Questi dispositivi, non solo sono più piccoli, ma permettono maggiori opportunità rispetto alle loro più grandi controparti. I precedenti motivi spiegano perchè i MEMS stanno attirando interesse scientifico in svariati campi come automobilistico, medico, di comunicazione, difesa e aerospazio. Analizzando il mercato delle comunicazioni, si riscontra un forte sviluppo a causa del crescente bisogno di altà connettività e rapidi scambi di dati in grande quantità. Parte di questo mercato è rappresentato dai front-end basati su RF-MEMS che sono stati proposti con lo scopo di fornire al tempo stesso: bassi consumi di potenza, piccole dimensioni e compatibilità con i CMOS in modo tale da essere facilmente integrabili con il resto dei circuiti. L'elemento centrale nei front-end basati su RF-MEMS è rappresentato dai risonatori piezoelettrici che sono principalmente impiegati per la realizzazione di filtri e oscillatori. In questa categoria, tra gli altri, i "Contour mode resonator" (CMRs) sono tra i più studiati in ambito di ricerca in quanto permettono di modificare la frequenza di risonanza con un semplice processo litografico. In questa tesi, partendo dal lavoro già realizzato da Marco Liffredo e dalla conoscenza su questi dispositivi precedentemente acquisita nel laboratorio ANEMS, ci si pone l'obbiettivo di sviluppare una nuova generazione di CMRs capace di raggiungere il range di frequenza del 5G fino a 4GHz (la generazione precenedtemente fabbricata funziona attorno a 150MHz). Per raggiungere questo risultato è stato studiato l'impatto dei parametri di design più importanti. Prima di tutto, una serie di simulazioni 2D è stata effettuata per ottenere più informazioni possibili senza la necessità di un elevato costo computazionale. Successivamente, un'ulteriore serie di analisi 3D è stata effettuata in modo da analizzare i parametri mancanti e ottenere un modello abbastanza preciso da poter essere utilizzato per lo sviluppo di un layout. Siccome per aumentare la frequenza di risonanza è necessario ridurre le

dimensioni critiche per i processi litografici, e a causa del dispositivo stesso, che punta ad essere prodotto in parallelo, lo stepper DUV ASML PAS 5500/350C è stato selezionato come strumento litografico. Pertanto, il processo di produzione è stato modificato in modo da soddisfare i requisiti del nuovo design e dello stepper. Per verificare l'efficacia di questi cambiamenti, alcuni test di fabbricazione sono stati effettuati e, una volta conclusi, il reticolo è stato scritto. Quest'ultimo processo è stato svolto nel CMi attraverso una scrittura diretta a laser per sfruttando la macchina "Heidelberg Instruments VPG200".

**Sommaire**
Ces dernières années, le concept clé lié aux avancées technologiques les plus significatives est lié à l'idée de miniaturisation. En effet, en réduisant la taille d'un dispositif, il est possible d'explorer une grande échelle d'applications en plus de la macro-échelle. Cette possibilité a conduit à la création de systèmes microélectromécaniques (MEMS) et de systèmes nanoélectromécaniques (NEMS) qui correspondent à des dispositifs dont les dimensions sont respectivement à l'échelle du micromètre et du nanomètre. Ces appareils sont non seulement plus petits, mais offrent plus de possibilités que leurs homologues plus grands.Les raisons précédentes expliquent pourquoi les MEMS suscitent l'intérêt scientifique dans divers domaines tels que l'automobile, le médical, la communication, la défense et l'aérospatiale. En analysant le marché des communications, il y a un fort développement en raison du besoin croissant de connectivité élevée et d'échanges rapides de données en grandes quantités. Une partie de ce marché est représentée par les frontend basés sur RF-MEMS qui ont été proposés dans le but d'offrir à la fois : une faible consommation d'énergie, une petite taille et une compatibilité avec CMOS de manière à être facilement intégrés avec le circuits de repos. L'élément central des frontend RF-MEMS est représenté par les résonateurs piézoélectriques qui sont principalement utilisés pour la réalisation de filtres et d'oscillateurs. Dans cette catégorie, entre autres, les « Résonateurs en mode Contour » (CMR) sont parmi les plus étudiés dans le domaine de la recherche car ils permettent de modifier la fréquence de résonance par un simple procédé lithographique. Dans cette thèse, à partir des travaux déjà réalisés par Marco Liffredo et des connaissances sur ces dispositifs précédemment acquises au laboratoire ANEMS, l'objectif est de développer une nouvelle génération de CMRs capables d'atteindre la gamme de fréquences de la 5G jusqu'à 4GHz ( la génération précédemment fabriquée fonctionne autour de 150 MHz). Pour arriver à ce résultat, l'impact des paramètres de conception les plus importants a été étudié. Tout d'abord, une série de simulations 2D ont été réalisées pour obtenir le plus d'informations possible sans nécessiter un coût de calcul élevé. Par la suite, une nouvelle série d'analyses 3D a été réalisée afin d'analyser les paramètres manquants et d'obtenir un modèle suffisamment précis pour être utilisé pour l'élaboration d'un aménagement. Comme les dimensions critiques des processus lithographiques

doivent être réduites pour augmenter la fréquence de résonance, et en raison du dispositif lui-même, qui vise à être produit en parallèle, le stepper DUV ASML PAS 5500/350C a été sélectionné comme outil lithographique. Par conséquent, le processus de fabrication a été modifié pour répondre aux exigences de la nouvelle conception et du stepper. Pour vérifier l'efficacité de ces modifications, des tests de fabrication ont été effectués et, une fois conclus, le treillis a été écrit. Ce dernier procédé a été réalisé au CMi par une écriture laser directe pour exploiter la machine "Heidelberg Instruments VPG200".

# Acknowledgements

First of all, I would like to thanks my supervisor Marco Liffredo for his availability, support, numerous advice and for sustaining me in every step of the project. I would like to express my gratitude also to professor Guillermo Villanueva who gave me this great opportunity and precious help in all the critical steps. Besides my supervisors, I would like to thank all the people in the ANEMS staff who welcomed me in the lab and gave me precious tips. Among these a particular thanks goes to the PhD student Silvan Stettler for his help in part of the simulations. I also wanted to express gratitude to the CMi staff, especially to Niccolo Piacentini and joffrey Pernollet for sharing their knowledge and for their great availability. Last, but not least, I would like to thanks my family and my friends who supported me along this experience.

# Table of Contents


**List of Tables** X

**List of Figures** XI

**Acronyms** XVI

**1 Introduction and state of art** 1
- 1.1 Introduction to RF MEMS . . . . . . . . . . . . . . . . . . . . . . . . . . 1
- 1.2 State of the art . . . . . . . . . . . . . . . . . . . . . . . . . . 4
  - 1.2.1 Thin film bulk acoustic wave resonator . . . . . . . . . . . . 4
  - 1.2.2 Contour mode resonator . . . . . . . . . . . . . . . . . . . . 6
  - 1.2.3 FBAR vs CMRs . . . . . . . . . . . . . . . . . . . . . . . . 11
- 1.3 Figures of merit . . . . . . . . . . . . . . . . . . . . . . . . . . 12
  - 1.3.1 Quality factor . . . . . . . . . . . . . . . . . . . . . . . . 12
  - 1.3.2 Electromechanical coupling . . . . . . . . . . . . . . . . . . 14
  - 1.3.3 Spurious modes . . . . . . . . . . . . . . . . . . . . . . . . 14
- 1.4 Research areas . . . . . . . . . . . . . . . . . . . . . . . . . . 15
  - 1.4.1 Aluminum scandium nitride . . . . . . . . . . . . . . . . . . 15
  - 1.4.2 DUV lithography . . . . . . . . . . . . . . . . . . . . . . . . 16

**2 2D Simulations** 19
- 2.1 Reference model . . . . . . . . . . . . . . . . . . . . . . . . . . 19
- 2.2 Resonator width analysis . . . . . . . . . . . . . . . . . . . . . . 22
  - 2.2.1 Modes analysis . . . . . . . . . . . . . . . . . . . . . . . . 23
- 2.3 Spurious analysis in 2D . . . . . . . . . . . . . . . . . . . . . . 28
  - 2.3.1 Spurious mode versus electrode size . . . . . . . . . . . . . . 28
  - 2.3.2 Electrode spacers . . . . . . . . . . . . . . . . . . . . . . . 29
  - 2.3.3 Spurious modes and size of the resonator . . . . . . . . . . . 32
  - 2.3.4 Spurious modes vs pitch . . . . . . . . . . . . . . . . . . . . 34
  - 2.3.5 Periodic model . . . . . . . . . . . . . . . . . . . . . . . . 36
- 2.4 Cross sectional Lamè mode resonator . . . . . . . . . . . . . . . . 38

2.4.1 Band diagram study for CLRM . . . . . . . . . . . . . . . . 39
2.4.2 CLMR and $k_t^2$ optimization . . . . . . . . . . . . . . . . . . 41
2.4.3 $k_t^2$ vs electrical coverage . . . . . . . . . . . . . . . . . . . . 44

**3 3D Simulations** **46**
3.1 Simulation matching . . . . . . . . . . . . . . . . . . . . . . . . 46
3.2 Transverse spurious modes . . . . . . . . . . . . . . . . . . . . . 48
3.3 Design considerations and n28 band . . . . . . . . . . . . . . . . 50
3.3.1 Materials for electrodes . . . . . . . . . . . . . . . . . . . . 51
3.3.2 Admittance of the n28 band . . . . . . . . . . . . . . . . . . 52
3.4 Piston mode design . . . . . . . . . . . . . . . . . . . . . . . . . 53
3.4.1 Piston implementation . . . . . . . . . . . . . . . . . . . . . 55
3.4.2 Holes in the gap . . . . . . . . . . . . . . . . . . . . . . . . . 57

**4 Fabrication** **60**
4.1 Process flow . . . . . . . . . . . . . . . . . . . . . . . . . . . . . 60
4.2 Trench filling test . . . . . . . . . . . . . . . . . . . . . . . . . . 62
4.2.1 Step in the test . . . . . . . . . . . . . . . . . . . . . . . . . 62
4.2.2 SEM analysis of the sample . . . . . . . . . . . . . . . . . . . 64
4.3 AlScN IBE etch test . . . . . . . . . . . . . . . . . . . . . . . . . 67
4.3.1 Test description and results . . . . . . . . . . . . . . . . . . 68
4.3.2 IBE etching with hard mask . . . . . . . . . . . . . . . . . . 71

**5 Layout development and reticle fabrication** **74**
5.1 Device cell & device choices . . . . . . . . . . . . . . . . . . . . 74
5.2 Layout cells . . . . . . . . . . . . . . . . . . . . . . . . . . . . . . 78
5.2.1 Primary cell . . . . . . . . . . . . . . . . . . . . . . . . . . . 78
5.2.2 Test cell . . . . . . . . . . . . . . . . . . . . . . . . . . . . . . 79
5.2.3 Final layout . . . . . . . . . . . . . . . . . . . . . . . . . . . . 80
5.3 Reticle fabrication . . . . . . . . . . . . . . . . . . . . . . . . . . 81
5.3.1 Mask test . . . . . . . . . . . . . . . . . . . . . . . . . . . . . 82
5.3.2 Final result . . . . . . . . . . . . . . . . . . . . . . . . . . . . 86

**6 Conclusions** **87**
6.1 Future improvements . . . . . . . . . . . . . . . . . . . . . . . . . 88

**Bibliography** **90**

# List of Tables


1.1 Comparison between FBAR and CMRs. . . . . . . . . . . . . . . . . . 11

3.1 Comparison between Platinum and Alluminum properties[15] . . . . 51

# List of Figures


1.1 Data consumption from 2017 to 2022[3] . . . . . . . . . . . . . . . . . 2
1.2 Typical structure of an FBAR[9] . . . . . . . . . . . . . . . . . . . . . . 4
1.3 Wave propagating in FBAR device[10]. . . . . . . . . . . . . . . . . . 5
1.4 CMR electrodes configurations in TFE(a) and LFE(b) configuration. Electric potential and the amplitude of the displacement are represented respectively in white and black[8] . . . . . . . . . . . . 7
1.5 SEM image of a contour mode resonator [8] . . . . . . . . . . . . . . 8
1.6 SEM image of a 1-port resonator in LTE configuration(a) and modified BVD model for 1 port devices(b) [8] . . . . . . . . . . . . . . . 9
1.7 Typical $Y_{11}$ measurement of a 1-port LTE device [8]. . . . . . . . . 10
1.8 Piezoelectric response behaviour of AlScN depending on Scandium percentage [23] . . . . . . . . . . . . . . . . . . . . . . . . . . . . . 16
1.9 Typical structure of a DUV stepper [25] . . . . . . . . . . . . . . . 17

2.1 Geometry of the reference model for 2D simulations . . . . . . . . . 20
2.2 Admittance $Y_{11}$ vs frequency plot of the reference model. . . . . . . 21
2.3 Mode shape (displacement in x component) for S0 mode (a) and spurious modes (b). Here only the one at 157.7MHz is reported since the other (128MHz) exhibit the same shape with a lower amplitude of displacement. . . . . . . . . . . . . . . . . . . . . . . . . . . . . 21
2.4 Admittance $Y_{11}$[S] varying the Width of the resonator with fixed electrical boundaries . . . . . . . . . . . . . . . . . . . . . . . . . . 22
2.5 Peak $Y_{11}$ admittance at the resonance frequency compared to the resonator width (a) and electormechanical coupling $k_t^2$ behaviour with respect to the resonator width (b). . . . . . . . . . . . . . . . 23
2.6 Admittance Y11[S] of 3 nodes modes at different widths (a), x component of the displacement in the reference model (b), x component of the displacement considering respectively $W_{res}$ of $80\mu m$ and $100\mu m$. 24

2.7 Displacement in x direction for reference model (a), $W_{res} = 80\mu m$ (b) and $W_{res} = 105\mu m$. In image (d) is represented the admittance of the 3 nodes mode for the reference model($W_{res} = 60\mu m$) versus the 5 nodes mode with $W_{res} = 105\mu m$. . . . . . . . . . . . . . . . . . 25
2.8 Admittance $Y_{11}$ [S] of 5 nodes mode at $W_{res} = 69\mu m$ and of 7-node mode at $W_{res} = 100\mu m$ . . . . . . . . . . . . . . . . . . . . . . . . 27
2.9 Mode shape (displacement in x component) of the 5-nodes mode $W_{res} = 69\mu m$ (a) and of 7-node mode at $W_{res} = 100\mu m$ (b) . . . . . 27
2.10 Admittance response [S] varying the width of the electrodes at a constant pitch. EC range between 0.95 and 0.5 on the left, EC range between 0.5 and 0.05 on the right. . . . . . . . . . . . . . . . . . . . . 29
2.11 2D geometry of the resonator with the addition of the spacers . . . 30
2.12 Admittance response versus frequency performing a sweep of the spacer thickness . . . . . . . . . . . . . . . . . . . . . . . . . . . 30
2.13 Admittance $Y_{11}$ plot, showing the behaviour of the higher frequency spurious mode(respect to the resonance) increasing the spacer thickness 31
2.14 Admittance $Y_{11}$, showing the behaviour of the lower frequency spurious mode(respect to the resonance) increasing the spacer thickness . 31
2.15 Mode shape along x axis for reference model(a) with 3 fingers and for larger resonator with 19 fingers(b) (S and G represent respectively the number of signal and ground fingers). Admittance plot versus frequency of the 3 fingers (c) and 19 fingers resonator(d). . . . . . . 33
2.16 Admittance vs frequency graphs with $W_{res} = 60\mu m$ with $P = 20\mu m$ (a), $P \approx 6.67\mu m$ (b), $P \approx 2.86\mu m$ and $P \approx 2.1\mu m$. . . . . . . . . . 35
2.17 Admittance vs frequency graphs with addition of spacers having $W_{res} = 60\mu m$ and $P \approx 6.67\mu m$ (a), and $P \approx 2.1\mu m$ . . . . . . . . . 35
2.18 Geometry and mode shape at resonance (displacement in x direction) of periodic model for pitch $P = 2\mu m$. . . . . . . . . . . . . . . . . . 36
2.19 Geometry and mode shape at resonance (displacement in x direction) of periodic model for pitch $P = 2\mu m$. . . . . . . . . . . . . . . . . . 37
2.20 Phase velocity versus $T_{AlScN}/\lambda_x$ for AlN CMR [29]. . . . . . . . . . 39
2.21 Phase velocity (P*$f_{res}$) vs $T_{AlScN}/\lambda_x$ ratio in AlScN resonator (left) and shape of the S0 mode (right). . . . . . . . . . . . . . . . . . . 40
2.22 Displacement in x direction of CMR (left) and CLMR (right). . . . 40
2.23 Displacement along the x direction for $P = 750\mu m$ . . . . . . . . . 41
2.24 Electromechanical coupling behaviour respect to $T_{AlScN}/\lambda_x$ ratio for S0 mode in AlN resonators for different configuration of metal fingers [28]. . . . . . . . . . . . . . . . . . . . . . . . . . . . . . 42
2.25 $k_t^2$ vs number of fingers with $W_res = 60\mu m$ and $T_{AlScN} = 500nm$. . 43
2.26 Displacement along x direction for $P = 850nm$ and a $T_{AlScN}/\lambda_x$ ratio equal to 0.294. . . . . . . . . . . . . . . . . . . . . . . . . . 43

2.27 Behaviour of $k_t^2$ respect to the electric coverage for $P = 880nm$ . . . 44

3.1 Image of the previously fabricated device at the optical microscope. 46
3.2 Admittance comparison of 2D, 3D and 3D periodic models. . . . . 47
3.3 Schematic image of a CMR resonator with 3 fingers . . . . . . . . . 48
3.4 Admittance plot for different $L_{active}$ ($W_a = L_{active}$)[30]. . . . . . . . 49
3.5 Admittance plot of the described resonator . . . . . . . . . . . . . 52
3.6 Admittance plot of the model designed for n78 band ($P = 4.5\mu m$) . 52
3.7 Velocity $\nu$ and displacement $u_x$ profile without (left) and with piston mode (right)[30] . . . . . . . . . . . . . . . . . . . . . . . . . . 54
3.8 2D periodic cell with piston representing the correct mode shape (left) and transverse wave vector (real part) vs frequency with main mode highlighted (right). . . . . . . . . . . . . . . . . . . . . . . . 55
3.9 2D periodic cell with gap representing the correct mode shape (left) and transverse wave vector (imaginary part) vs frequency with main mode highlighted (right). . . . . . . . . . . . . . . . . . . . . . . . 56
3.10 Qualitative representation of the results obtained from the band diagrams. (Note that for the gap the imaginary part instead of the real one has been plotted. . . . . . . . . . . . . . . . . . . . . . . 56
3.11 Admittance $Y_{11}$ plot of the device for band n28 9 ($P = 4.5\mu m$) with the addition of pistons ($L_p = 11.5\mu m$) . . . . . . . . . . . . . . . 57
3.12 Edge of the cell of a n28 band resonator with a 500nm hole in the gap. In blue are represented the metal parts(Al) whereas in grey the piezoelectric ones . . . . . . . . . . . . . . . . . . . . . . . . 58
3.13 Two different cases of waveguide junctions: the first one (a) can be associated to long holes in the gap, whereas the second one (B) to short holes.[33] . . . . . . . . . . . . . . . . . . . . . . . . . . . 58
3.14 Admittance response vs frequency of the n28 band devices ($P = 4.5\mu m$) with the introduction of the gap in the hole . . . . . . 59

4.1 Main steps for the fabrication of the LTE CMRs. . . . . . . . . . . 61
4.2 Main steps for the trench filling test . . . . . . . . . . . . . . . . . 63
4.3 Test layout for the trench filling test (positive polarity). . . . . . . . 64
4.4 SEM image of the group of the smallest test cells . . . . . . . . . . 65
4.5 SEM image of the bottom part of one the smallest cells. . . . . . . 65
4.6 SEM image of the higher part of one the smallest cells. . . . . . . . 66
4.7 Modification of the steps to solve the clogging issue. . . . . . . . . . 67
4.8 Reticle chip for IBE etch test.[26] . . . . . . . . . . . . . . . . . . . 68
4.9 SEM image of the $5\mu m$ apertures after 620s of medium power IBE. 69
4.10 SEM image of the $1\mu m$ apertures after 620s of medium power IBE. 70

4.11 SEM image of the $5\mu m$ apertures after 18 minutes of medium power IBE. . . . . . . . . . 71
4.12 SEM image of the $5\mu m$ apertures after 20 minutes of medium power IBE on silicon with Hard mask protection. . . . . . . . . . 72

5.1 Lithographic steps required in the reticle. . . . . . . . . . 75
5.2 Example of a n28 band cell layout . . . . . . . . . . 75
5.3 N28 band cell layout with separate layers. . . . . . . . . . 76
5.4 Zoom on a n28 band device with layers 1), 4), 5), 6) of figure 5.3. . 77
5.5 Primary cell with "big" pitches on the left and "small" ones on the right. Note that each colour correspond to a different image on the reticle. . . . . . . . . . 79
5.6 Test cell representation. Note that each colour correspond to a different image on the reticle. . . . . . . . . . 80
5.7 Final image of the layout. Note that here the layers have not been separated due to L-edit representation issue . . . . . . . . . . 81
5.8 Process for reticle fabrication.[26] . . . . . . . . . . 82
5.9 SEM image of fingers ($P = 500nm$) with optimal dose (7.5). . . . . 83
5.10 SEM image of gap hole in the openings layer (dose 7.5). . . . . . . . 84
5.11 SEM image of the release area confinement (Dose=7.5). . . . . . . . 84
5.12 SEM image of fingers with pistons (Dose=7.5) having $P = 4.5\mu m$ (top) and $P = 1\mu m$ (bottom). . . . . . . . . . 85
5.13 Image of the Fabricated reticle. . . . . . . . . . 86

# Acronyms

**AlN**

Aluminum nitride

**AlScN**

Aluminum scandium nitride

**BAW**

Bulk acoustic wave

**BHF**

Buffered hydrofluoric acid

**BVD**

Buttherworth-Van Dyke

**CMi**

Center of microtechnology

**CMRs**

Contour mode resonators

**CLMR**

Cross sectional Lamè mode resonators

**DF**

Defocus

**DOF**

Depth of focus

**DUV**

Deep ultra violet

**FBAR**

Thin-film Bulk acoustic wave resonator

**FoM**

Figures of merit

**IBE**

Integrated circuits

**IC**

Ion beam etching

**KrF**

Krypton fluoride

**LFE**

Lateral field excitation

**MEMS**

Micro electromechanical systems

**MPL**

Maskless lithography

**NA**

Network analyzer

**NEMS**

NANO electromechanical systems

**OPC**

Optical proximity corrections

**SAW**

Surface acoustic wave

**SEM**

Scanning electron microscope

**TFE**

Thickness field excitation

**TTV**

Total thickness variation

**UV**

Ultra violet

# Chapter 1

# Introduction and state of art

## 1.1 Introduction to RF MEMS

In the recent years the world is becoming more and more interconnected, therefore the need of multiple and fast communications is growing rapidly. To fulfill this requirements and to simplify our lives, the amount of technology around us is quickly increasing. The final goal of this trend is to create network of devices and sensors able to do task now done by human being. In this context the role of MEMS (microelectromechanical systems) is growing in terms of importance. Analyzing the Yole technology report of 2021 [1] it is possible to see how these kind of devices are covering a wide area of applications, spacing from Health-care to automotive and 5G communications. Following Yole predictions, the MEMS market is going to reach 18.2 billion of revenue forecasting 7.2% of CAGR in 2026[1]. The reason of this diffusion is linked to the advantages associated to this kind of devices. In fact, they exhibit: low power consumption, small form factor (which allow an easy integration with other component) and mass production possibility that makes them cost-effective. Despite these awesome qualities that puts them in the condition to substitute many older devices, a significant work is still required for their improvement. The peak in terms of performances is not reached yet and fabrication processes are still under improvement. This situation induces so an increase in terms of cost and decrease the reproducibility of the devices. Hence an intense research is on going to explore their full potentiality.[2]

Among the MEMS based devices the biggest slice of market is devoted to the RF MEMS.[1] An important factor which took to this result is related to the huge increase in terms of data consumption which, as it is possible to see from the image 1.1, has been growth by a factor of seven in the last six years[3]. This huge amount of data induced a strong development in terms of communication velocity leading

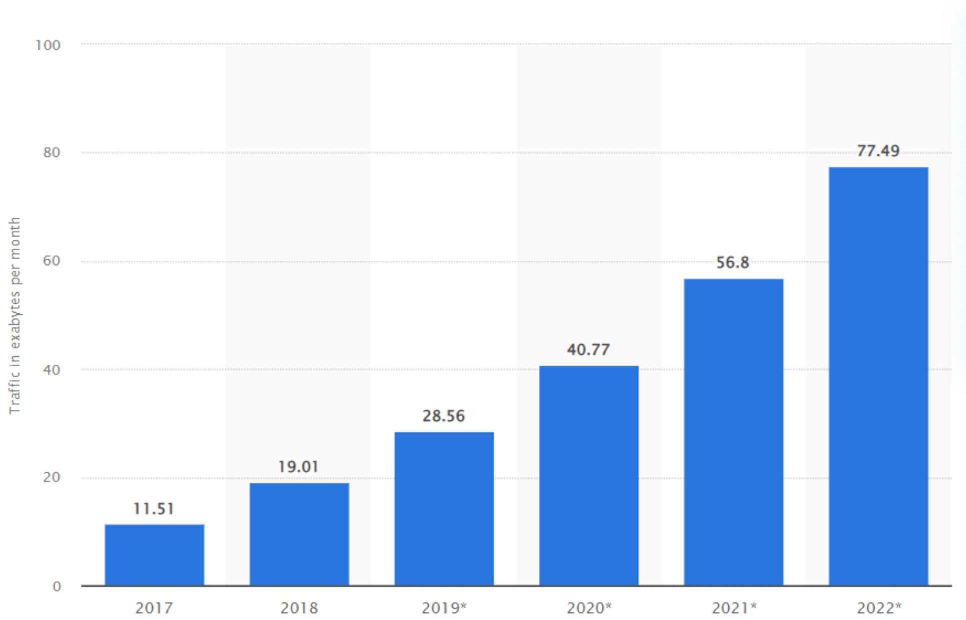


**Figure 1.1:** Data consumption from 2017 to 2022[3]

to the realization of 4G and 5G. These new technologies have required the addition of multiple new bands and other filter-intensive solutions. This factor, in parallel with the extremely rapid diffusion of smartphones, has exponentially increased the number of needed filters as well as their number per chip and with them, the complexity of the device strengthening so the boundaries related to size and power consumption. For these reasons, the old ceramic filters, despite their high quality factor and $kt^2$ (these figures of merit will be explained in the following sections), had to be gradually substituted along the years by Piezoelectric MEMS solutions due to their big dimension in the millimeter range which is not compatible with such evolution of the technology.[4] Moreover, several piezoelectic MEMS present the advantage of being on chip component, allowing so a much easier integration with the already developed circuitry in the market and reducing so the number of trade off which have been done by the designers.

In this context the market requirements have been mainly satisfied by two different typology of devices: surface acoustic wave devices (SAW), and bulk acoustic wave devices (BAW). The first one has been developed many years ago and so is a well established technology. It is made by many metallic interdigitated fingers (working as transducer) lying over a piezoelectric substrate. Applying an alternate voltage to the metal is possible to easily excite a shear wave in the piezo (the motion of the atoms is perpendicular respect to the surface). Those devices, being fabricated with a single lithographic step, are cheap and have the advantage of allowing the integration of many different frequencies on the same chip. This aspect can be underestimated but is a crucial considering the growing complexity of the RF front end. Unfortunately it is difficult to work at high frequencies with this kind of devices since the power density exhibit a cubic growth respect to the frequency making the SAW not reliable at high frequencies. Hence the SAW devices are typically used up to 2GHz and are so not really suitable for the new 5G applications[4][5]. Over this frequency the BAW become the most employed choice. These devices are typically composed by a piezoelectric material deposited between two electrodes. In this configuration it is possible to excite longitudinal waves (the motion of the atoms is in the same direction of the energy transfer) that, exhibiting a higher phase velocity respect to shear waves, allow to relax the power density constraints. The drawback of this kind of devices is represented by the cost, since a more complex fabrication process that can reach more than 20 steps is needed, and by the more complex integration of many frequencies on the same chip. On the other hand BAW are IC compatible and more stable in temperature. Moreover, this devices are designed to reduce the losses related to the excitation of other mode in the substrate showing so an higher Q factor respect to SAW.[4] Two main typology of BAW are present and chosen depending on the specifications. The film bulk acoustic resonator (FBAR) being suspended structure allows to enhance the Q at the cost of less power dissipation capability[6], whereas, the solidly mounted resonator BAW (SMR-BAW) are directly attached to the substrate allowing a better power dissipation but, despite the contact with the substrate is made through an alternation of oxide and metal which constitute a bragg reflector, the losses are higher and the Q lower.[7] This device choice flexibility (SMR-BAW or FBAR) linked to the offered performances and the IC compatibility has made the BAW based devices one of the main players in the 5G race. However the goal is represented by the realization of a RF front end where a single resonator is employed for frequency timing and control. A promising solution currently under study is represented by contour mode resonators CMRs (the structure of the device will be accurately described in the next section). This kind of device is in fact able to guarantee at the same time IC compatibility and the possibility to easily tune the working frequency by design. These two properties are crucial in the evolution of the RF front end since they allow a change respect the currently used architecture inducing a reduction in terms of system complexity, cost and size.[8]

## 1.2 State of the art

The aim of this section is to analyze the contour mode resonator. First of all the a brief introduction of the FBAR, which is its main competitor in the market, is presented, then its principle of working, characteristics and potentiality are explained. To completely understand the comparison, an explanation on the main figures of merit have been performed. Finally, an FBAR vs CMRs comparison is performed focusing on why CMRs is an interesting option and where it is still necessary to make improvements.

### 1.2.1 Thin film bulk acoustic wave resonator

The thin film bulk acoustic wave resonator (FBAR) is one of the most employed typology of RF piezoelectric MEMS. In fact, thanks to its reduced dimension, good performances and easy tunable resonance frequency in the 100MHz-20GHz range, it was able to replace crystal oscillators, crystal filters and to partially substitute SAW devices becoming widely used in the RF front end of modern smartphones [9]. Many different typologies of FBAR are produced slightly changing depending on the fabrication process, but their structure can be resumed in figure 1.2:

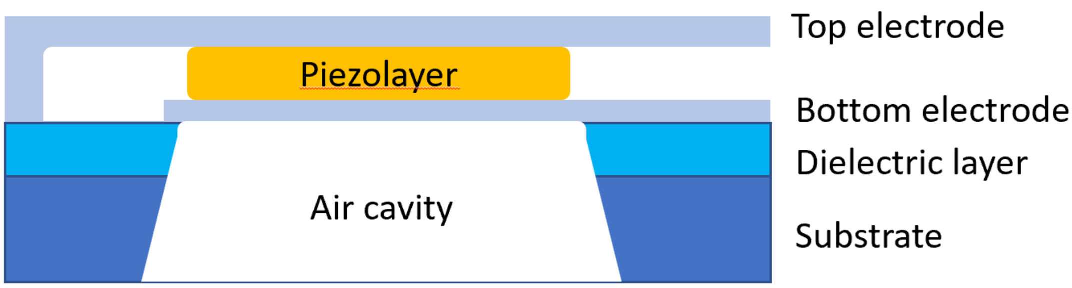


**Figure 1.2:** Typical structure of an FBAR[9]

The core of the structure is represented by the piezoelectric layer deposited between two metal electrodes. If correctly oriented, it allow to exploit the piezoelectric coefficient $d_{33}$ to excite a longitudinal acoustic wave through the application of an AC signal between the two electrodes. To electrically insulate the structure from the substrate, below the bottom electrode, one or more dielectric layer are present. Another crucial characteristic which differentiate the FBAR from the SMR-BAW is represented by the acoustic insulation. In fact, if in the latter the insulation is performed through a bragg reflector made by the alternation of many layers, in FBAR the same function is performed by an air cavity [10]. For this reason, FBAR exhibit a higher quality factor at a cost of a lower power dissipation capability.

This last characteristic make FBAR in competition with other suspended structure such as CMRs that exhibit similar performances. Concerning the excited acoustic wave, as it is possible to see in figure 1.3, it propagates along the vertical direction and it is associated to the thickness of the device.

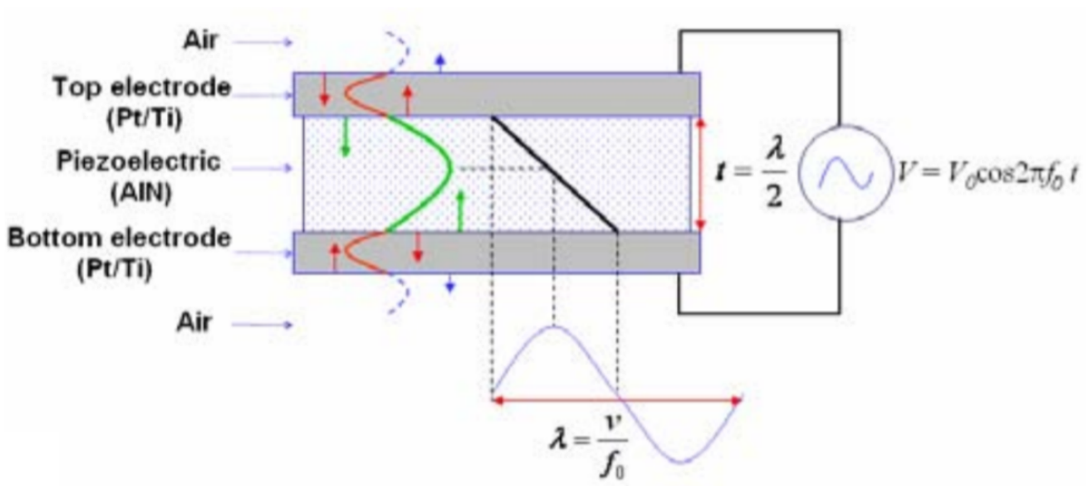


**Figure 1.3:** Wave propagating in FBAR device[10].

In fact at the resonance frequency $f_0$ (as stated in [10]) the frequency can be expressed as:

$$f_0 = \frac{\nu}{2t} \tag{1.1}$$

Where $\nu$ is the phase velocity and t the thickness of the device. Observing the formula it is possible to notice that the thickness of the device corresponds to the half of the wavelength at the resonance frequency. Hence, being at the resonance, this represent the optimal condition for the energy confinement and, at the same time, it provide an easy way to define the working frequency of the device. In fact, the simplicity in the resonance frequency selection for the FBAR comes from its possibility to be tuned by modifying the piezoelectric layer thickness. This fact constitute a great advantage since, a variation in the deposition time, does not constitute a problem for the fabrication but, at the same time, it is a limitation because of the difficulty to integrate different frequency (and so thickness) on the same chip. To do that, it is necessary to increase the fabrication complexity by performing ion milling or mass loading steps [9]. To overcome this issue, that in the context of exponentially growing number of device per chip cannot be underestimated, some other solutions such as CMRs are currently under research.

### 1.2.2 Contour mode resonator

A promising class of MEMS currently under research is constituted by the contour mode resonators also known as Lamb wave resonator (from the name of the excited mode). As previously mentioned this kind of resonators has the potentiality to replace SAW devices since it does not exhibit the same power dissipation issues and, at the same time, allow an easy integration on the same device because, differently from BAW, the working frequency isn't determined by the thickness of the piezoelectric layer allowing multiples frequencies on the same chip[11] . In this way, linking the two properties, it is possible to relax the complexity of the architecture in the RF front end. To schematize, the main advantages of this devices are:

- Easy tunability of the resonance frequency on a single chip in MHz and GHz range by design
- Low motional resistance
- High Q factor also in air
- Parasitic capacitance values below the pF range.
- CMOS compatibility

This specifications are promising for the RF front end both for the realizations of filters and oscillators. Concerning the latter the CMR constitute a good module for frequency selection, since, because of their possibility to reach a Q factor over 1000 in air, allow a good frequency stability [12]. For filtering applications, the crucial property is represented by the possibility to modify the motional resistance by design and set it to 50Ω which is the reference value matched with the other circuitry. Regarding the structure, the device consists in a piezoelectric layer sandwiched between two metal layers. Thanks to the application of a given AC voltage, and consequently of an electric field perpendicularly respect to the piezoelectric layer, it is possible, through the inverse piezoelectric effect, to induce a mechanical deformation exploiting the piezoelectric coefficient $d_{31}$. This physical phenomena result in the excitation of the lateral mode of the resonator (so called since the strain is perpendicular respect to the vertical applied electric field) that, being named "contour" gives the name to this class of resonator. As it is possible to see in figure 1.4 there are two different configuration which allow to excite the chosen mode known as "Thickness field excitation" (TFE) and "Lateral field excitation" (LFE). In both cases the metal electrodes on the top of the structure are disposed to form interdigitated (IDT) fingers. It is important to notice that adjacent fingers must be connected to opposite polarities to correctly excite the contour mode. The difference between the two structures consists instead in the bottom metal which, in the LFE is a uniform floating metal layer, whereas in the TFE resonator constitute another series on interdigitated fingers put at the same x and y coordinate respect to the one on top but with opposite voltage applied.

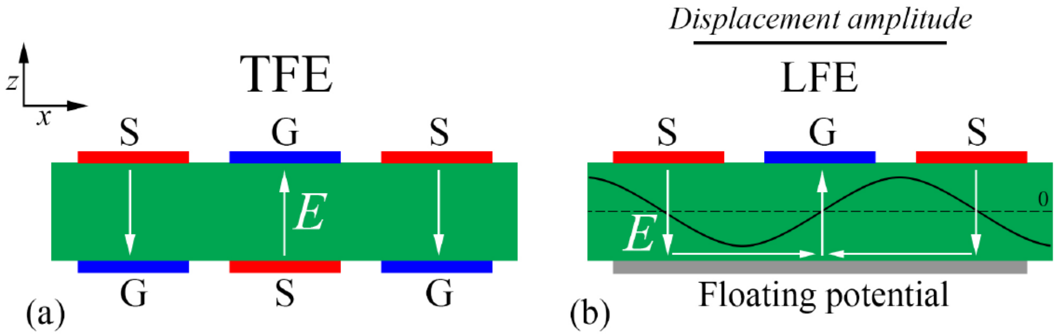


**Figure 1.4:** CMR electrodes configurations in TFE(a) and LFE(b) configuration. Electric potential and the amplitude of the displacement are represented respectively in white and black[8]

Despite this variation in the structure both these configuration allow to excite the contour mode but with some differences. In fact, having electrodes with opposite polarities one over the other, in TFE configuration the direction of the electric field is defined with stronger boundaries, resulting in a better excitation of the piezoelectric material. This lead to a stronger electromechanic coupling (see "figures of merit" section) and consequently to a slightly lower motional resistance if compared to the correspondent LFE. Moreover thanks to the lower amount of metal on the bottom (which is typically characterized by a lower sound velocity respect to the piezoelectric material), TFE CMR typically exhibit also a blue shift in terms of resonance frequencies.[13] The cost of these advantages is balanced by higher difficulties in terms of fabrication. In fact, due to the presence of many discontinuities, the deposition of the piezoelectric element over the bottom metal is more challenging due to the irregularity of the surface.[14] Besides this fact, an additional lithographic step is also required for the routing of the signal. Finally the restrictions in terms of alignment are more stringent because of the need to vertically align bottom and top electrodes [8]. For those reasons, the LFE is often preferred since the improvement aren't enough satisfying to justify the increasing fabrication effort. Hence, if not specified, from now on LTE will be considered inside of this document.
To give a possible idea about the global 3D structure and to show and clarify the name of the main parameters, an example of a CMR resonator previously realized in the NEMS lab, is presented in figure 1.5. Where resL (or $L_{res}$) represent the total length of the resonator, $L_a$ and $W_a$ stands respectively for length and width of

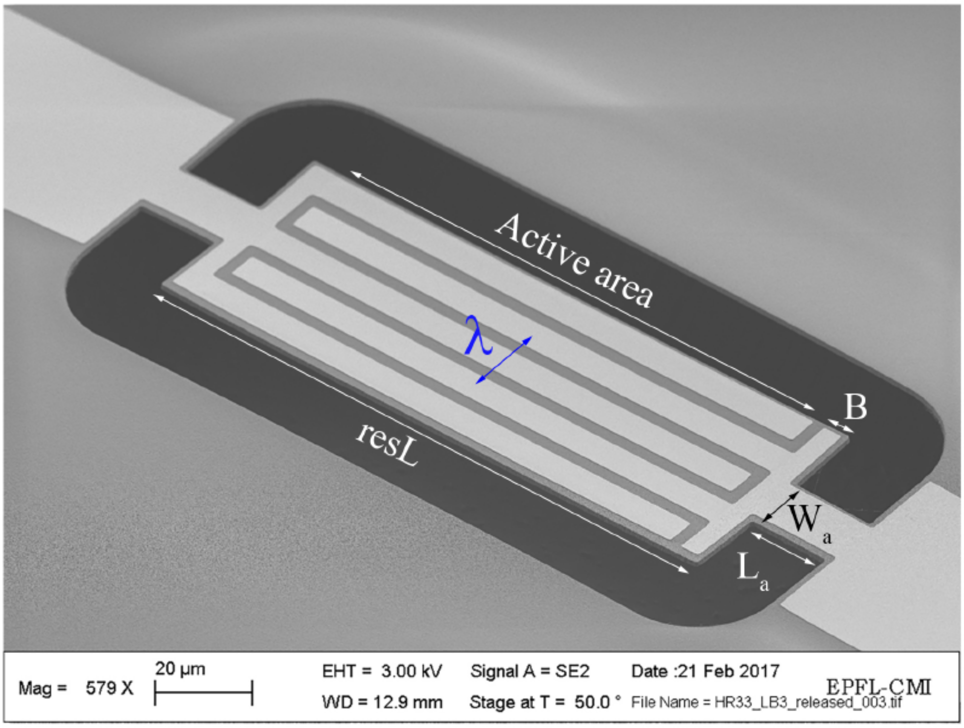


**Figure 1.5:** SEM image of a contour mode resonator [8]

the anchor, B is the bus which connect the fingers and $\lambda$ is the electrical wavelength used to excite the resonator. This latter parameter is important to explain why in this typology of resonators it is possible to integrate multiple frequency on the same chip. In fact, differently from BAW, the distance between the middle of the electrodes, which is called pitch (P) and is equal to half of the wavelength, can set the resonance frequency:

$$f_{res} = \frac{\nu_{S0}}{\lambda} = \sqrt{\frac{E_{eq}}{\rho_{eq}}} \cdot \frac{1}{2P} \tag{1.2}$$

Where $\nu_{S0}$ is the acoustic phase velocity associated to the S0 mode in a given material ("S" represent the typology of the mode which in this formula means "symmetric" whereas "0" indicate the order and in this particular case the fundamental one), $\lambda$ is the wavelength, P is the pitch and $E_{eq}$ and $\rho_{eq}$ stands for equivalent young modulus and density of the resonator and represent the effective value coming from the combinations of E and $\rho$ of the various materials constituting the resonator [15]. Once the materials are fixed, being the elasticity module (E) and the density ($\rho$) intrinsic properties of the materials, it is possible to modify the pitch (P) to consequently vary the working frequency of the resonator. Hence, by properly tuning, accordingly to the pitch, the others geometrical parameters it is possible to have a full control on the resonance frequency in the limit offered by the fabrication tools. Depending on the measurement needs, with a similar fabrication processes, it is possible to realize one or two port devices however, since this project is orientated for filter fabrication, only the 1-port devices will be considered. This kind of device constitute the simplest model and is visible in figure 1.6(a). In this configuration a reflection measurement is performed. In fact, here the fingers on top of the resonator, which are used to provide the excitation of the piezoelectric layer through an electric field, are at the same time exploited for the readout. This is possible since the second port is shorted, representing a perfectly reflective boundary in the acoustic domain. The electrical equivalent of this structure can be realized through a modified version of the Butterworth-Van Dike (BVD) model presented in figure 1.6 (b): This model is constituted by a motional branch containing $R_m$, $L_m$ and

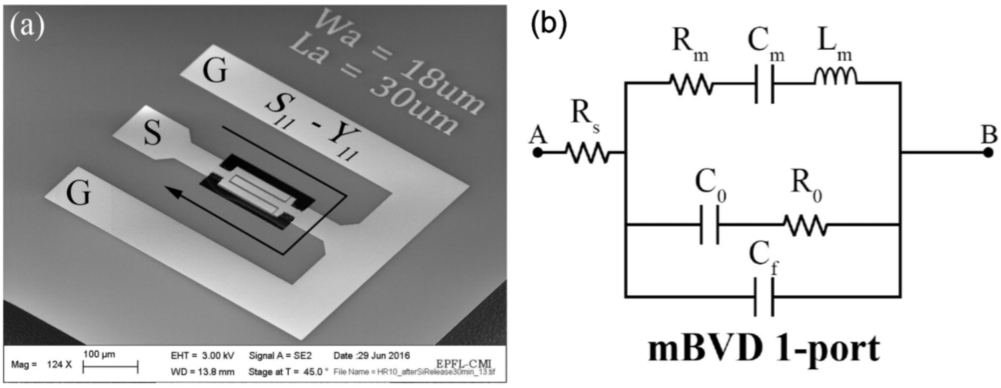


**Figure 1.6:** SEM image of a 1-port resonator in LTE configuration(a) and modified BVD model for 1 port devices(b) [8]

$C_m$ which represent the electrical equivalent of the motional parameters of the resonator, in parallel with a capacitance $C_f$, that consider the device and substrate feedthrough, while the signal is going forward and is reflected back. Moreover, the presence of the floating bottom metal is the main contributor for the addition of a static capacitance which can be seen as:

$$C_0 = \varepsilon_{33} \cdot \frac{Area\ Electrodes}{piezo\ thickness} \tag{1.3}$$

Where $\varepsilon_{33}$ is the dielectric permittivity of the piezoelectric material in the thickness direction[16]. To complete the mBVD model two more parasitic resistance $R_0$ and $R_s$ has to be added. The first one need to be considered in the same branch of the static capacitance $C_0$ and stands for the dielectric losses whereas the latter,in series respect to all the branches, represent the equivalent electrical resistance associated to the electrodes and contact pads. For this reason, it is strongly related to the choice of the metal used to provide the signal. Once that a given static capacitance $C_0$ has been determined, it is possible to obtain the value of the motional parameters for a rectangular geometry:

$$R_m = \frac{1}{\omega_s C_m}\frac{1}{Q} \tag{1.4}$$

$$L_m = \frac{1}{\omega_s^2 C_m} \tag{1.5}$$

$$C_m = n\frac{8}{\pi^2}\frac{PL}{T}E_{eq}d_{31}^2 = \frac{8}{\pi^2}C_0k_t^2 \tag{1.6}$$

Where $n$ is the number of fingers, T is the thickness of the piezoelectric material. P and L are respectively the pitch and length for the resonator. $E_{eq}$ is the equivalent young modulus and $d_{31}$ is the piezoelectric coefficient for the excitation of the S0 mode (lateral direction). The parameters Q and $k_t^2$ are the quality factor of the resonator and the coefficient evaluating the electromechanical coupling (both will be explained in the following section). The last appearing parameter is $\omega_s$ and simply correspond to the resonance frequency 1.2 multiplied for $2\pi$. Performing a measurement on this kind of devices, through a Network Analyzer (NA) exploiting RF probes, a result similar to the one in figure 1.7 is obtained:

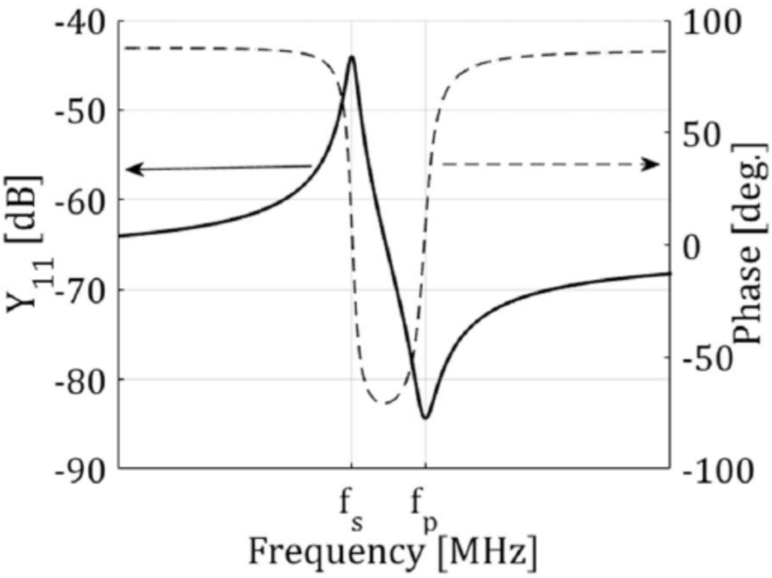


**Figure 1.7:** Typical $Y_{11}$ measurement of a 1-port LTE device [8].

Having a reflection measurement the relevant parameter is represented by $S_{11}$ (the subscript "11" means that the power sent to the first port is reflected to the same port). Usually this values is converted into a $Y_{11}$ measurement which can be plot in function of the frequency exhibiting: a resonance peak $f_s$ ( series resonance) determined by the motional branch, and an anti-resonance frequency $f_p$ (parallel resonance) associated to the presence of the parasitic branch with $C_0$ and $R_0$ (figure 1.7a)[8].

### 1.2.3 FBAR vs CMRs

As previously stated, due to the presence of a suspended structure, FBAR and CMRs exhibit similar heat dissipation and power handling capability making them to compete for similar applications. The main difference which characterize these two devices is the way in which the resonance frequency is determined and their capability to reach ultra high frequencies (UHF). In FBAR it is sufficient to reduce the piezoelectric thickness whereas in CMRs the same operation have to be done with the pitch. From a fabrication point of view, this fact constitute an advantage for FBAR since the deposition of a few hundreds nanometer layer constitute an easier task then reducing the CMRs pitch down to the nanometer scale. However, once that the fabrication process is well established, the CMRs own the great advantage of being able to reproduce many frequencies on the same chip by performing only layout modification. On the other hand, in case of FBAR, the multi frequency integration require an increased fabrication complexity related to mass loading and ion milling steps. The other significant difference between these devices is represented by the piezoelectic coupling efficient exploited for the excitation of the main mode. In fact, in FBAR the $d_{33}$ coefficient is utilized instead of the $d_{31}$ typical of CMRs. Since the first one present an higher amplitude, it will exhibit an higher piezoelectric coupling factor $K^2$ and, if correctly optimized, also an higher electromechanical coupling $k_t^2$ (those figure of merit will be explained in the next sections). A resume of the FBAR vs CMRs comparison is presented in table 1.1 :

| **Compared element** | **FBAR** | **CMR** | **Advantage** |
|---|---|---|---|
| Coupling coefficient | $d_{33}$ | $d_{31}$ | FBAR |
| High frequency fabrication | Thin piezoelectric layer | Small electrodes pitch | FBAR |
| Multi frequency integration | Ion milling & Mass loading | Layout modification | CMRs |

**Table 1.1:** Comparison between FBAR and CMRs.

As it is possible to see from the table, the CMRs, despite having the huge advantage of a simpler frequency integration, present more challenges in terms of fabrication and specifications. For those reasons the initial CMRs research target is to obtain similar performances and gain part of the FBAR market exploiting the advantage in multi frequency operations. To close the gap with FBAR, two different solutions are currently under study in the ANEMS LAb:

1. Introduction of DUV lithography tool to gain resolution for the pitch and become able to reach UHF.

2. Aluminum nitride doping with Scandium to enhance the electromechanical coupling.

Before explaining in details these two solutions (see "Research areas" section), to better comprehend the resonator behaviour it is useful to present the figures of merit (FoM) which characterize the piezoelectric resonators.

## 1.3 Figures of merit

In a piezoelectric resonator the key element is represented by the piezoelectric layer sandwiched between the metal electrodes. Here the electric field (E) and the strain are reciprocally converted to each other through the direct and inverse piezoelectric effect. Hence, the performance of the resonator itself is intrinsically related to the conversion of kinetic energy into potential one and vice versa. The efficiency of this conversion can be evaluated through two fundamental parameters: the Quality factor $Q$ and the electromechanical coupling $k_t^2$ [17]. Particularly important for a correct evaluation is the product $Q \cdot k_t^2$, since in some cases the increment of a parameter may decrease the other ones. Another crucial factor in the resonator evaluation is the presence of "spurious" modes, which are modes of oscillation different from the resonance that can deteriorate the other figures of merit and lead to error in the practical applications.

### 1.3.1 Quality factor

The Quality factor (Q) is a parameter used to evaluate the energy loss in a resonator. As previously mentioned, while a resonator is working the energy is continuously converted from potential to kinetic and vice versa in a cyclic way. During this process, part of the energy is irremediably lost in many form such as heat dissipation whereas, some other losses, can be associated to the excitation of unwanted oscillation modes or to the dissipation in the substrate outside the resonant structure. The simplest definition of quality factor is represented by the formula:

$$Q = 2\pi \frac{E\ stored\ at\ resonance\ peaks}{E\ dissipated\ per\ cycle} \tag{1.7}$$

However, this is a general definition that, from a practical point of view, is often not convenient. Hence, being piezoelectric resonators associated to an admittance response in the frequency domain (figure 1.7), is more convenient to use the following formulation which allow an easy evaluation from the graph:

$$Q = \frac{f_{res}}{BW_{3dB}} \tag{1.8}$$

Where $f_{res}$ (or $f_s$) is the resonance frequency of the device and $BW_{3dB}$ is the bandwidth of the peak where the attenuation respect to the top is 3dB. Observing the equation 1.8, high quality factor are associated to sharp peak in the frequency response since, while the other contributions have been fixed, it correspond to a narrower bandwidth. Having an high Q means that the energy has been more confined at the resonance frequency. In fact, all the mechanism that exhibit a coupling with the resonator without being part of the wanted response can be considered as losses[17]. For this reason, it is possible to distinguish many different contribute which cooperate to establish the total quality factor ($Q_{tot}$)[18]:

$$Q_{tot} = \left[ \sum \frac{1}{Q_i} \right]^{-1} \tag{1.9}$$

This means that a single source of losses can degrade significantly the performances of the resonator. Therefore it is crucial to individuate and optimize, as much as possible, each contribution. The main mechanism which contributes to energy losses are :

- *Electrical losses*, related to the finite conductivity of the employed materials.
- *Material losses*, associated to the intrinsic properties of the various layers.
- *Acoustic and anchor losses*, correlated to the energy not confined in the resonator.
- $Electro-mechnical\ losses$, which came from the conversion of energy between electrical and mechanical domains.

Hence, to optimize this FoM, is crucial to carefully work on design, material and fabrication processes. It is also important to notice that further losses elements are present but are not mentioned here since the quality factor is not a core research topic at this stage of the project.

### 1.3.2 Electromechanical coupling

The electromechanical coupling coefficient, usually called $k_t^2$ or $k_{eff}^2$ is a parameter which allow to evaluate the conversion efficiency between electrical and mechanical domains of the resonator. It is fundamental to highlight the difference between this parameter and the piezoelectric coupling factor. In fact, the $k_t^2$ depends also on the resonator design whereas the latter depends only on the material and is represented by the symbol $K^2$ and the following equation [8]:

$$K^2 = \frac{d^2}{c_E \cdot \epsilon_T} \tag{1.10}$$

Where d is the piezoelectric coefficient mainly exploited in the energy conversion and excitation of the mode, $c^E$ is the stiffness in condition of zero electric field applied and $\epsilon_T$ is the dielectric constant in zero stress condition. The piezoelectric coupling factor $K^2$ is crucial for the evaluation of a given piezoelectric material since it provide the upper limit for the electromechanical conversion [19]. Hence, every $k_t^2$ value measured will be lower than $K^2$. Concerning the electromechanical coupling $K_t^2$, due to its dependence from both design and materials, it is convenient to define it through resonance and anti-resonance position. Hence it can be expressed as [15]:

$$k_t^2 = \frac{\pi}{2}\frac{f_s}{f_p}tan(\frac{\pi}{2}\frac{f_p - f_s}{f_p}) = \frac{\pi^2}{8}\frac{C_m}{C_o} \tag{1.11}$$

If the difference in frequency between resonance ($f_s$) and anti-resonance ($f_p$) is small, the formula can be simplified obtaining:

$$k_t^2 = \frac{\pi^2}{4}\frac{f_s}{f_p}\frac{f_p - f_s}{f_p} \tag{1.12}$$

This formula will be considered as a reference for the rest of $k_t^2$ computations in this project. Moreover, being this formula strongly related to the peaks position in the $Y_{11}$ vs frequency graph, a rough evaluation can be performed by observing the image. In fact, higher $k_t^2$ correspond to higher peak to anti-peak distance in frequency.

### 1.3.3 Spurious modes

Another important factor which characterize the admittance response of mechanical resonator is the presence of spurious modes. These correspond to vibrational modes which differs from the resonance and are excited simultaneously to it. As a result, the admittance plot is not completely smooth as in the illustrative plot of figure 1.7, but it usually present some ripples. For practical application, the amplitude of these spurious mode has to be really small. In fact, in case of filters, the spurious modes presence could enlarge or modify the pass band degrading the filter performances, whereas, in application like oscillators, ripples close to the resonance can induce an amplification at the wrong frequency, leading to an unwanted behaviour. According to [20], their origin is mainly related to bus interaction, asymmetries and interaction with the anchors. For these reasons during the design phase it is not sufficient to maximize the response at the resonance frequency, but, it is necessary to analyze the shape of each spurious mode in order to comprehend their behaviour and minimize their coupling.

## 1.4 Research areas

As already mentioned in section 1.2.3, the Contour mode resonator present great potentialities but it still need improvements to become competitive with the other solution. In this section the two main research areas characterized by this objective are presented.

### 1.4.1 Aluminum scandium nitride

As previously introduced in the "Figures of Merit" section, the electromechanical coupling ($k_t^2$) depends both on design and material properties. Hence, to enhance the electromechanical coupling without considering the design, it is necessary to find materials with higher piezoelectric coefficients. Thanks to its IC compatibility, one of the most employed materials for the realization of piezoelectric resonator is the aluminum nitride (AlN)[21]. However, due to its limited piezoelectric coefficient, many different doping material have been tested to enhance ita piezoelectric response. Among these, the Scandium (Sc) is the most promising one since it allow to increase the asymmetry of the Wurtzite cell enhancing up to 4x the piezoelectric response [22]. Therefore, to maximize the piezoelectric coefficients, many different Scandium percentage $x$ have been analyzed in literature up to 50%, developing so a new alloy called aluminum scandium nitride ($Al_{1-x}Sc_xN$). From those tests, which where performed by cosputtering the alloy from aluminum and scandium targets, the piezoelectric response resulted to be strongly related to deposition temperature and scandium concentration[23]. In particular, considering a deposition temperature of $400°C$, as showed in figure 1.8, the piezoelectric response versus percentage of scandium exhibit a clear peak few units above 40% and then rapidly decreases. This means that the asymmetry of the cell is gradually increased and then broken around 45% of Scandium concentration. For this reason, following the aim to maximize the electromechanical coupling, the deposition process have been previously optimized (by Marco Liffredo and Xu Nan) for a scandium percentage of 40% (in order to keep a certain margin respect to the rapid decrease). Hence, this

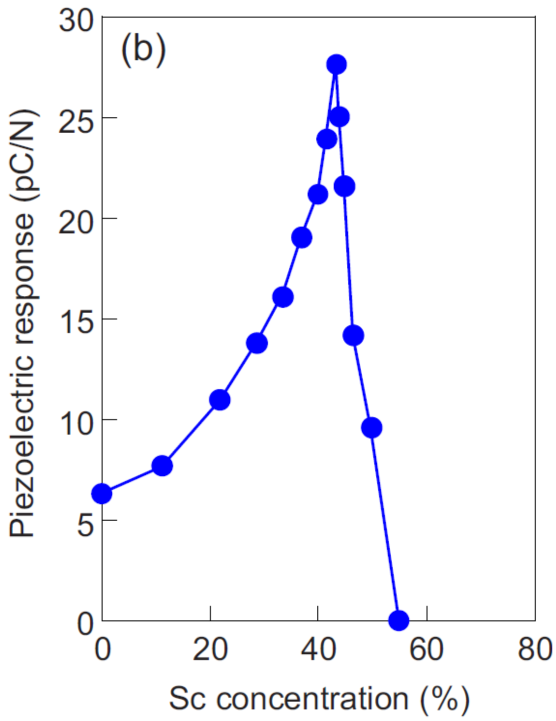


**Figure 1.8:** Piezoelectric response behaviour of AlScN depending on Scandium percentage [23]

concentration has been selected as a reference an will be implicitly considered for the rest of the project. In this way, by exploiting the maximum enhancement of the $k_t^2$ obtainable through the material modification, more competitive performances can be obtained.

### 1.4.2 DUV lithography

As previously mentioned one of the issues associated to CMRs is represented by the necessity of high resolution tools to reach high frequency by reducing the electrodes pitch. The most employed tool in research for this kind of requirements, due to its extremely high resolution which can reach few nanometers, is represented by the e-beam lithography [24]. However, this tool perform a serial scan of every image, therefore, since in this project the device target the industrial applications, this slow throughput lithography is not suitable because it would have lead to a huge increase of process time and so to a not sustainable cost increase. Hence, the choice is fallen on the stepper for DUV lithography and, in particular, on the ASML PAS 5500/350C available in the EPFL center of microtechology (CMi). Its structure is represented in figure 1.9:

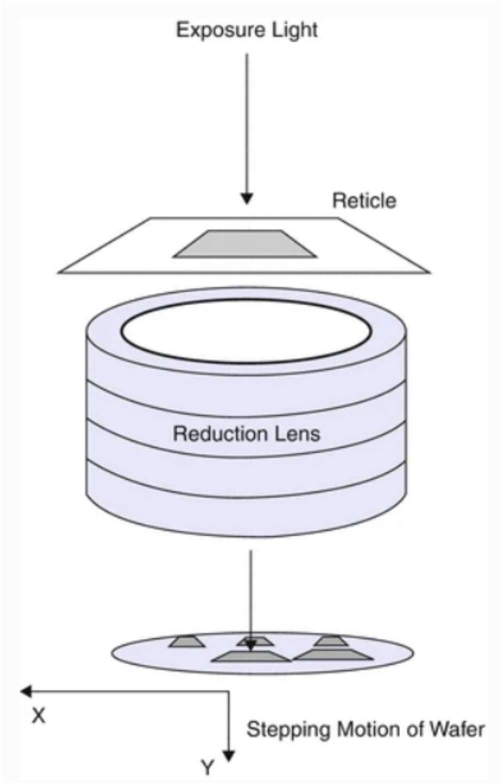


**Figure 1.9:** Typical structure of a DUV stepper [25]

The DUV light, coming from a KrF laser source with 248 nm of wavelength, arrive from the top of the structure, here, through the employment of a quartz reticle, the wanted pattern is realized and then, exploiting many demagnifying lenses, the image is reduced by a factor of 4 before reaching the wafer where the image is impressed thanks to the photoresist. The name stepper comes from the fact that this tool allow to partially cover the reticle exposing only a portion of the image. Then the wafer can perform a "step" in order to expose another part of the wafer with the previous or with a different image. This feature is particularly interesting since it allow many degrees of freedom in the job definition and in the parameters optimization for each design. Concerning the specifications, the resolution (R) of the ASML PAS 5500/350C, which correspond to half of the minimum pitch size, can reach 150nm. Hence, the minimum feature size is lower than the KrF laser wavelength. This extremely positive result, as it is possible to see from the Rayleigh criterion (1.13), is allowed thanks to the presence of demagnifying lenses and optimal process conditions.

$$R = C_1 \frac{\lambda}{NA} \tag{1.13}$$

Where $\lambda$ is the laser wavelength, NA is the numerical aperture of the lens and $C_1$ is a factor related to the process. Another fundamental parameter that has to be taken into account for the stepper is the depth of focus (DOF) which can be expressed through the equation [26]:

$$DOF = C_2 \frac{\lambda}{NA^2} \tag{1.14}$$

Where $C_2$ represent another process parameters. As it is possible to see observing the equation 1.14 the DOF is proportional to the same parameters of the resolution (except for the process condition coefficient) and so, an increment in resolution lead to a decreased DOF. Hence, the DOF stepper value corresponds roughly to $1\mu m$ and so it determines additional flatness requirement for the employed wafer. In fact, a minimum of $2\mu m$ total thickness variation (TTV) is required for simpler application and a $0.5\mu m$ TTV is strongly suggested in presence of critical steps. Despite this added complication the stepper presents many other advantages like the possibility to exploit three different alignment possibility:

1. $The\ topside\ on-axis\ alignment\ system$, which is performed by illuminating some specifics marks through a red laser and align the wafer with a maximum error of 25nm.

2. $The\ backside\ on-axis\ alignment\ system$, which, exploiting the same equipment of the previous one plus the addition of periscopes, guarantee worse alignment performances (maximum error of 60nm) with the advantage of align multiple layers to the same backside marks avoiding fabrication issues.

3. $The\ topside\ off-axis\ alignment\ system$, also called ATHENA, which, employing both a red and a green laser and being able to detect many diffraction order, increase the alignment capability in presence of layers which cover the marks maintaining the same resolution of the other topside marks (25 nm).

The presence of these three systems played a crucial role in the choice of this tool, since they allow to guarantee at the same time high performances (due to the small maximum misalignment) and great flexibility making the DUV stepper a tool suitable also in case of complex processes.

To sum up the DUV stepper seems to be a great option for the development of high frequency resonator, since, despite the more demanding requirement and the system complexity respect to the standard UV lithography, thanks to its high resolution, low misalignment and high flexibility allow to build CMRs with resonance frequency in the ultra high frequency range (300MHz-3GHz) and beyond.

# Chapter 2

# 2D Simulations

To understand the impact of each parameter on the behaviour of the device and to explore the impact of various solutions, some preliminary simuations have been performed. Hence, starting by the work previously done by on the COMSOL software by Marco Liffredo and Giacomo Graziano, who already build the standard model and the $Al_{0.6}Sc_{0.4}N$ library, many evaluations have been considered[15]. The aim of this section is to exploit the low computational cost offered by 2D simulations in order to reduce the spurious mode of the resonator and to understand the best configuration to be able to scale up in frequency.

## 2.1 Reference model

The reference model consist in the 2D representation of one typology of the LTE CMR devices already built by Marco Liffredo, which was already used to verify the coherency between real behaviour and simulations. The 2D geometry is quite simple and is shown in figure 2.1. Starting from the bottom it is possible to observe a floating platinum electrode with 50nm of thickness on which lies a 500nm thick AlScN piezoelectric layer. At the top of the structure three 50nm thick metal fingers in Pt, are present alternating signal and ground. The width of the resonator has been set to $60\mu m$, the pitch has been set to $20\mu m$ whereas the standard electrode width has been set to $15\mu m$. The various modification of this design and materials will be explained when introduced.

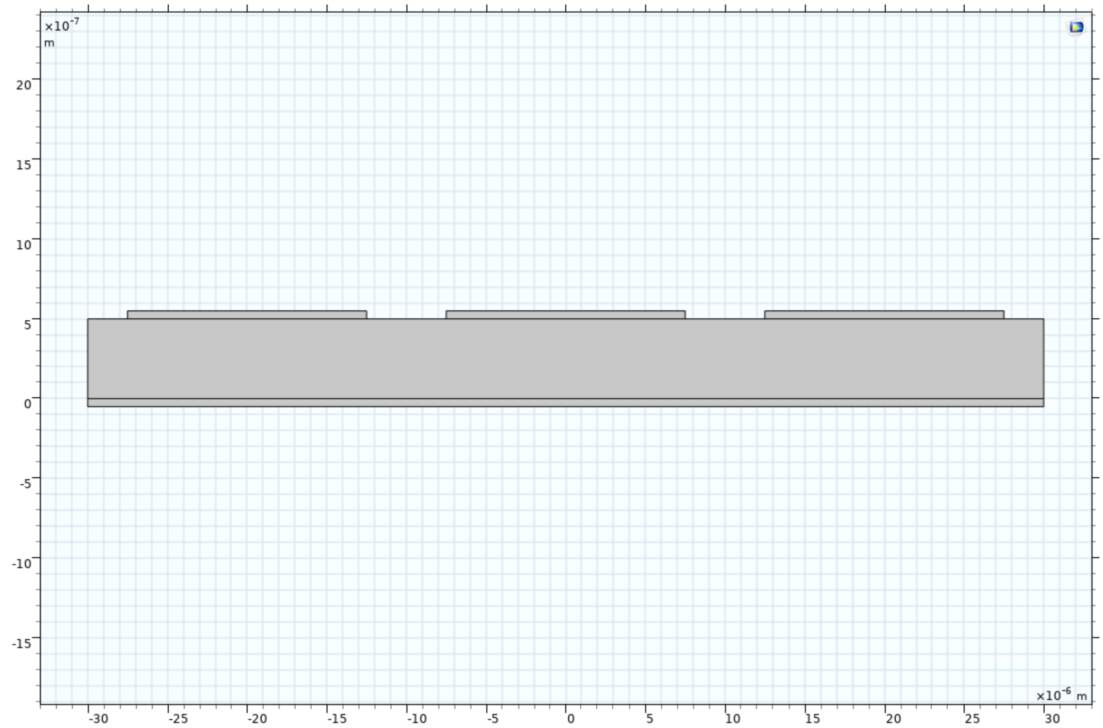

**Figure 2.1:** Geometry of the reference model for 2D simulations

From the simulation point of view is also important to notice that the bottom and top electrodes are included in the mechanical domain since, due to their different young modulus E and density ($\rho$) with respect to the AlScN, they modify the phase velocity in the material modifying consequently the resonance frequency of the device. On the contrary they are not present in the electrical domain since the electric field is mostly distributed in the piezoelectric material. This simulation choice lead to the fact that the electrical resistance (Rs) will be neglected in the simulations. This fact must be carefully considered when the devices will be fabricated and measured since, if the resistance will be too high, it will constitute the limiting element for the quality factor. In this considerations about the electrical resistance, it will be crucial to consider the ratio between width and length of the metallic fingers. Moreover, the length of the resonator and, in particular, of the active region $L_{active}$, is extremely important also in the 2D analysis since it allow to determine the area where the piezoelectic layer is excited by the electric field, representing so a key factor for the determination of the motional resistance $R_m$. In this reference model $L_{active}$ has been set to $122.5\mu m$. The results obtained from this parameter choice constitute the reference Admittance $Y_{11}$ plot (in siemens [S]) for this model and is visible in figure 2.2:

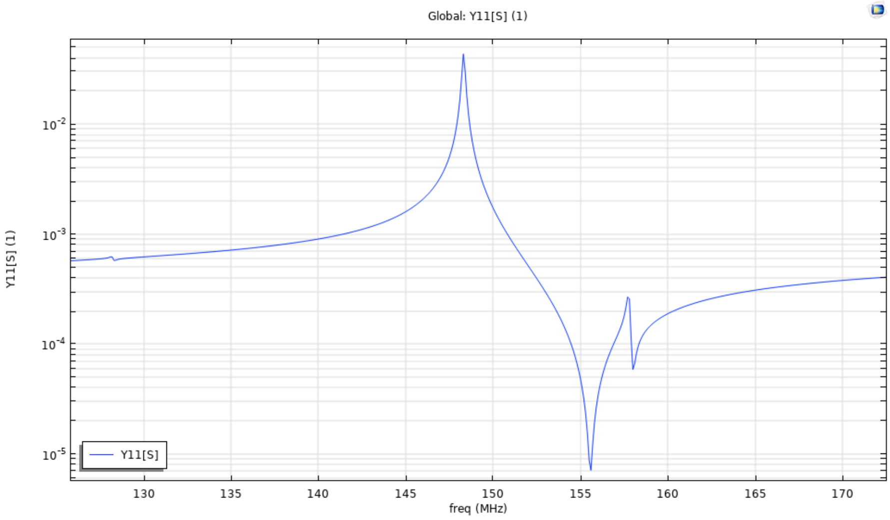


**Figure 2.2:** Admittance $Y_{11}$ vs frequency plot of the reference model.

Here it is possible to see the resonance frequency $f_{res} = 148.3MHz$ a small spurious mode around 128MHz and a more relevant spurious at 157.7MHz just after the anti-resonance. To give a reference about the shape of the modes we are discussing about, the x displacement has been showed in figure 2.3

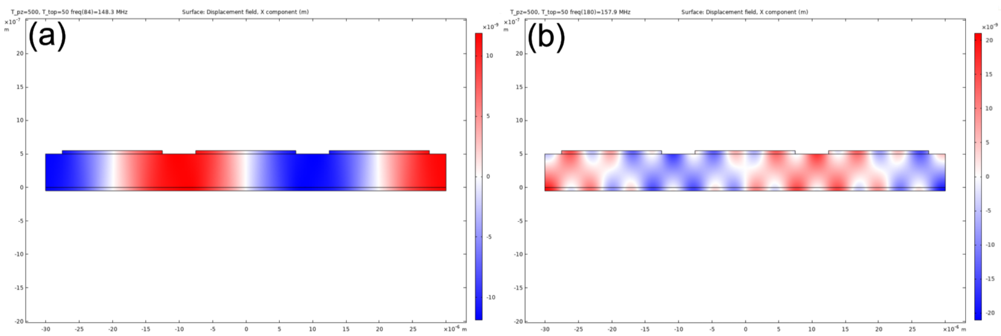


**Figure 2.3:** Mode shape (displacement in x component) for S0 mode (a) and spurious modes (b). Here only the one at 157.7MHz is reported since the other (128MHz) exhibit the same shape with a lower amplitude of displacement.

## 2.2 Resonator width analysis

The first analysis performed has been done to understand the impact of the mechanical constraint imposed by the resonator width in the determination of: resonance frequency, electromechanical coupling and admittance of the device. Hence, the width of the resonator have been gradually increased from the reference value of $60\mu m$ up to $105\mu m$ while maintaining fixed the electrical boundaries. This means that the top platinum fingers remained constant in number, pitch and position. The resulting plot has been depicted in figure 2.4:

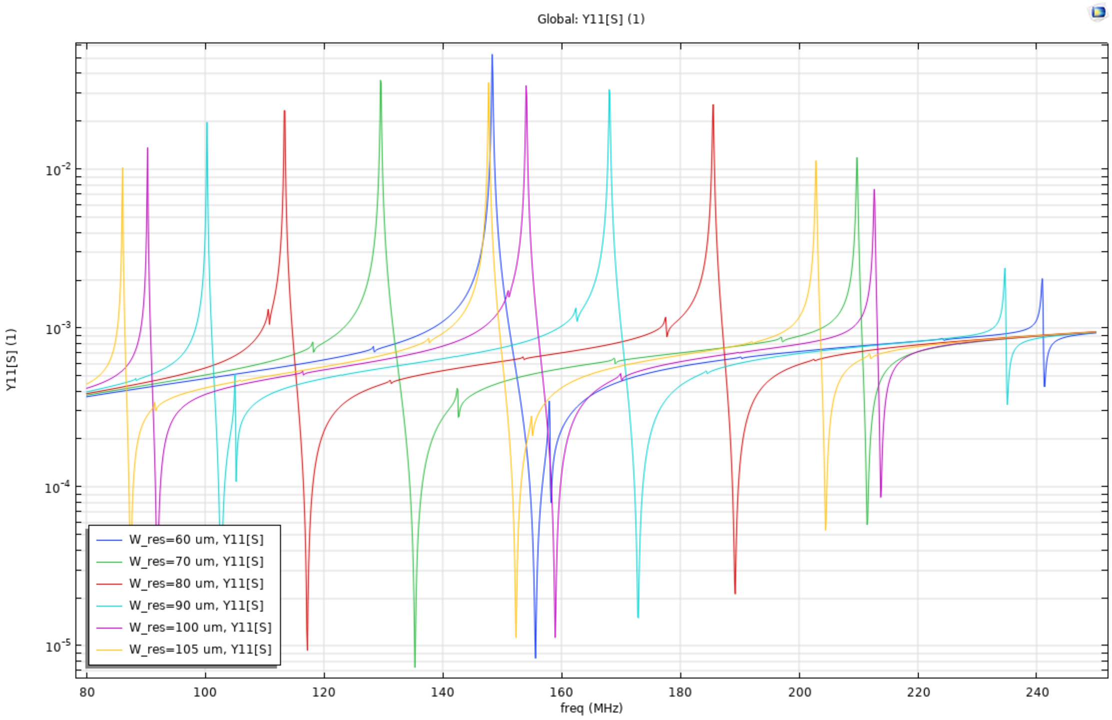


**Figure 2.4:** Admittance $Y_{11}$[S] varying the Width of the resonator with fixed electrical boundaries

Observing the image it appears as clear that the resonance seems to be sharper around the reference plot at 148MHz, however, since for some widths many resonances appears, it is necessary to analyze the mode shape to completely understand the behaviour and see exactly which modes are excited. From this analysis it results that for each width two or three different lateral modes (neglecting the small spurious) are present. Choosing a given width, selecting the displacement in x direction(horizontal) as a way to determine the mode shape and progressively increasing the frequency it is possible to see that the peak of lateral mode with 3, 5 and 7(if is in the range) nodes are encountered for each plot. Hence, the peak corresponding to the 3 nodes modes (figure 2.6 a) have been analyzed.

### 2.2.1 Modes analysis

To clearly verify the the admittance and electromechanical coupling behaviour respect to the width, the data have been plotted and exported on MATLAB (figure 2.5). The result obtained is coherent with the one expected since both Admittance (figure 2.5 a) and coupling (2.5 b) decrease increasing the width.

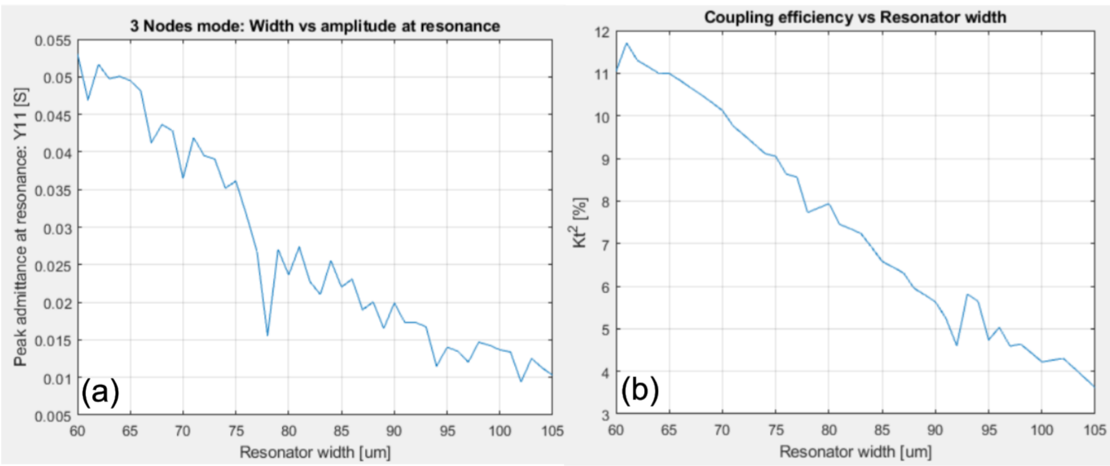


**Figure 2.5:** Peak $Y_{11}$ admittance at the resonance frequency compared to the resonator width (a) and electormechanical coupling $k_t^2$ behaviour with respect to the resonator width (b).

To explain this behaviour it is necessary to analyze the mode shape by looking at the x component of the displacement for the reference model (figure 2.6 b), and to compare it with the same mode at bigger width (figure 2.6 c and d). It appears clear that, for the reference model, the three nodes (points with zero displacement) of the modes are perfectly centered under the platinum fingers, whereas increasing the width the two lateral nodes are gradually moving outside the area below the fingers.

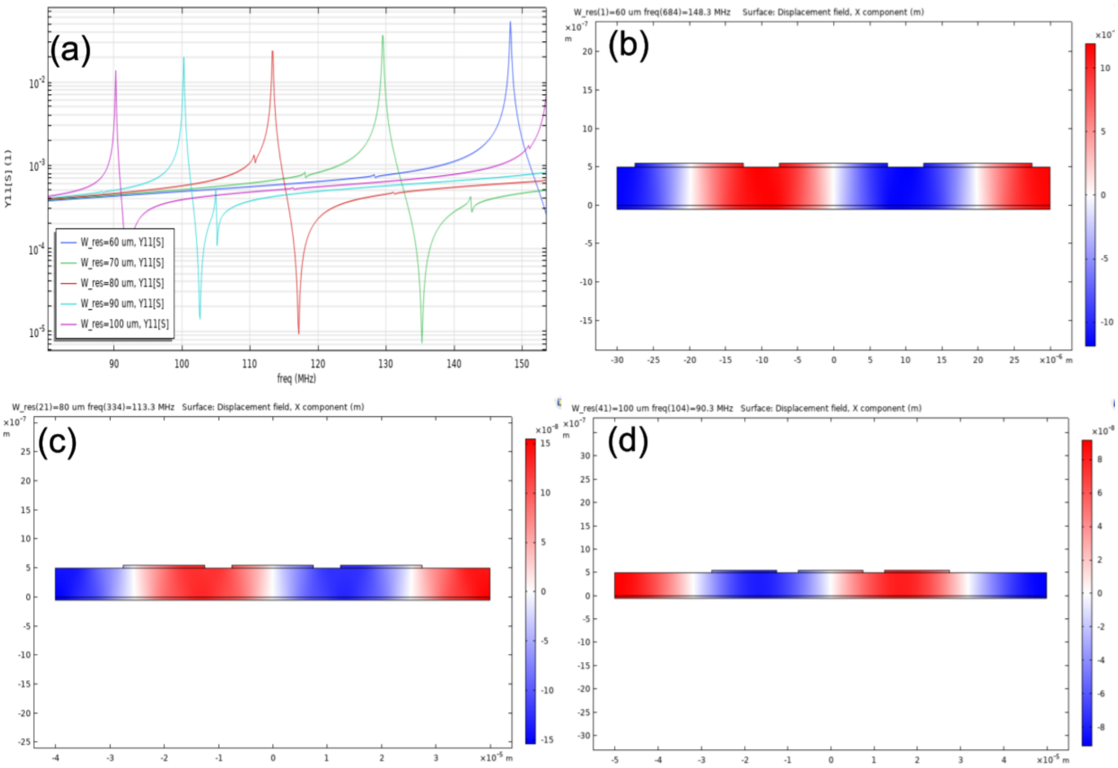


**Figure 2.6:** Admittance Y11[S] of 3 nodes modes at different widths (a), x component of the displacement in the reference model (b), x component of the displacement considering respectively $W_{res}$ of $80\mu m$ and $100\mu m$.

From this information it is possible to formulate some hypothesis able to explain the result of the simulation:

- The distance between two adjacent nodes is progressively augmented with the width since it works as a mechanical boundary. Hence, even if the pitch is the same, the wavelength increases because of the position of the nodes inducing a reduction in frequency.
- Concerning the admittance, it seems to be maximized in the reference configuration (figure 2.6 a). The explanation could be related to the density of the platinum which is much higher than the one of AlScN. This means that in the reference configuration, having the node exactly in the middle of the electrode, the movement of the highly dense metal is minimized reducing so, as much as possible, the mechanical losses. On the contrary, the opposite effect will be obtained moving the nodes, having so a progressive increase of this detrimental effect which is going to decrease the quality factor.
- Concerning the $k_t^2$ its behaviour can be explained considering the electrical

and mechanical boundaries. Increasing the width the distance between the nodes increases, leading to a reduction of the resonance frequency, whereas, at the same time, the electrical boundary constituted by the metal electrodes and their position is maintained fixed and try to excite the piezoelectric material at an higher frequency. Therefore a mismatch between electrical and mechanical wavelength is gradually generated inducing a gradual reduction of the electromechanical coupling.

A similar analysis have been repeated also for the 5 mode peaks. Here the behaviour of the resonance frequency is the same (it decreases increasing the resonator width) and it is perfectly coherent with the explanation previously given. Concerning the the Admittance and the electromechanical coupling, the behaviour is opposite respect to the width of the resonator, since both $Y_{11}$ and $k_t^2$ increase decreasing the width. Therefore, the reference model exhibit the worst performances among the ones under examinations. To analyze the phenomena, it is necessary to plot again the mode shape and see the differences (only few examples to show the trend have been reported here).

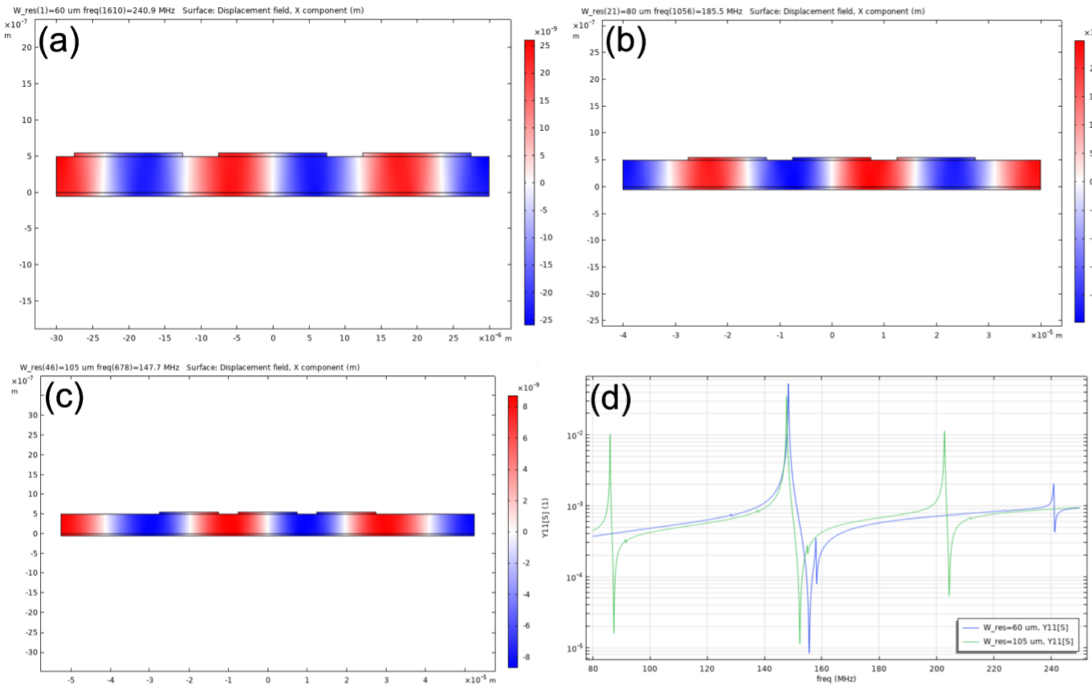


**Figure 2.7:** Displacement in x direction for reference model (a), $W_{res} = 80\mu m$ (b) and $W_{res} = 105\mu m$. In image (d) is represented the admittance of the 3 nodes mode for the reference model($W_{res} = 60\mu m$) versus the 5 nodes mode with $W_{res} = 105\mu m$.

Observing the figures 2.7 a, b and c it is possible to see that, having five nodes instead of three, the zero displacement are situated below the center of the electrodes only for bigger width (otherwise this condition could have been met modifying the pitch that we have assumed as fixed). Hence these result are perfectly coherent with the explanation previously given. In fact the admittance is maximized for $W_{res} = 105\mu m$ where the nodes are placed exactly in the middle of the platinum electrodes minimizing their displacement and so the mechanical losses. Moreover, as previously happened, the electromechanical coupling is maximized when the wavelength imposed by the mechanical boundaries is closer to the one imposed by the electrical boundaries. Having coherent result, it is interesting to make a comparison between the best case for the 3 nodes mode ($W_{res} = 60\mu m$) and the best case from the 5 nodes mode ($W_{res} = 105\mu m$) like the one observable in figure 2.7 (d). Analyzing the image, it is possible to see that the plot of the three nodes mode present better $Y_{11}$ (higher peak) and $K_t^2$ (bigger distance from peak to anti-peak at the same frequency). These lower performances for the 5 nodes mode are probably related to the lack of two electrodes that lead to a less efficient excitation of the piezoelectric material. Therefore we can still consider the condition with the nodes of displacement below the middle of the electrodes as the one related to an optimal excitation. What it is also interesting to see is that, in this configuration, the ratio between $W_{res}$ and number of nodes is roughly the same and coincide with the pitch (P) of the resonator. A slight difference is present between the two ratios, but it could be associated to the lack of the electrodes in the 5 nodes mode simulated. Hence, we can extrapolate a general relation which links the mechanical ($W_{res}$) and electrical (pitch) boundaries for an optimal excitation of the S0 mode:

$$P = \frac{W_{res}}{m} \tag{2.1}$$

Where m is the number of displacement nodes. This means that once a boundary is fixed the other one need to be selected in agreement with the first one, but, at the same time, it is possible to properly select the resonance frequency choosing the number of node excited in the S0 mode. Finally, to give consistency to the previous hypothesis the analysis have been repeated for the 7 nodes mode. Also in this case the behaviour in terms of resonance frequency is the same and the performances in terms of $Y_{11}$ and $K_t^2$ tends to improve when the position of the nodes gets closer to the center of the electrodes (in this case the admittance is optimized for $W_{res}$ around $140\mu m$. To verify also the correctness of the formula 2.1 an example of overlap between the 5 and 7 nodes modes have been considered in the following figure:

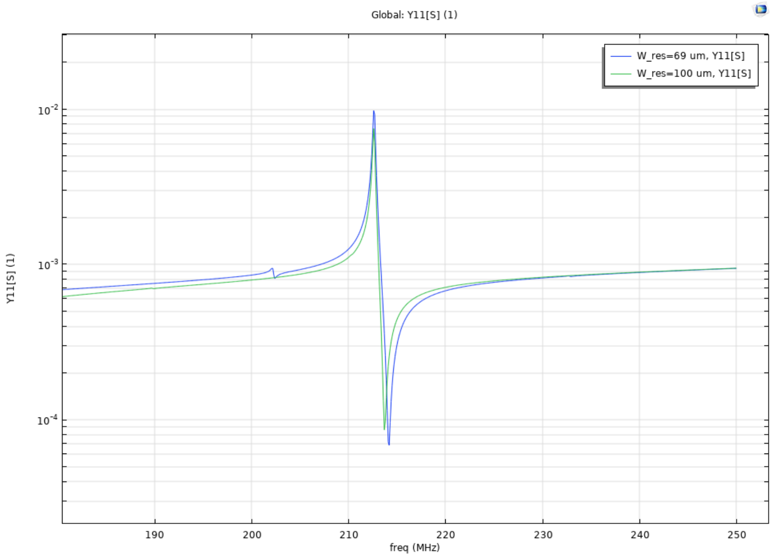


**Figure 2.8:** Admittance $Y_{11}$ [S] of 5 nodes mode at $W_{res} = 69\mu m$ and of 7-node mode at $W_{res} = 100\mu m$

Applying the equation 2.1 it is possible to obtain $P_{5-nodes} = 13.8um$ and $P_{7-nodes} = 14.28um$. Also in this case the difference of result could be related to the difference in density related to the fixed number of electrodes. Moreover the pitch imposed by the mechanical constraints is different respect to the one of the electrodes. This can be verified by observing the two mode shape of the two plots:

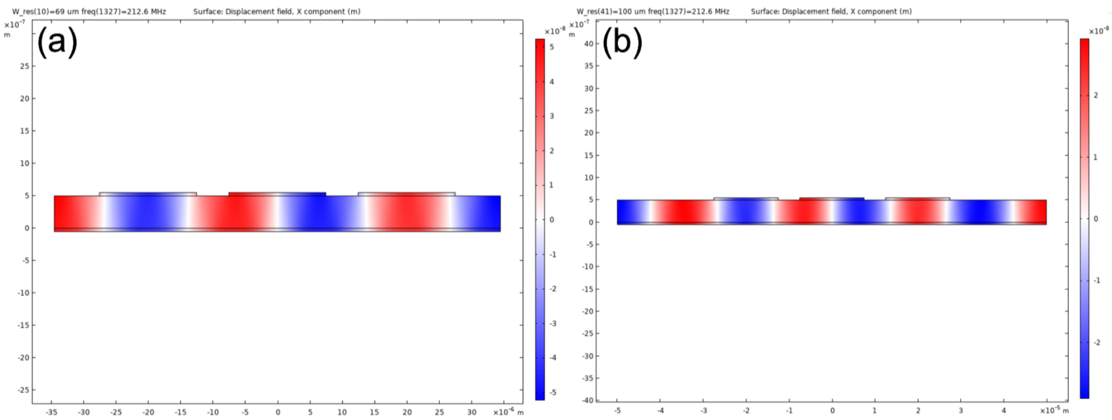


**Figure 2.9:** Mode shape (displacement in x component) of the 5-nodes mode $W_{res} = 69\mu m$ (a) and of 7-node mode at $W_{res} = 100\mu m$ (b)

As predicted by the equation the position of the nodes respect to the electrodes is the same, confirming the validity of the hypothesis, whereas the position of

the nodes highlights the mismatch between electrical and mechanical boundaries, explaining so, coherently with the expectation, the lower $Y_{11}$ and $K_t^2$ respect to the reference model.
Being all the results coming from the simulations coherent, we can assert that:

- For the optimal excitation of the lateral S0 mode the nodes of the displacement must be set in correspondence of the middle of the electrodes.
- The electrical boundary provided by the pitch is important to define the resonance frequency as stated in the equation 1.2 but it has to be properly matched with the wavelength imposed by the resonator width as a mechanical boundary.
- The simple formula 2.1 deduced in this analysis can determine a good approach for the resonator design.

## 2.3 Spurious analysis in 2D

One of the main challenges in the resonator design and fabrication is the elimination of the spurious modes from the admittance response since their presence is a limiting factor in the practical application of these devices. Hence the goal of this analysis is to understand the source of the spurious mode and try to find solutions to eliminate or reduce their impact. It is important to notice that the following analysis, having only a two dimensional model, can detect only part of the spurious because, some other, transverse to the considered section, are not simulated. Moreover, the geometry is considered as perfect but this assumption is not true when the devices is fabricated since, even with the most optimized process, the resonators will be characterized by some imperfections.

### 2.3.1 Spurious mode versus electrode size

Following the result of the previous section related to the matching between electrical and mechanical boundaries we considered the hypothesis that, centering the nodes of the displacement in the middle of the electrodes and reducing the fingers width could have led to the reduction of the spurious excitation. Here it is important to introduce the concept of electric coverage:

$$EC(\%) = 100\frac{W_{el}}{P} \tag{2.2}$$

Where $W_{el}$ is the electrodes width (in this simulation it will be also called W) and P the pitch. Hence, given this definition, in this simulation the electric coverage of the resonator have been altered by modifying the width of the electrodes keeping constant the pitch in order to analyze any possible impact on the spurious. To do that, as a first approach $W_{el}$ have been swept between $17\mu m$ and $1\mu m$ separating the result in to images to make it more readable as it is possible to see in figure 2.10.

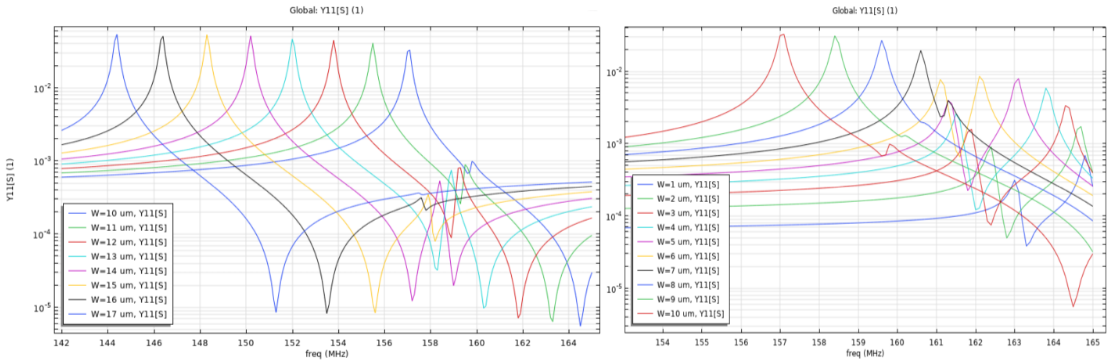


**Figure 2.10:** Admittance response [S] varying the width of the electrodes at a constant pitch. EC range between 0.95 and 0.5 on the left, EC range between 0.5 and 0.05 on the right.

Observing the result the initial hypothesis is refuted. In fact, the best result in terms of spurious modes are obtained for higher electric coverage. Moreover, decreasing $W_{el}$, the resonance peak is progressively blue shifted whereas the spurious mode remains at a similar frequency. Hence, below $EC = 40\%$ ($W_{el} = 8\mu m$) the admittance response is compromised since the main mode become hybridized with the spurious mode generating two peaks with a similar entity and hybrid shape. Therefore from this analysis it is possible to deduce that the optimal EC range is between 40% and $80\% - 85\%$ (the upper bound is given by short circuit risk).

### 2.3.2 Electrode spacers

From previous simulation it was obtained that, removing the metal electrodes from the mechanics, the admittance response was characterized only by the presence of the main mode and the spurious where completely eliminated. This information linked to the result of the previous simulation, which showed lower spurious modes with higher electric coverage, could suggest that these modes visible in the 2D plot are actually generated, considering a LTE CMR, by the mismatch between the amount of metal on the top and on the both of the resonator. Hence, the presence of spurious modes could be related to the difference in stiffness associated to the presence of a full layer of platinum on the bottom and a patterned top electrode. To prove this hypothesis and try to eliminate the detrimental modes, a dielectric material have been inserted between the fingers with the function to separate them and, at the same time, reduce the mismatch in terms of stiffness between top and bottom metal like in the following picture:

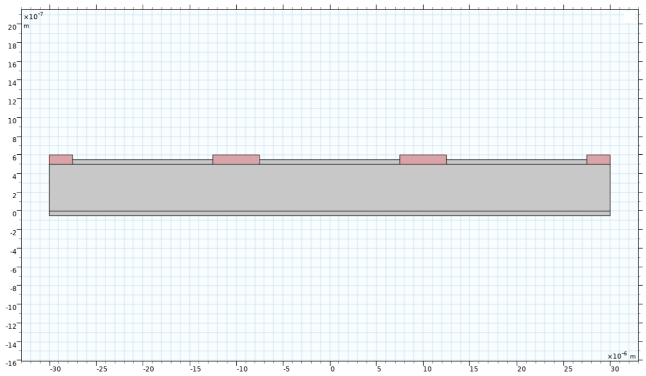

**Figure 2.11:** 2D geometry of the resonator with the addition of the spacers

As a choice for the dielectric material, that from now on will be called as "spacer" or "electrodes spacer", many possibilities have been evaluated but the chosen one is the Aluminum Nitride (AlN). This selection is related to the fact the AlN is dielectric, has a well known deposition process, and is the material with the closer properties respect to the AlScN layer minimizing so the discontinuities in the system. However, this material has different mechanical properties respect to the platinum, therefore a the new geometry has been simulated while performing a sweep of the spacer thickness visible in figure 2.12.

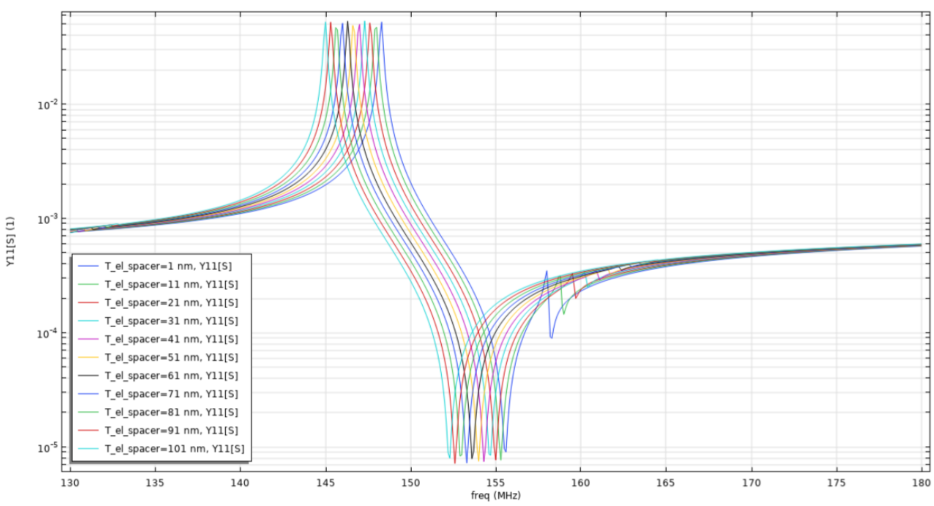


**Figure 2.12:** Admittance response versus frequency performing a sweep of the spacer thickness

Observing the result, as expected, the resonance frequency slightly decrease increasing the thickness of the spacers due to the increase of the mass loading on the resonator. Considering the spurious modes, their amplitude seems to gradually decrease. To analyze in a better way the spacers effect is interesting to perform a zoom around the admittance of these modes.

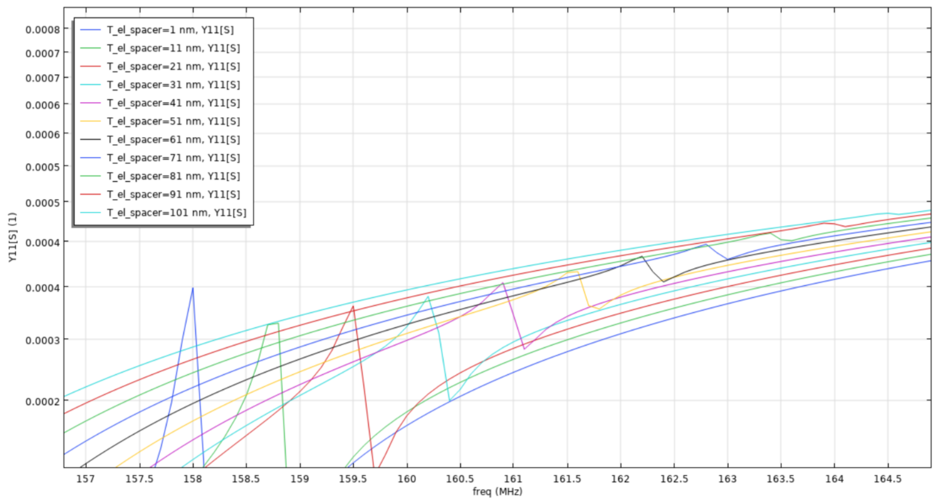


**Figure 2.13:** Admittance $Y_{11}$ plot, showing the behaviour of the higher frequency spurious mode(respect to the resonance) increasing the spacer thickness

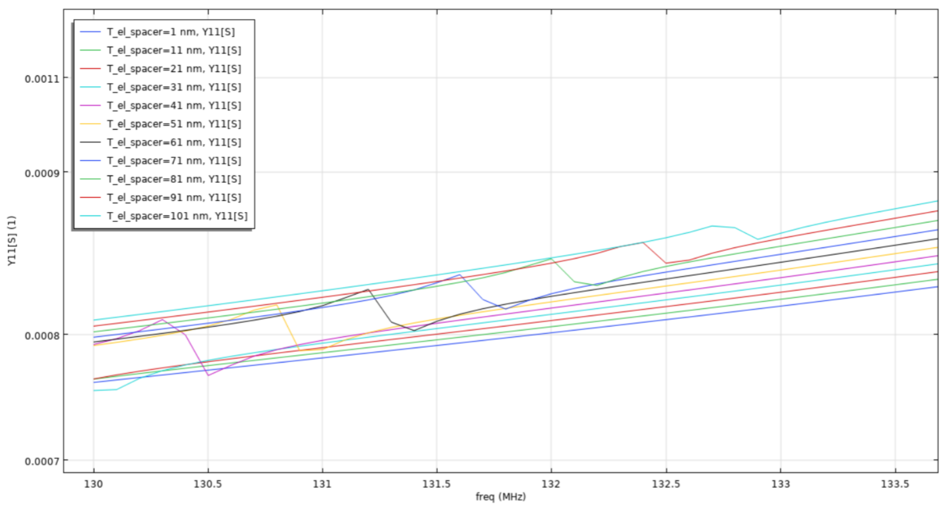


**Figure 2.14:** Admittance $Y_{11}$, showing the behaviour of the lower frequency spurious mode(respect to the resonance) increasing the spacer thickness

Both graphs show a good result. In fact, in both cases the amplitude of the spurious modes tends to decrease and is almost zero once the thickness of the spacer reaches $100nm$. For this reason, at least for a 2D analysis, the presence of the spacers seems to have a positive impact on the resonator admittance unless the specifications require a frequency higher than the one reachable with this configuration. However some consideration regarding the solution provided by the spacer has to be done before inserting them into a design:

- The thickness of the spacer need to be finely tuned in order to find the optimal one (in this case coincides with $100nm$). In fact, increasing it over this level is going to decrease the symmetry of the device in the opposite way respect to the initial situation, reducing so the benefit provided by the spurious and inducing a further worsening of the mass loading.

- The effect of this solution is strongly related to the choice of materials. In our case it has such a big impact due to the choice of platinum, which exhibit completely different mechanical property respect to AlScN, but it might significantly decrease in case different material choices.

- The presence of the spacers induce a red shift in terms of resonance frequency and a blue shift considering the spurious modes frequency. Therefore, since even if they reduces the amplitude of the spurious they do not completely eliminate it, therefore, depending on the position of the spurious, their presence might be detrimental. In fact, even if a spurious is small, when it comes close to the resonance frequency its amplitude is strongly enhanced degrading the performance of the resonator.

- The impact of this feature still has to be considered for a 3D application, as well as their eventual fabrication.

For this reasons, despite this seems to be a promising solution, the impact of the spacers still need to be evaluated and, as a first approach, we will try to make the resonators without them eventually adding them in a second moment.

### 2.3.3 Spurious modes and size of the resonator

From the results on the previous analysis and in particular observing figures 2.7(d) and 2.8 it is possible to observe that the amplitude of the spurious modes in terms of admittance seems to decrease enlarging the resonator. This effect might be related to the fact that, increasing the resonator width, the periodicity of the structure is augmented and the impact related to the discontinuity at the end of the resonator is reduced. However, in the case of the mentioned figures, the number of fingers where limited and fixed to three limiting the electrical excitation of the piezoelectric layer. For this reason it is interesting to increase $W_{res}$ increasing at the same time the number of fingers and maintaining the condition of optimal excitation suggested by equation 2.1(for each added finger the resonator width increases by $20\mu m$). Hence, a simulation have been performed by sweeping the number of fingers from 3 to 19 with the step of 2.

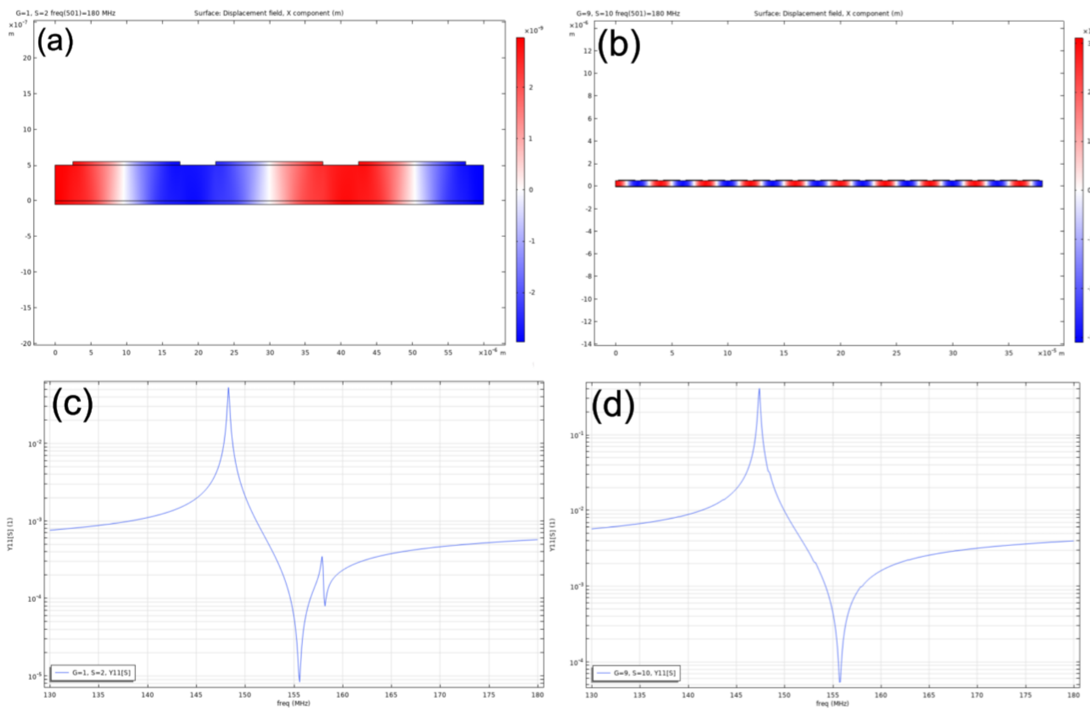


**Figure 2.15:** Mode shape along x axis for reference model(a) with 3 fingers and for larger resonator with 19 fingers(b) (S and G represent respectively the number of signal and ground fingers). Admittance plot versus frequency of the 3 fingers (c) and 19 fingers resonator(d).

As a result the simulation shows a gradual reduction in terms of spurious modes amplitude increasing the width of the resonator and the number of fingers. Here in figure 2.15 the reference model (a) with its admittance (c) have been compared to the biggest simulated resonator (b) and is admittance (d) to highlight, as much as possible, the difference between the two resonators. The model with 19 fingers, even if showing more spurious modes than the reference model it exhibit a strongly reduction in their amplitude which constitute a significant improvement. The source of the spurious modes could still be related to the presence of asymmetries between top and bottom metal, whereas the reduced amplitude could be related to the repetition of the same pattern which lead to a much less significant impact of the discontinuity generated by the mechanical boundaries. The drawback of the model with 19 fingers is the size since it goes in the opposite direction respect to the aim of reducing the dimension, however this result might be promising since,a similar result in terms of spurious modes, might be obtained by keeping the same width and reducing the excited wavelength.

### 2.3.4 Spurious modes vs pitch

Following the result of the previous simulation, it is possible to hypothesize that, the amplitude in terms of admittance of the spurious modes in 2D simulations is associated to the resonator width $W_{res}$ and the pitch P. The idea is that, bigger is the width respect to the pitch, lower is the impact of the mechanical boundaries at the end of the resonator decreasing so the amplitude of the spurious modes. Hence, in order to verify this hypothesis, the width of the resonator have been set at $W_{res} = 60\mu m$ and the number of fingers have been increased from 3 up to 29 keeping the electrical and mechanical boundaries matched. This has led to a gradual reduction of the pitch starting from $P = 20\mu m$ down to $P \approx 2.1\mu m$ (P=$W_{res}/N_{fingers}$). It is important to notice that, reducing the pitch and maintaining the optimal excitation conditions, the resonance frequency is going to increase according to the formula 1.2:

$$f_{res} = \sqrt{\frac{E_{eq}}{\rho_{eq}}} \cdot \frac{1}{2P}$$

This effect is positive since it allow to conjugate at the same time the reduction of spurious modes and the increment in terms of frequency which is the objective of this thesis. Some of the simulation results are visible in figure 2.16 to highlight the trend. The plots are coherent with the expectations since the frequency is inversely proportional to the pitch and the impact of the spurious modes decrease with the pitch until an almost complete elimination have been performed in correspondence of small pitch(2.16 d). The only exception is constituted when, due to the variation of frequency related to the pitch reduction, the resonance frequency of the main mode become overlapped with an already present spurious mode which is not related to asymmetries or periodicity. In that case the spurious mode become much more excited degrading the frequency response. To do a further check of the previously explored solutions the same simulations have been repeated with the addition of the "Spacers" (2.17).The trend obtained is the same confirming another time the validity of the initial hypothesis.

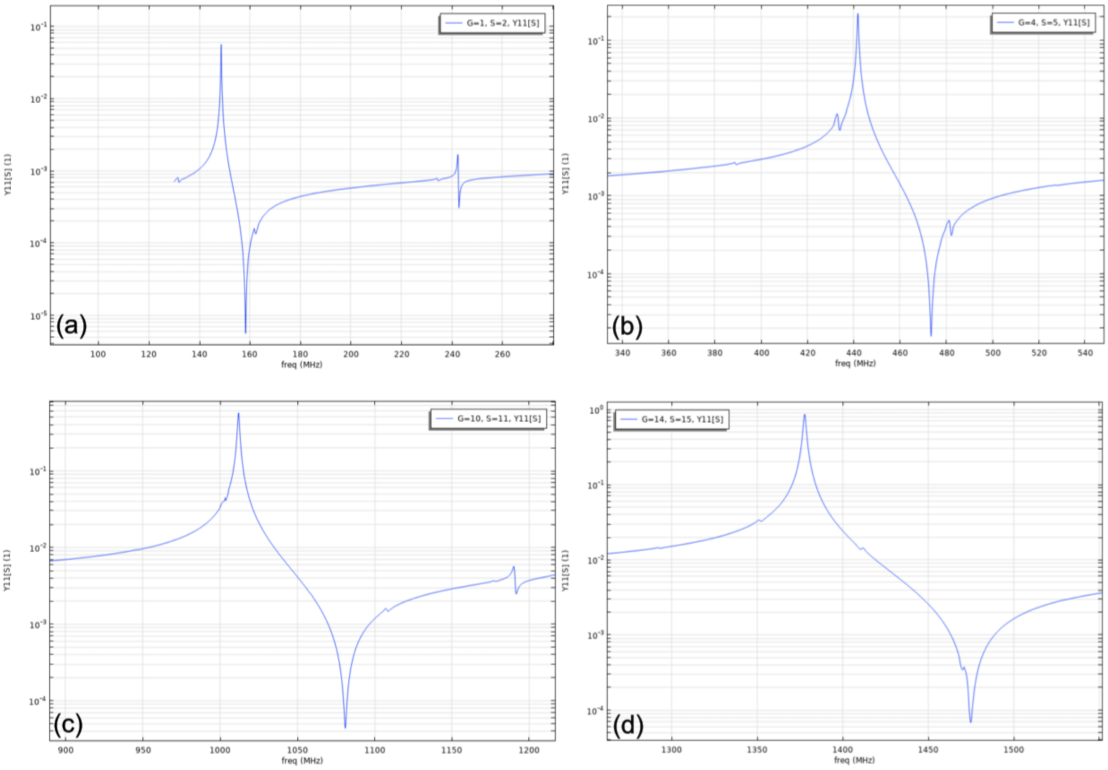


**Figure 2.16:** Admittance vs frequency graphs with $W_{res} = 60\mu m$ with $P = 20\mu m$ (a), $P \approx 6.67\mu m$ (b), $P \approx 2.86\mu m$ and $P \approx 2.1\mu m$.

Moreover, comparing the plot with the same pitch (2.16 (b) vs 2.17 (a) and 2.16 (d) vs 2.17 (b))it is possible to observe that, coherently con the result obtained in the previous sections, the "Spacers" reduces the asymmetry of the system decreasing the spurious impact at the cost of a slightly lower resonance frequency.

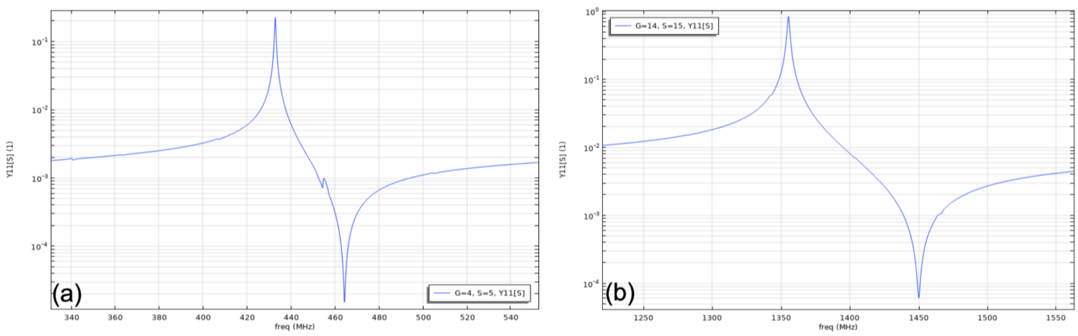


**Figure 2.17:** Admittance vs frequency graphs with addition of spacers having $W_{res} = 60\mu m$ and $P \approx 6.67\mu m$ (a), and $P \approx 2.1\mu m$

As a conclusion, this simulation was useful since it allowed to prove the initial hypothesis and it paved way to a resonance frequency increase. In fact, according to this simulation, the better results are achieved not only reducing the pitch, but also increasing the number of fingers inducing so the formation of a certain periodicity in the structure.

### 2.3.5 Periodic model

As highlighted in the previous simulations, increasing the number of fingers and excluding the edge of the resonator, it is possible to individuate a periodic structure. Hence, if the number of fingers if high, the impact of the mechanical boundaries at the edge is low or negligible. For this reason the whole resonator can be simulated through a periodic model constituted by a single cell. To realize this model it is necessary to build a basic cell following the previously explained conditions and selecting the wanted pitch as it has been done for $P = 20\mu m$ in figure 2.18. To make it work properly it is necessary to add periodic boundary condition containing the wave vector k to both domain (electrical and mechanical). Where k correspond to :

$$k = \frac{2\pi}{\lambda} = \frac{\pi}{P} \tag{2.3}$$

Hence this value allow to associate to the model the correct wavelength $\lambda$ excited by this pitch.

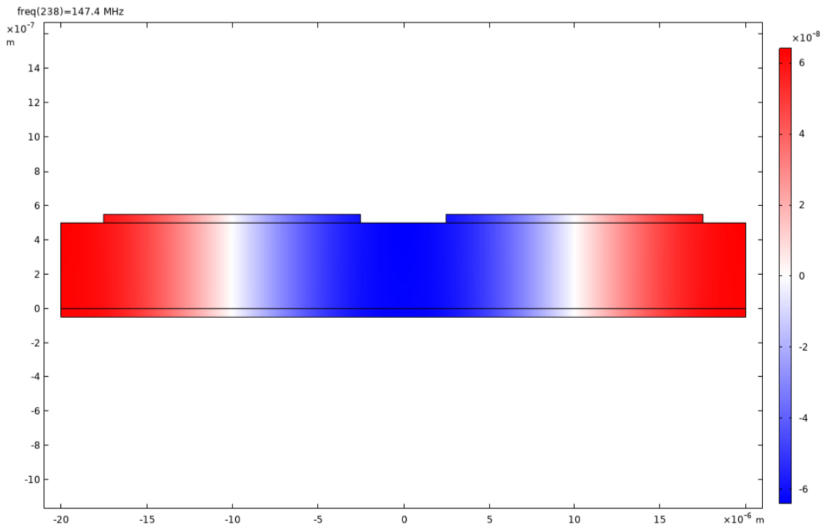


**Figure 2.18:** Geometry and mode shape at resonance (displacement in x direction) of periodic model for pitch $P = 2\mu m$.

The resulting frequency response obtained from this model is visible in figure 2.19

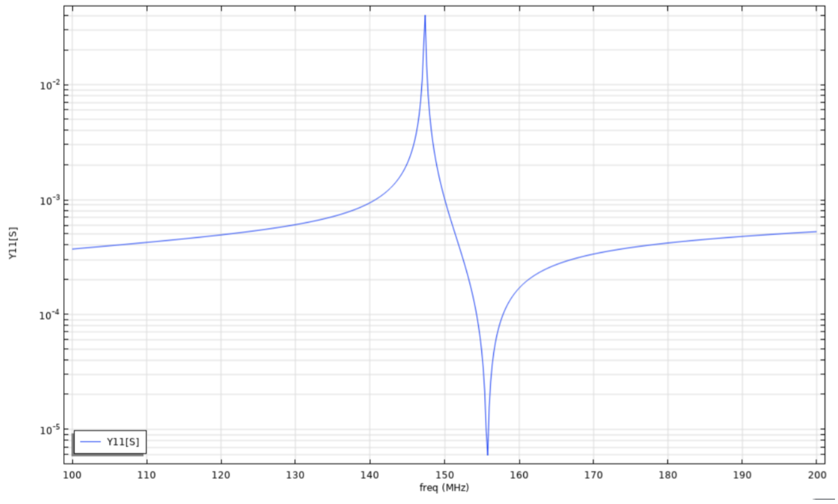


**Figure 2.19:** Geometry and mode shape at resonance (displacement in x direction) of periodic model for pitch $P = 2\mu m$.

The resonance frequency coincides with the expected (reference model in figure 2.2) with an error of 0.9 MHz which is acceptable considering the variability that we will have in real devices. Moreover, comparing the plot to the one previously obtained, it is possible to see that the spurious modes completely disappear making the plot more similar to the result obtained in figure 2.15 (d) rather than the reference model in figure 2.15 (c). This is perfectly coherent with the expectation since the assumption related to a perfectly periodic structure is much more realistic in a 19 fingers resonator than in a 3 fingers one. However, being this 19 fingers resonator extremely wide, it is more useful to exploit the periodic model for smaller pitches. Another important observation required in the comparison between the reference model (fig. 2.2) and the periodic one (fig. 2.19) is related to the behaviour of the spurious modes. In fact, the absence of the them in the periodic model suggest that the their presence is associated to the presence of boundary at the edges of the resonator confirming the hypothesis done in the previous simulations. However, this does not exclude the possible role played by the mismatch in terms of stiffness and the solution provided by the spacer, since they could be useful in a real device where the boundaries exists and cannot be neglected. Concerning the practical application of this periodic model, it is extremely useful due to low computational cost, and, if the advantage is not so important in 2D simulations which are already quite fast, it will be crucial moving to 3D simulation that, without this solution would have been extremely long.

## 2.4 Cross sectional Lamè mode resonator

As previously explained in the chapter 1 the CMR constitute a promising solution in the context of filter fabrication. Their main advantage is the possibility to easily tune the resonance frequency modifying the layout through a modification of the pitch. This is possible since, in this kind of devices, the application of a vertical electrical field through the fingers allow to excite the lateral mode of vibration S0. This is done thanks to the piezoelectric coefficient $d_{31}$, however this coefficient, compared to the $d_{33}$ (the one associated to a vertical excitation), is intrinsically smaller. This lead to the fact that devices that exploit the thickness excitation through the $d_{33}$ coefficient such as FBAR exhibit higher performance in terms of $K_t^2$ and are so preferred in many application such as filtering. A possible solution to overcome this gap is represented by the Cross-sectional Lamé mode resonator (CLMR) [27]. This kind of solution are basically constituted by standard CMRs (both LFE and TFE are valid) in which the thickness of the piezoelectric layer $T_{piezo}$ have been matched with the excited wavelength in the horizontal direction $\lambda_x$. In this way, when the resonance frequency of the lateral S0 mode matches the one of the mode propagating in the thickness direction, both the $d_{31}$ and $d_{33}$ coefficient are exploited and the $k_t^2$ is boosted, even if, also in this case, the upper reachable limit will be constituted by the piezoelectric coupling constant $K^2$ which represent the coupling limit for the piezoelectric material. Neglecting the presence of metal at the top and bottom of the resonator it is possible to compute the thickness wavelength ratio which allow to match the two frequencies through the formula[27]:

$$\frac{\lambda_x}{T_{piezo}} = 2\sqrt{\frac{(C_{11} - C_{55})}{(C_{33} - C_{55})}} \tag{2.4}$$

Where the $C_{xx}$ coefficient are the element of the elasticity matrix and $\lambda_x$ is the horizontal wavelength and correspond to $\lambda_x = 2P$. It is important to remember that, in a real device the presence of the metal is going to modify the sound velocity in the resonator, therefore, the real value of the ratio is going to be different from the one computed. Moreover, observing this equation it is important to notice that the ratio is dependent on the choice of the piezoelectric material. Many analysis have already been performed for the Aluminum nitride (AlN) obtaining $T_{AlN}/\lambda_x$ ratio of 0.5 for CLMR and below 0.2 for standard CMR, this means that, due to the strongly dispersive characteristic of Lamb waves, the shape and displacement of the S0 mode change a lot with the $T_{AlN}/\lambda_x$ ratio[28]. The aim of this section is to find the ratio which exhibit the best $k_t^2$ and find the ranges in which the resonator mode shape can be associated to CMR or CLMR for AlScN piezoelectric layer. To do that two different approach have been performed: a dispersion relation study and an experimental approach through the use of simulations.

### 2.4.1 Band diagram study for CLRM

Applying the formula 2.4 in the case of AlScN using the values previously obtained in the ANEMS Lab and used for the Comsol simulations, the obtained result is :

$$\frac{T_{AlScN}}{\lambda_x} = 0.34$$

Considering the usual thickness of our simulations $T_{AlSnN} = 500nm$, the obtained pitch is $P = \lambda_x/2 = 735nm$. To verify if this value belongs to CLMR it is possible to analyze the phase velocity comparing it to $T_{AlScN}/\lambda_x$ ratio as it is possible to see from figure 2.20 focusing on the S0 plot. Here the phase velocity exhibit a flat shape in the range where it behaves as standard CMR and then a decrease occurs moving in the CLMR range.

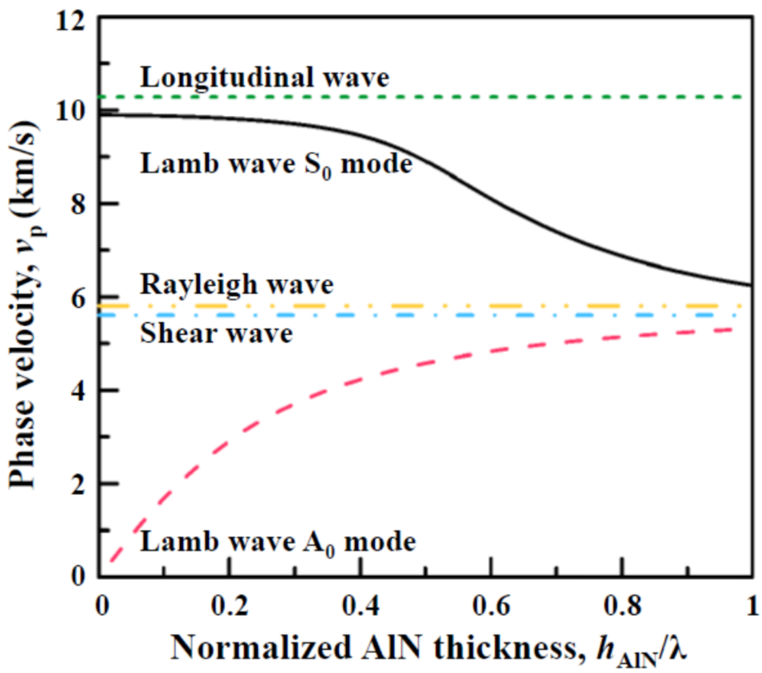


**Figure 2.20:** Phase velocity versus $T_{AlScN}/\lambda_x$ for AlN CMR [29].

Hence, exploiting the periodic 2D model with spacers the dispersion relations have been analyzed obtaining the result in figure 2.21 (also the result without spacers has been considered but there aren't significant variation in terms of main mode mode shape making this analysis valid for both cases) :

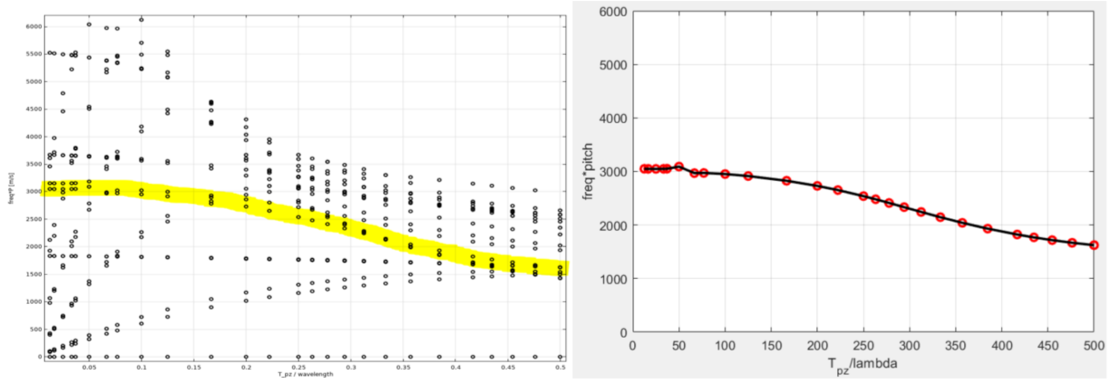


**Figure 2.21:** Phase velocity (P*$f_{res}$) vs $T_{AlScN}/\lambda_x$ ratio in AlScN resonator (left) and shape of the S0 mode (right).

As it is possible to see, the range of $T_{AlScN}/\lambda_x$ ratio is different since the result of formula 2.4 with AlScN is lower, however the behaviour of the S0 plot, obtained verifying the shape of the modes step by step is the same. This dispersion curve suggest a CMR behaviour from 0.01 up to 0.2 and then a gradual change until the CLMR one is reached. To evaluate the changes in shape of the mode it is sufficient to observe the figure 2.22 where on the left is represented the CMR shape obtained with a $T_{AlScN}/\lambda_x$ ratio of 0.1 ($P = 2.5\mu m$) and on the right is represented the CLMR mode shape with a ratio equal to 0.385 ($P = 0.65\mu m$).

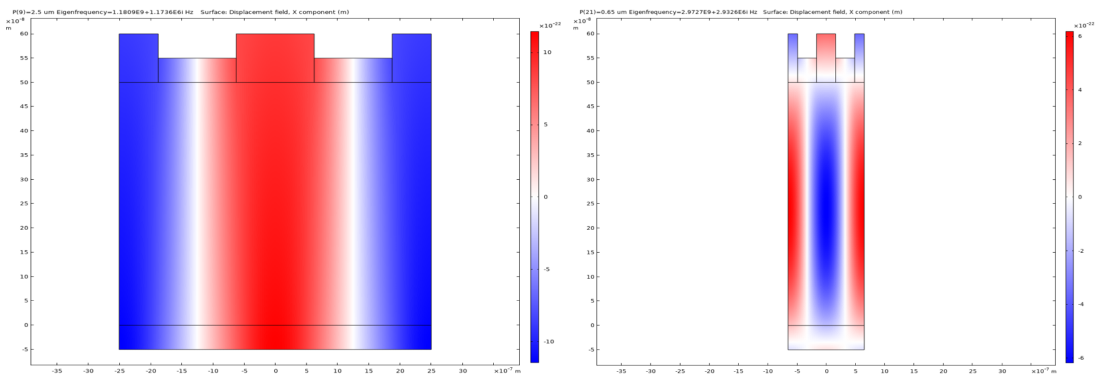

**Figure 2.22:** Displacement in x direction of CMR (left) and CLMR (right).

It is important to highlight that the shape visible in the two images is quite similar because the two modes are in reality a single mode that change its shape due to the progressive increase of matching between lateral and thickness modes which, in the case of displacement in the x direction, lead to the formation of two a horizontal nodes around the interface between AlScN and metal. Once that the mode shape associated to the two ranges is clear, it is possible to verify if the ratio predicted by the formula 2.4 is correct visualizing the mode shape for a $T_{AlScN}/\lambda_x$ ratio of 0.34 (The result has been approximated from $735\mu m$ to $750\mu m$):

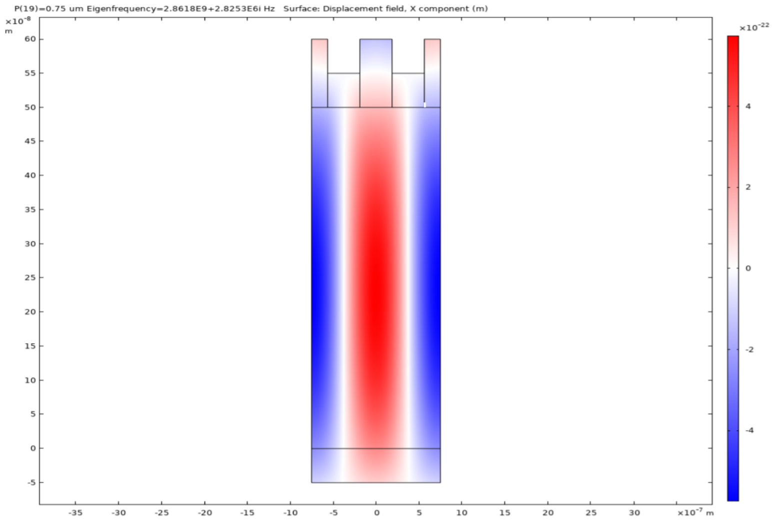


**Figure 2.23:** Displacement along the x direction for $P = 750\mu m$

Observing the shape of the mode, even if a change at the top of the resonator is observed respect to the standard CMRs mode shape, the result seems to be still in the transition between the shape previously presented in figure 2.22. However the formula 2.4 can still be considered as affordable for the identification of the correct dimensions for the excitation of the CLMR mode since, differently from the initial assumption, in the performed simulation both metal fingers and dielectric spacers have been accounted in the simulations.

### 2.4.2 CLMR and $k_t^2$ optimization

Thanks to the previous simulation the mode shape and the displacement behaviour of the CLMR resonator have been showed. According to the theory associated to the piezoelectric elements, the combined excitation of the $d_{31}$ and $d_{33}$ piezoelectric coefficient should provide the best results in terms of electromechanical coupling, however, considering a real case, this assumption might not be true. In fact, adding to the considered structure, top and bottom metal, some variation are possible and the CLMR might not be the best solution for this purpose. Moreover, further variations are possible depending on the the configuration of the resonator (LTE or TFE). An example about this variation of the optimal $k_t^2$ for AlN can be observed in figure 2.24

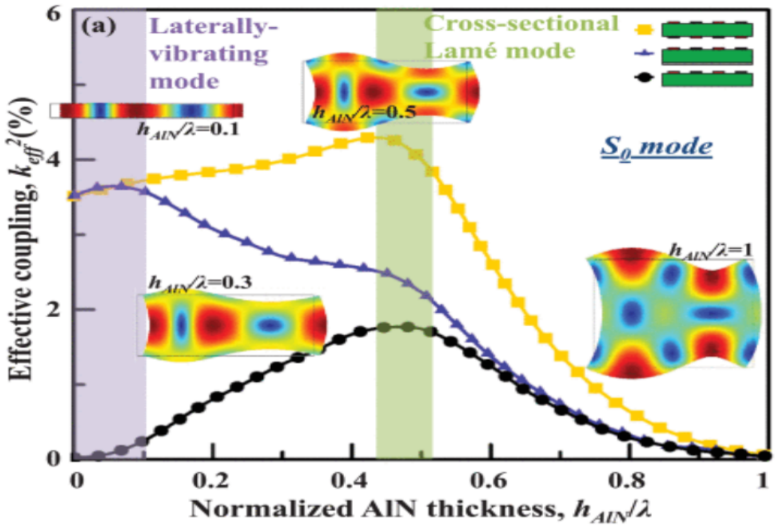


**Figure 2.24:** Electromechanical coupling behaviour respect to $T_{AlScN}/\lambda_x$ ratio for S0 mode in AlN resonators for different configuration of metal fingers [28].

Analyzing this graph it appears clear that, for the AlN LTE resonator considered, the highest coupling is reached in the standard laterally vibrating mode. Hence, the aim of the following simulation is to find the optimal $k_t^2$ for the studied AlScN based resonator. To do that, in a way similar to what has been already done in the "Spurious modes vs pitch" section, the width and the thickness of the resonator have been fixed to $W_{res} = 60\mu m$ and $T_{AlScN} = 500nm$, the number of fingers have been increased maintaining the usual excitation conditions. This means that the pitch and consequently the wavelength $\lambda_x$ have been reduced and the $T_{AlScN}/\lambda_x$ ratio progressively increased. In this condition, for every pitch, the electromechanical coupling have been computed using the formula 1.12:

$$k_t^2 = \frac{\pi^2}{4} \cdot \frac{f_s}{f_p} \cdot \frac{f_p - f_s}{f_p}$$

The result, split to lower the computational cost have been reported in figure 2.25

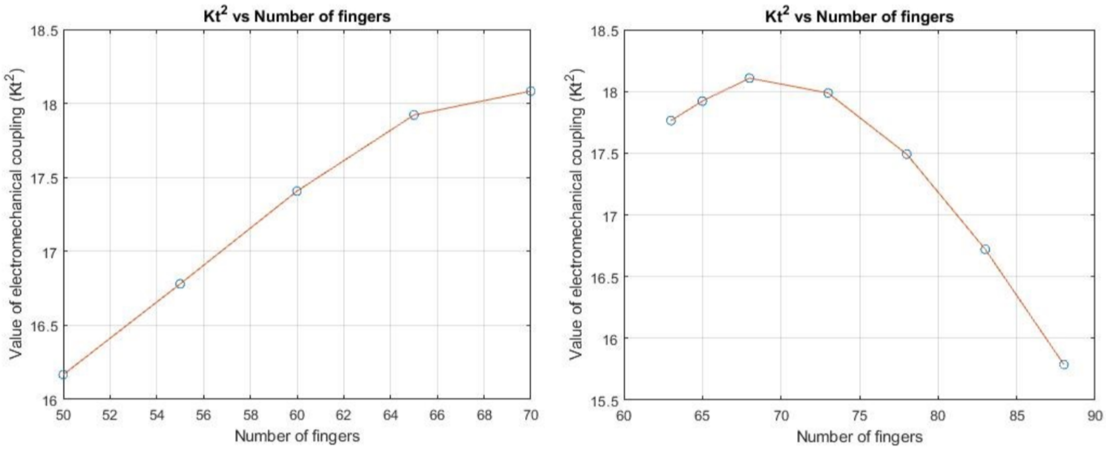


**Figure 2.25:** $k_t^2$ vs number of fingers with $W_res = 60\mu m$ and $T_{AlScN} = 500nm$.

Then, performing a further zoom around the peak the best coupling have been found for 70 fingers which correspond to a pitch $P \approx 850nm$ and to a $T_{AlScN}/\lambda_x$ ratio equal to 0.294. This result, considering the presence of the top metal fingers and of the bottom plate, is coherent with the 0.34 previously computed through the equation 2.4, however, to do a proper comparison, it is interesting to observe the mode shape for this pitch obtained from the previous simulation:

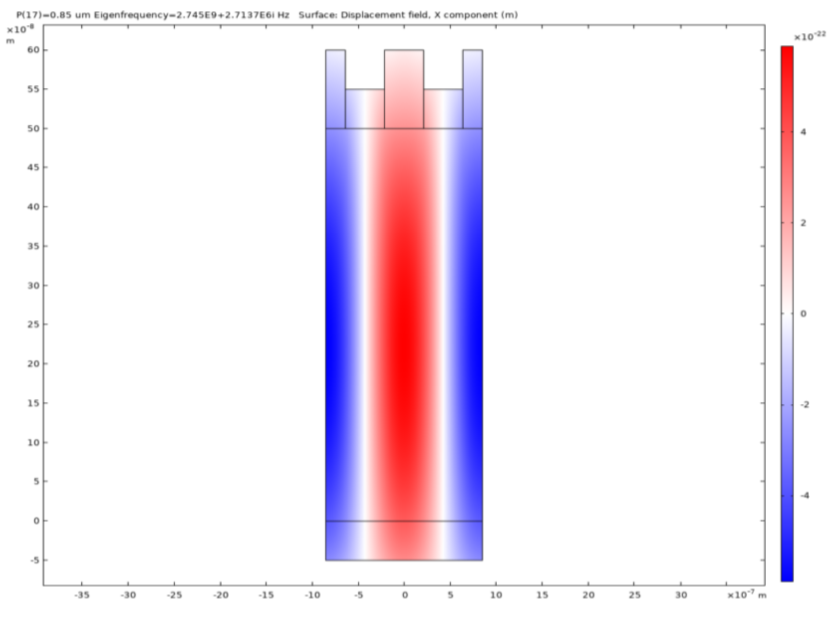


**Figure 2.26:** Displacement along x direction for $P = 850nm$ and a $T_{AlScN}/\lambda_x$ ratio equal to 0.294.

Analyzing this image it is possible to notice that the mode is still more similar to a lateral mode, however is already possible to see some changes towards the typical CLMR mode. This mean that, in our device, the optimal configuration seems to be an hybrid configuration between the standard lateral CMR mode and the CLMR mode. This information is useful to comprehend the behaviour of the device and to make the optimal choice in terms of layout.

### 2.4.3 $k_t^2$ vs electrical coverage

The previous study on CLMR allowed to find the best $T_{AlScN}/\lambda_x$ ratio for the optimization of the electromechanical coupling. However, as explained in the previous simulations, also the metal on top has an impact on the coupling of the resonator. Hence, to further optimize the design, it is interesting to simulate the device modifying the electric coverage EC (formula 2.2). To do that, with the usual choices of $W_{res} = 60\mu m$ and $T_{AlScN} = 500nm$ the EC coverage has been evaluated in a range between 35% and 85% for a pitch $P = 880nm$ ( around the optimal $T_{AlScN}/\lambda_x$ ratio obtained before) obtaining:

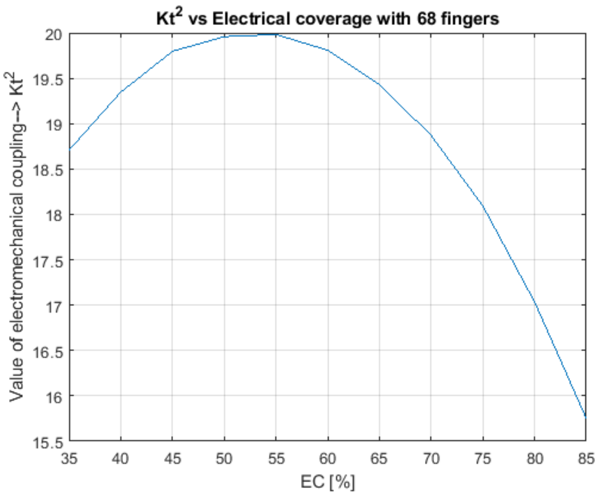


**Figure 2.27:** Behaviour of $k_t^2$ respect to the electric coverage for $P = 880nm$

As it is possible to observe the optimal coverage is obtained around $50 - 55\%$ instead of the usual 75% that has been used until now starting from the reference model. This might means, and it has been verified through other simulations not reported here to avoid redundancy, that the optimal electrical coverage tends to decreases increasing the number of fingers for a fixed width. Hence, considering the result in figure 2.27 and that the aim of the project is to increase the resonance frequency decreasing the pitch size, in the further analysis the electric coverage will be set to 50%.

# Chapter 3

# 3D Simulations

## 3.1 Simulation matching

The 2D simulations represent a useful tool since, thanks to their low computational cost, they allow a rapid investigation of the device properties, however, being two dimensional, they can represent only a section of the device. In our case the resonator has been cut along the axis of propagation of the main mode, therefore the model is able to represent correctly the resonance behaviour and the spurious associated to the section, but it cannot show the phenomena associated to the perpendicular direction. Hence, in order to have a behaviour more similar to the real case, it is necessary to move to the 3D analysis. To do that, the reference model have been realized following the previously fabricated device:

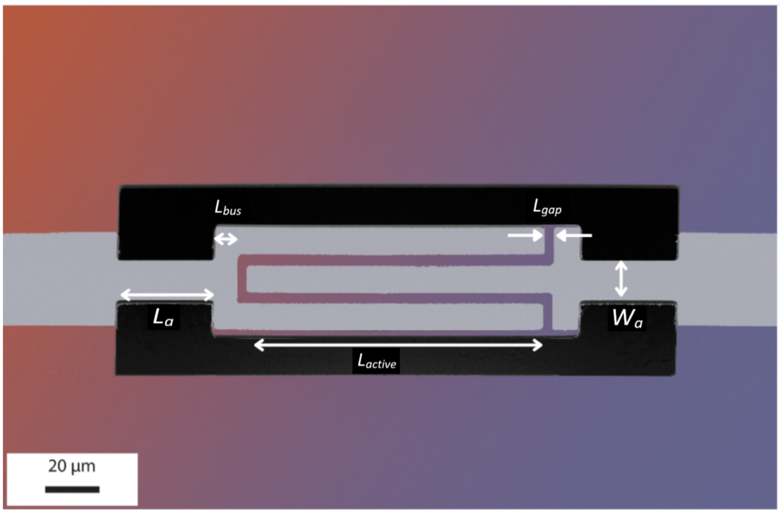


**Figure 3.1:** Image of the previously fabricated device at the optical microscope.

The parameter used were the same previously mentioned in the 2D simulation with the addition of length of the bus (which is the metal that provide the signal to the fingers) equal to $L_{bus} = 10\mu m$ and length of the gap (which is the space between metal and fingers) set to $L_{gap} = 3.75\mu m$, whereas the anchors (which link the resonator to the substrate) have been neglected in the simulations. So the finite element model has been realized, but, due to its high computational cost, a periodic model containing a single cell and Floquet periodicity condition, as previously done in the 2D section, has been built. To confirm the accuracy of these new models their admittance plots have been compared with the 2D one as it is possible to see in figure 3.2.

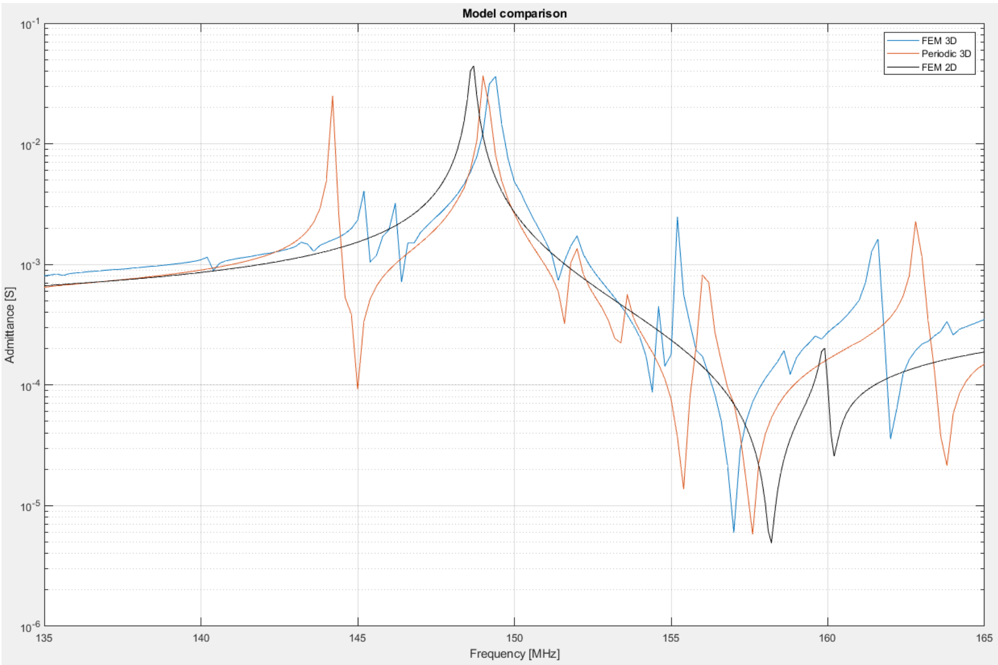


**Figure 3.2:** Admittance comparison of 2D, 3D and 3D periodic models.

Comparing 2D and 3D plots it is possible to see the that, going to a 3D model, the frequency of the device is increased, however, being the change among the 3 models below 1MHz the results are perfectly coherent. Considering the anti-peak, the opposite behaviour is observed leading to a smaller peak to anti-peak distance and consequently to a smaller $k_t^2$ for 3D. Also in this cases the two plots matches since the position of the anti-resonance in the 3D model is influenced by the presence of spurious modes. Having verified the matching between the plots, the main difference is represented by the amplitude and quantity of spurious. In fact, the 2D plot exhibit only a single spurious mode whereas the 3D ones shows many of them. Some of this peaks are related to asymmetric modes typical of

Lamb wave resonator (not only along the sections like discussed in the previous chapter) but many of them to transverse spurious mode on which a study will be performed to attempt their elimination. Regarding the comparison between 3D FEM and periodic models, the first shows a higher number of spurious modes while the second a lower number of them but with higher amplitude. A possible explanation could be related to the fact that, like it has been previously observed in 2D, increasing the number of fingers some unwanted modes are eliminated due to the lower importance of the mechanical boundary associated to the width of the resonator, but the coupling of the remaining transverse spurious mode is probably enhanced by the periodicity of the structure. Hence, since the progress of the projects will be devoted to scale up the frequency reducing pitch and increasing the number of fingers, the periodic model is going to be much more affordable in the future simulations, but this highlights even more the necessity to find solutions to remove or attenuate the effect of transverse spurious modes.

## 3.2 Transverse spurious modes

Given the CMRs resonator in figure 3.3, as previously demonstrated in section 2.2, the resonance frequency is determined by properly matching its electrical and mechanical boundary conditions exciting the lateral mode (S0).


**Figure 3.3:** Schematic image of a CMR resonator with 3 fingers

In the ideal case, considering an excitation exactly at the resonance frequency $f_{res}$ and an infinite resonator, the S0 mode is excited only along the x direction. This means that the wave vector $k_{tot}$ has only its x component different from zero ($k_x = k_{tot}$ and $k_y = 0$). Where $k_x$is defined as:

$$k_x = \frac{2\pi}{\lambda} \tag{3.1}$$

In this case the wave is going to propagate only along x direction with a phase velocity which can be computed by inverting the formula 1.2 :

$$\nu_{S0} = f_{res} \cdot 2P \tag{3.2}$$

Hence, once a material has been chosen, the velocity is fixed. Considering a real device, the excited frequency $f_{real}$ is deviated respect to $f_{res}$ since the resonator is finite and has mechanical boundaries which alter displacement and stress at the edges of the device, moreover, in practical applications such as filters, the excitation frequency can be different respect to the resonance one. Therefore, assuming $f_{real}$ slightly higher than $f_{res}$, for the formula 3.2, $\nu_{S0}$ is supposed to increase, however this is physically impossible since the x component of the velocity in S0 mode cannot change. The only possibility to fulfill this condition for the wave is to start propagating outside the x axis having so $k_y \neq 0$. This means that, in a real case, the total wave vector is a superposition of the x and y components. So, as stated in [30],the condition for the generation of a transverse spurious mode, is linked to the relation between $k_y$ and the length of the active area $L_{active}$ which contains the fingers:

$$k_y = \frac{\pi \cdot (n+1)}{L_{active}} \tag{3.3}$$

Where n is the order of the transverse mode. Hence the transverse spurious resonance show a dependence related to the length of the active area. In fact, as it is possible to see in figure 3.4, reducing the length of the device ($L_{active}$) the number of spurious modes decreases and their amplitude increases:

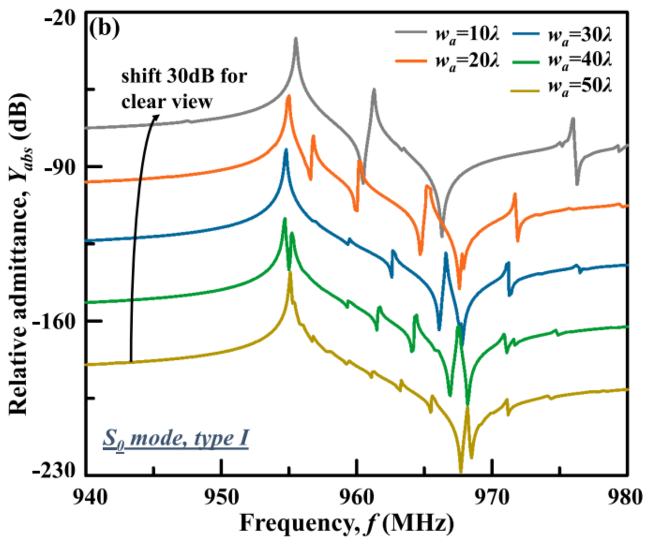


**Figure 3.4:** Admittance plot for different $L_{active}$ ($W_a = L_{active}$)[30].

The explanation to this phenomena could be related to the fact that, with longer devices, there are more $k_y$ which met the propagation condition 3.3 and so an higher number of unwanted peaks, but, at the same time, their impact is going to be less significant in the $k_{tot}$ computation performed through the superposition of $k_x$ and $k_y$. Moreover, as stated by [30], below $L_{active} = 10\lambda$ the $k_y$ starts to contribute directly for the propagation of the main mode. Hence, as a first approach, $L_{active} = 10\lambda$ will be considered as a design limit to preserve the the performance of the device while some solution will be explored to improve the situation from the spurious point of view.

## 3.3 Design considerations and n28 band

As previously said the aim of the thesis is related to the increment of the resonance frequency of the devices performed through the reduction of the size of the pitch. However, since a gradual change in terms of dimension would be easier to manage, to start the 3D design approach of new devices the band n28, whose frequency range is comprised between 703 and 748 MHz (pitch around 5 times smaller than the reference), has been chosen as a target. Here some design choices have been made to complete the design:

- The electric coverage EC has been set to 50% since it falls in the optimal range obtained in 2D simulations (section 2.4.3) and allow to maximize the symmetry of the system.

- The active area length ($L_{active}$) has been set to $10\lambda$ to minimize the number of spurious without degrading the electromechanical coupling.

- The length of the bus $L_{bus}$ does not represent a crucial parameter since the electric resistance is not taken into account and so it has been set equal to the wavelength to reduce the computational costs, but in reality it will be bigger.

- Concerning the length of the gap ($L_{gap}$) it has been set equal to the value of the wavelength. This has been done since to achieve the best performances it is necessary to confine the wave as much as possible in the active area limiting the transfers of energy to the bus. In fact, due to the presence of metal, the bus exhibit a lower acoustic velocity and, being it also connected to the substrate, it represent also a source of energy dissipation[30]. Hence after many simulations, the choice $L_{gap} = \lambda$ has been done guaranteeing the confinement and also additional space for purpose explained in the next sections.

- To limit as much as possible the transfer of energy from the active region to the bus it is necessary to increase as much as possible the acoustic discontinuity between the active region and the bus. For this reason, in addition to the absence of one of the fingers for each base cell the bottom metal has been removed both below gap and bus.

### 3.3.1 Materials for electrodes

Before defining the pitch it is necessary to chose the material employed in the fabrication since, through their mechanical properties, they play a critical role in the definition of the resonance frequency. Hence, having already chosen the AlScN as a piezoelectric material, it is necessary to modify the metal layers. Regarding the bottom metal, the selection of platinum here is necessary since it is fundamental for the growth of an high quality piezoelectric layer, but, since the device considered is an LTE CMRs it is not used to provide signal and its thickness can be so reduced from 50nm to 30nm. In this way the layer is thick enough to enhance the quality of the AlScN and, at the same time, having reduced the mass loading, the resonance frequency of the device increases. Concerning the top electrodes there are no restrictions and so, many possibilities can be considered. Among those the aluminum has been selected (here it is possible to see its comparison respect to platinum):

| **Material** | **Electrical resistivity** | **Young Modulus** $E_{eq}$ | **Density** $\rho_{eq}$ |
|---|---|---|---|
| Platinum | 105 n$\Omega m$ | 168 GPa | 21450 kg/$m^3$ |
| Alluminum | 26.5 n$\Omega m$ | 68 GPa | 2700 kg/$m^3$ |

**Table 3.1:** Comparison between Platinum and Alluminum properties[15]

As it is possible to see from the graph, the Aluminum represent a better solution since it exhibit an higher $E_{eq}/\rho_{eq}$ ratio which means higher phase velocity and consequently higher resonance frequency (equation 1.2). Moreover the lower resistivity of this material reduce the impact of the electrical resistance $R_s$ on the quality factor augmenting the design possibilities (more EC and $L_{active}$ combinations). The only problem associated to this choice is related to the fact that a mismatch between top and bottom metal has been introduced. Hence, starting form 2D periodic simulations with $P = 4.4\mu m$ to meet the n28 band requirements, the thickness of the top metal layer $T_{top}$ has been swept between 50nm and 100nm in order to find the optimal one as it is possible to see in figure 3.5 (a). Here it is possible to notice that, despite the higher mass loading, increasing the thickness of Aluminum the frequency increases. The reason of this phenomena is probably related to the fact that the mass loading is probably balanced by the impact of aluminum density and Young modulus on the whole resonator. However, considering that this increase is negligible respect to the one associated to the change of material, as it is possible to observe in figure 3.5 (b), the best case is represented by setting $T_{top} = 50nm$ since it allows to eliminate the presence of spurious.

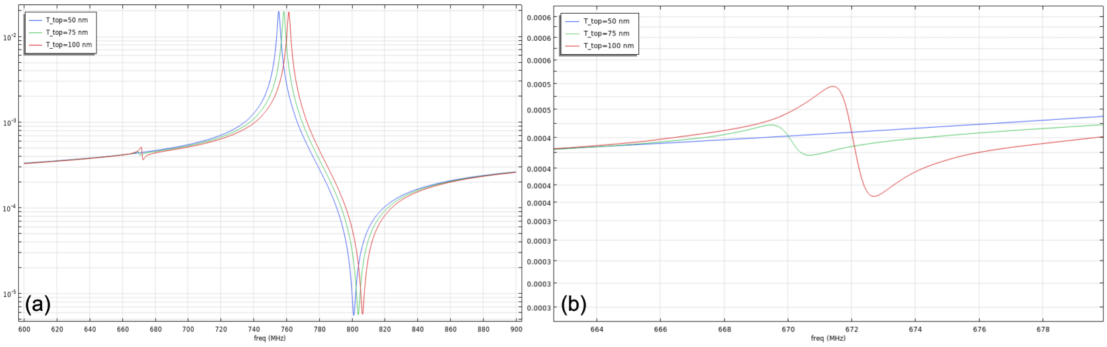


**Figure 3.5:** Admittance plot of the described resonator

Having eliminated the spurious from periodic 2D simulation means that a good balance between top and bottom of the resonator have been obtained. Hence, from now on the new reference will be: 30nm of platinum for the bottom metal and 50nm of aluminum for the top electrodes.

### 3.3.2 Admittance of the n28 band

Having defined all the design parameter and the material choices the 3D periodic model of the device can be built. In particular, for the n28 band the selected pitch is $P = 4.5\mu m$ which lead to $f_{res} = 740MHz$ as it is possible to see in the following figure:

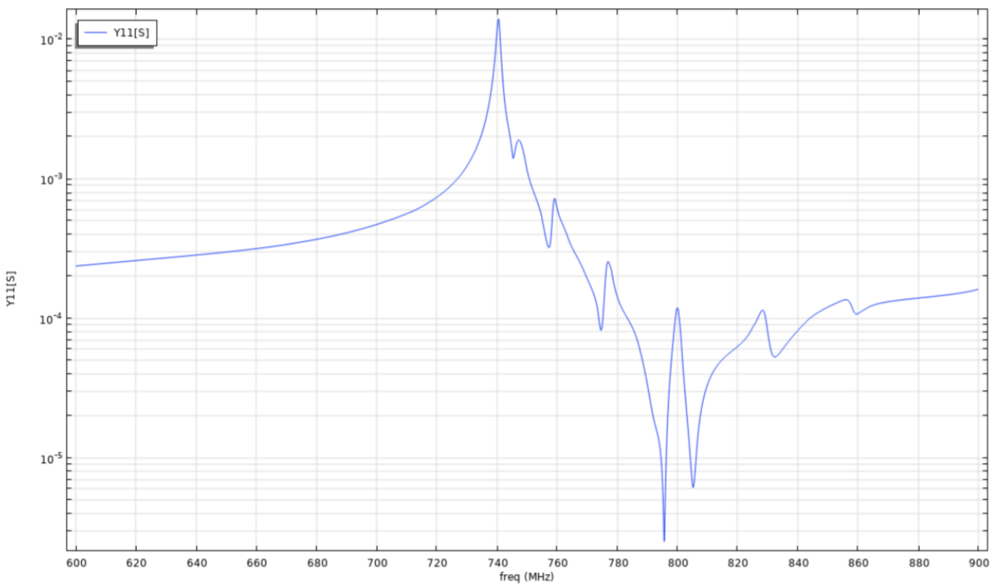


**Figure 3.6:** Admittance plot of the model designed for n78 band ($P = 4.5\mu m$)

It is important to notice that, to obtain valid information on the quality factor, the system should be simulated with perfectly matched layers (PML) which in this case have been neglected for simplicity. Hence in this simulations the quality factor has been set to 500 thanks to the application of a loss factor in the damping section. Observing the plot many transverse spurious modes are observed even if $L_{active}$ has been reduced to $10\lambda$ highlighting the necessity to find solution able to allowing their elimination.

## 3.4 Piston mode design

One of the possible solutions to improve the plot shape of the resonator is the introduction of the so called "Piston mode design". This solution is based on the enlargement of the fingers that lead to the formation of an "hammer head" at the end of the acoustic active region. The presence of this structure induces the reduction of the phase velocity and make the transverse wave vector $k_y$ of the propagation mode equal to zero in the gap between pistons and bus [31]. Hence the $k_y$ is real in the border region of the active area (from now on it will be called "Piston region") and become imaginary in the gap, so the amplitude of the wave is exponentially attenuated in this region. To better understand this behaviour in figure 3.7 the difference obtained through the introduction of the pistons is showed for what concern: design structure, acoustic velocity and displacement $u_{x,n}$ for the $n^{th}$ mode. As it is possible to see from the plot shape the presence of the piston allow to maximize coupling and displacement for the main mode, whereas considering the higher order modes, it is possible to see that the even modes having a finite multiple of the total wavelength in the active region cancel each other and do not couple to electrical domains [30]. The design method of these piston modes has been developed in the past for SAW and BAW devices and can be done in many different ways which mainly consist in :

- Increasing the electric coverage at the end of the active area
- Changing the metal thickness in the piston region
- Introducing a low velocity dielectric in the piston region
- Adding a high velocity dielectric in the active region without pistons.

In this project it has been decided to proceed modifying the electric coverage EC in the piston region, the procedure, in which electric coverage and piston length $L_p$ are optimized will be presented in the following section.

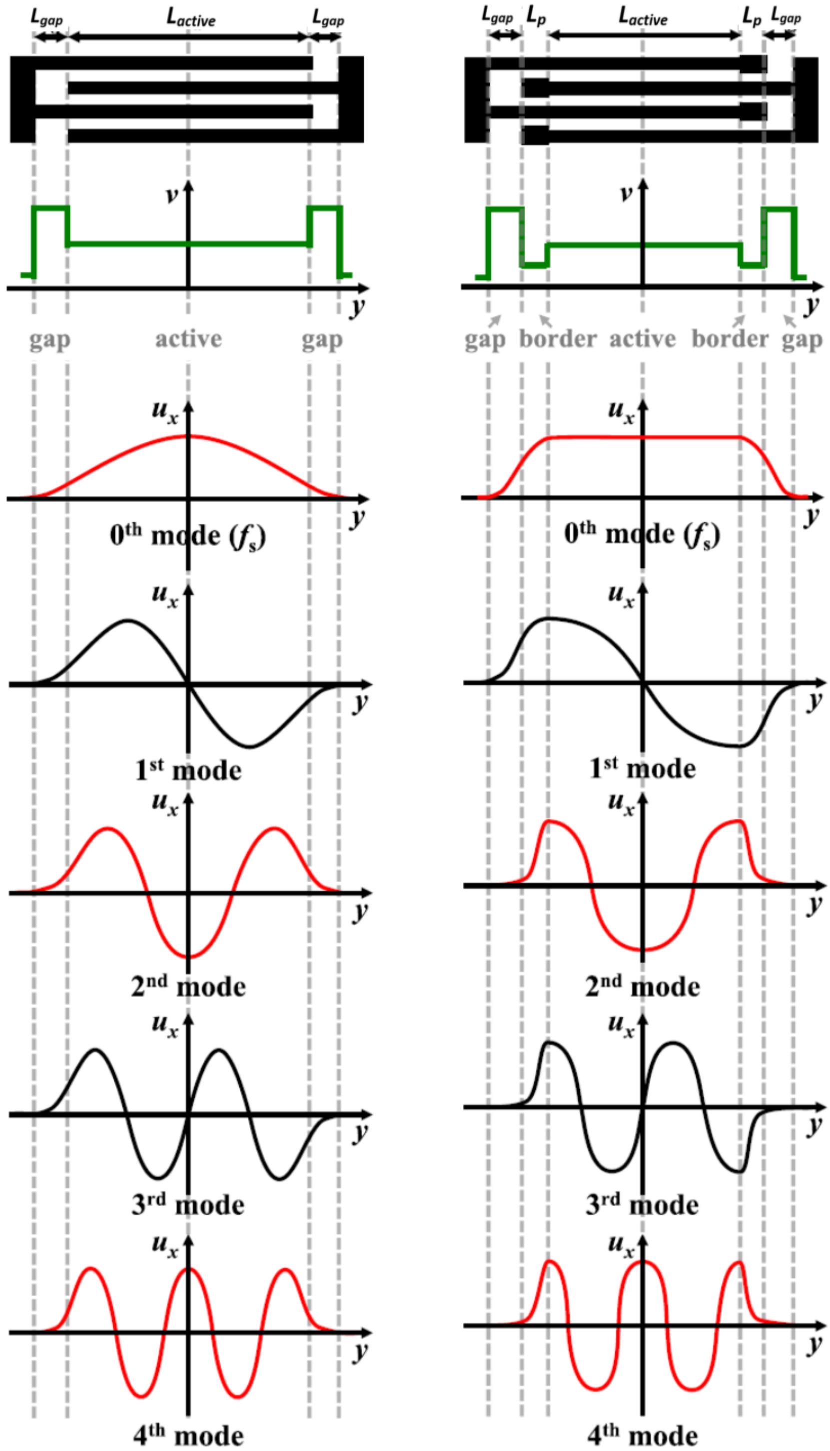


**Figure 3.7:** Velocity $\nu$ and displacement $u_x$ profile without (left) and with piston mode (right)[30]

### 3.4.1 Piston implementation

As previously mentioned the piston modes can be realized by modifying the electric coverage of the fingers in the pistons region at the border of the active area for a length $L_p$. To do that it is necessary to divide the device in three regions: active region where there is the propagation of the main mode, piston region where the electric coverage will be modified to reduce the sound velocity and gap region which separate the fingers from the bus (see figure 3.7 for reference). For each of these zones it is possible to define a transverse wave vector $k_y$: in the active where the main mode propagate it is assumed $k_y = 0$ and $k_x = k_{tot}$ since the wave propagate only in the x direction, in the others regions it is possible to define two transverse component $ky_{gap}$ and $ky_{piston}$ which are different from zero. Having clear this parameters, through the computations explained in [32], it is possible to obtain the formula:

$$L_p = \frac{\arctan(\frac{ky_{gap}}{ky_{piston}})}{ky_{piston}} \tag{3.4}$$

Hence, once the two transverse component of the wave vector have been obtained the length of the pistons region can be obtained. To get those two value it is necessary to define arbitrarily an electric coverage in the pistons region $EC_p$ keeping in mind that the objective is to reduce the phase velocity in the pistons area. Therefore in our situation the required condition is $EC_p > EC$ and, in particular, bigger is $EC_p$ smaller is going to be $L_p$. Starting from a standard coverage equal to $EC = 50\%$ the value of $EC_{piston} = 70\%$ has been chosen. Now through a periodic 2D simulation of the cell using the selected $EC_p$ it is possible to perform a mode analysis and obtain a band diagram plotting the real part transverse wave vector versus the frequency.

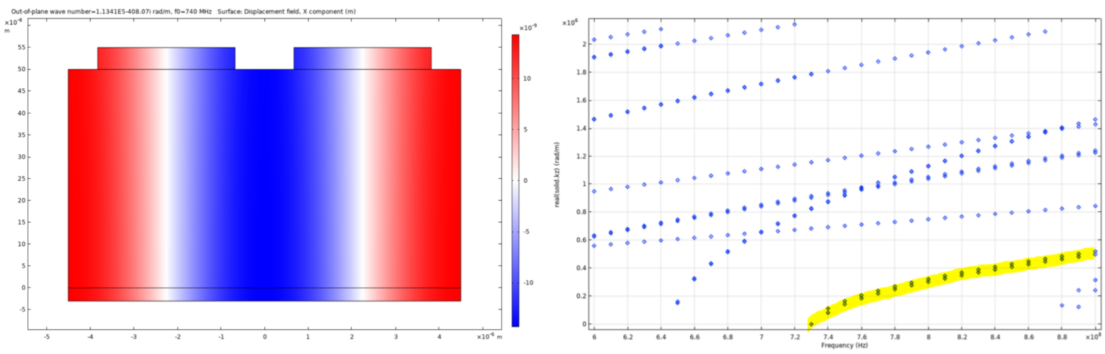

**Figure 3.8:** 2D periodic cell with piston representing the correct mode shape (left) and transverse wave vector (real part) vs frequency with main mode highlighted (right).

Here through the analysis of the mode shape it is possible to distinguish the S0 mode of the resonator (in yellow) that, due to the higher coverage, exhibit a lower resonance frequency. Hence, by selecting the value of the wave vector at the resonance frequency of the main mode, it is possible to deduce $k_{piston}$ (in both his components). In the same way, simulating the periodic cell which correspond to the gap it is possible to plot the imaginary part of the transverse wave vector respect to frequency:

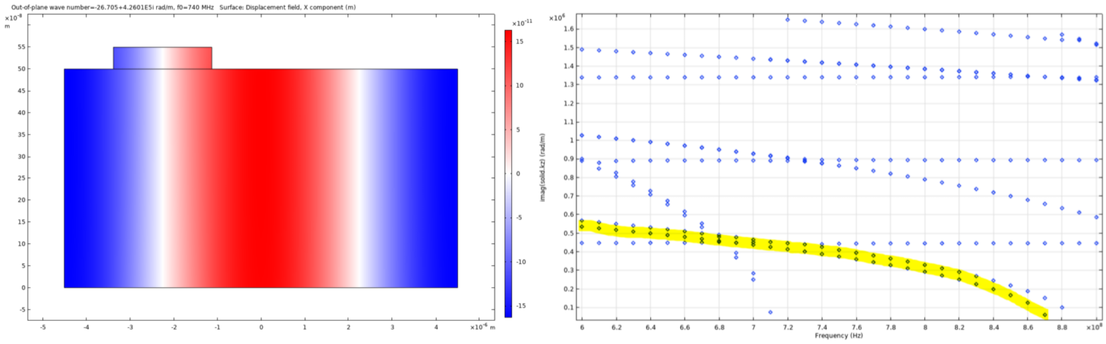

**Figure 3.9:** 2D periodic cell with gap representing the correct mode shape (left) and transverse wave vector (imaginary part) vs frequency with main mode highlighted (right).

In this case the mode will be at higher frequency due to the lack of a finger, but in the same way as before, it is possible to get the wave vector $k_{gap}$. The final situation can be resumed by the figure 3.10:

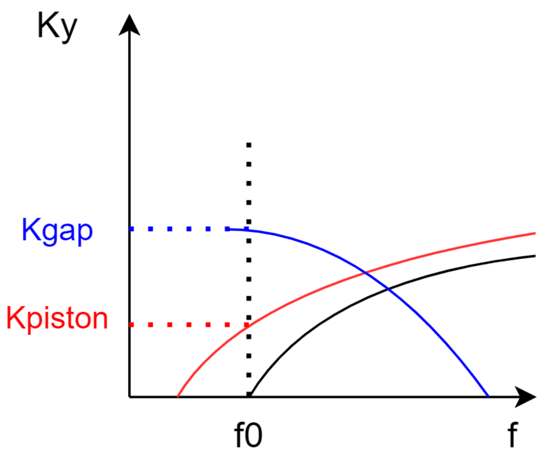


**Figure 3.10:** Qualitative representation of the results obtained from the band diagrams. (Note that for the gap the imaginary part instead of the real one has been plotted.

This procedure can be now applied to the device designed for the n28 band with a $f_{res} = 740MHz$ and $EC_p = 70\%$ obtaining $L_p = 11.5\mu m$ through the formula 3.4. Then the new cell with the addition of pistons has been simulated obtaining:

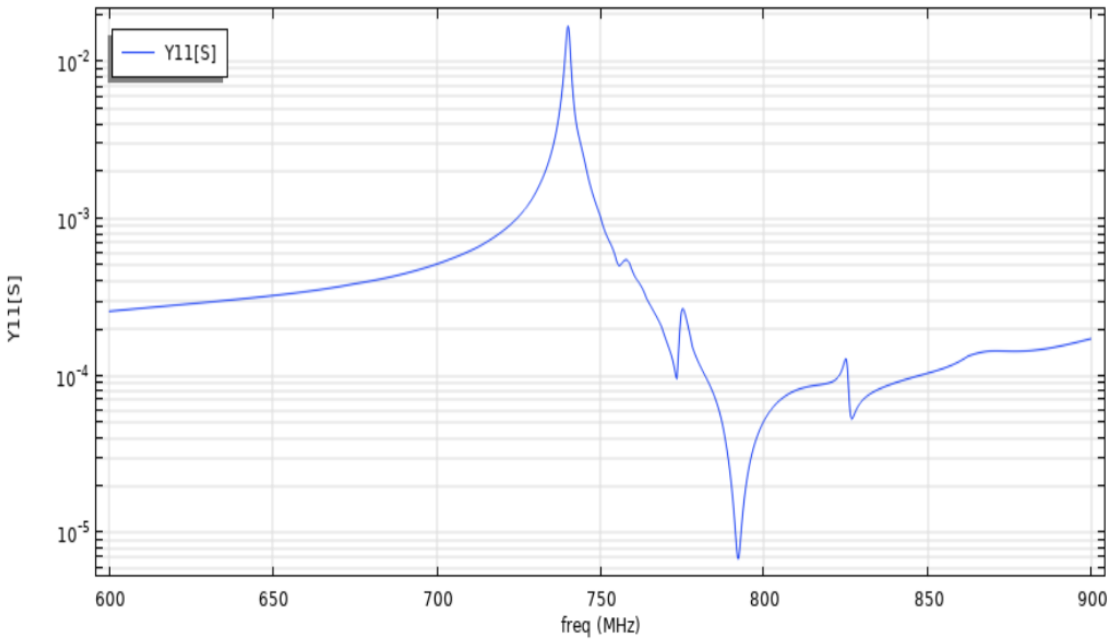


**Figure 3.11:** Admittance $Y_{11}$ plot of the device for band n28 9 ($P = 4.5\mu m$) with the addition of pistons ($L_p = 11.5\mu m$)

Comparing this plot with figure 3.6 it appears clear that the number of spurious modes, as well as their amplitude, have been strongly reduced without reducing quality factor and electromechanical coupling, proving so the effectiveness of this solution. However, it was not possible to completely eliminate the spurious mode presence from the admittance even with trying with different length of pistons. Hence, a further effort need to be done to perform a complete elimination.

### 3.4.2 Holes in the gap

The introduction of the pistons in the design have led to a significant improvement in terms of spurious modes impact, however some of them are still present and could disturb the correct behaviour of the resonator. Hence, a further modification has been done by performing holes through all the gap like the one visible in the following figure:

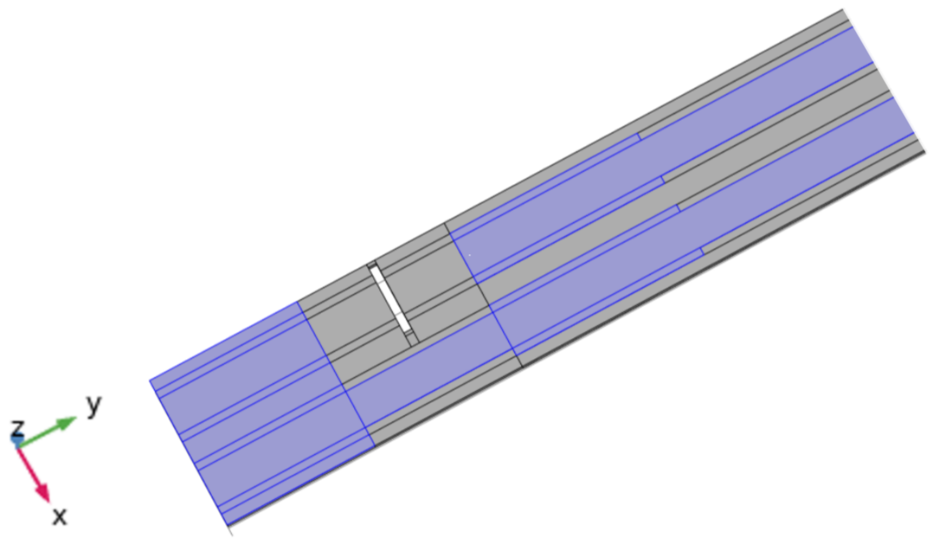


**Figure 3.12:** Edge of the cell of a n28 band resonator with a 500nm hole in the gap. In blue are represented the metal parts(Al) whereas in grey the piezoelectric ones

Depending on the size of the hole it is possible to compare the resonator along the y axis to an acoustic waveguide junctions and encounter two different cases:

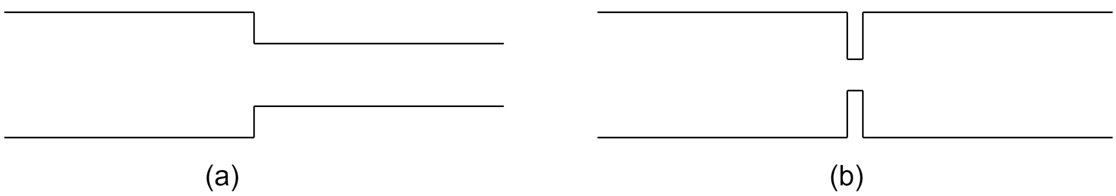


**Figure 3.13:** Two different cases of waveguide junctions: the first one (a) can be associated to long holes in the gap, whereas the second one (B) to short holes.[33]

In the case (a), which can be associated to a long hole in the gap, a new propagation region is realized along the hole, this lead to a complication in the study and so it will not be considered in the preliminary analysis performed here. In case (b) a small hole is introduced in the gap adding a source of reflection for the impinging wave. A proper theoretical demonstration about the the introduction of the hole still have to be developed but it is possible to give a rough explanation. In fact, in correspondence of the hole, the stress which is propagating with the wave is set to zero, therefore, in the zones without the holes, some higher order modes above the cutoff frequency are produced. This means that by properly choosing the distance between hole and piston it is possible to reflect part of the energy that would have been dissipated without degrading the admittance response of the resonator, because the higher order modes exponentially decreases before reaching the active region. A theoretical derivation to find the optimal configuration has not been obtained yet, hence, for the n28 band device the following values have been obtained through simulations: pistons-holes distance $Y_h = 1.3\mu m$, hole length $L_h = 1\mu m$ and hole width $W_h$ set keeping 200nm of margin respect to the border of the cell. Then, the new cell has been simulated:

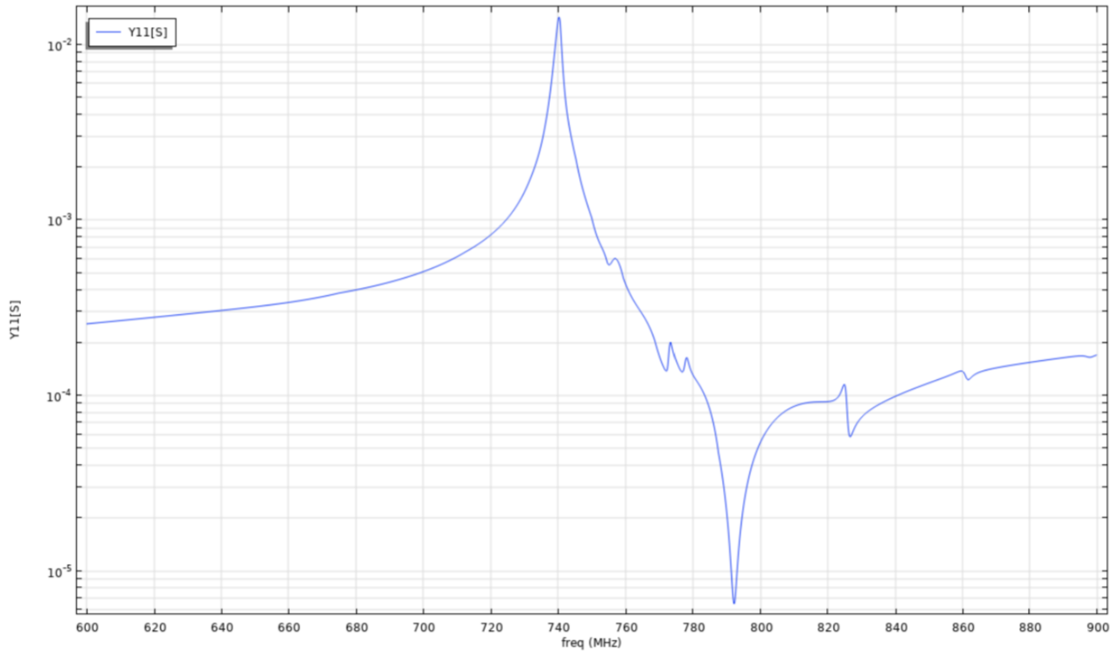


**Figure 3.14:** Admittance response vs frequency of the n28 band devices ($P = 4.5\mu m$) with the introduction of the gap in the hole

Comparing this plot with the one obtained with the pistons (figure 3.11) it is possible to see that the situation is pretty similar but, the amplitude of the spurious has been reduced. Hence the overall impact of this solution is positive (since can be implemented just by modifying the layout), but, at the same time, some work still have to be done to find a rigorous rule and the best possible configuration.

# Chapter 4

# Fabrication

After having defined the basis for a new design thanks to 2D and 3D simulations, it is important to define a process flow and consider all the possible issues in the fabrication of the device. One of the drawbacks associated to the employment of MEMS is related to the fabrication process that in some case can be quite challenging. Hence, for a good result, it is necessary to do all the required tests in order to have a process known as much as possible. In this chapter the main steps of the process flow are explained and, at the same time, new solution are evaluated.

## 4.1 Process flow

The process flow for this device, in line with other typologies of MEMS, requires several steps here, in figure 4.1, the most important ones are reported. Before starting with the steps it is important to remarks that, having a device which is oriented to possible application in the market, all the lithographic steps are performed exploiting the use of the DUV stepper that is able to guarantee, at the same time, higher resolution, alignment capability and throughput than the common lithographic methods. Starting the process, in the step 1) the alignment marks are performed on the backside of the wafer. This solution has been preferred respect to a standard front side alignment since, at the cost of a slightly worse misalignment (the maximum misalignment is 60nm instead of 25nm), it allow to align all the layers avoiding issues that could be associated to possible damage or reduced visibility of the marks caused by processes on top of the wafer. Therefore, for this process, a double side polished wafer is taken and the backside marks are exposed on the backside through the reticle provided by ASML. Then the marks are etched by high density plasma etching exploiting the SPTS Advanced Plasma System present in the Cmi (center of MicroNanotechnology).

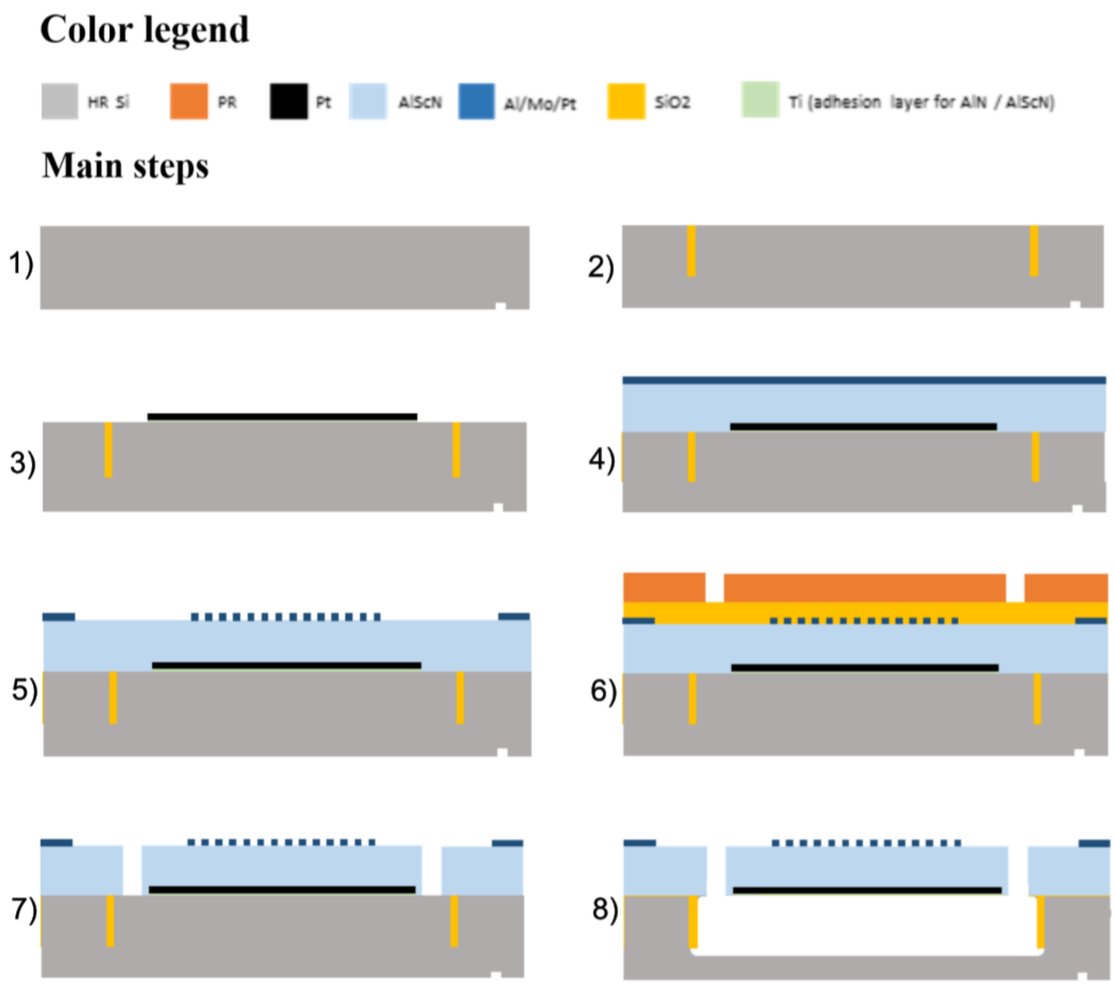


**Figure 4.1:** Main steps for the fabrication of the LTE CMRs.

The step 2) it is quite long, involving many intermediate step that will be explained better in the following section. Its aim is to realize some high aspect ratio trenches filled with Silicon dioxide ($SiO_2$) able to separate the Silicon below the resonator from the one in the rest on the wafer and, in particular, below the contact pads. In this way, when the release of the suspended resonator will be performed, the material below the pads will not be etched guaranteeing a good resistance of the pads during the probing of the device after the fabrication [34]. The following step (3) consists in the deposition, through sputtering, of the bottom metal plate, composed by a small Titanium adhesion layer and by the selected thickness of platinum. Then in step 4), exploiting the Pfeiffer Spider 600, the piezoelectric material (AlScN) and the top metal (Al) are sputtered in a single deposition session. It is important to notice that this step is particularly crucial since it is the responsible of the quality of the piezoelectric material and, consequently, of the electromechanical coupling of the final device. The following process (5) consist in the exposure and pattern definition of the top metal and the fingers through ion beam etching. From a lithographic point of view, it represent the critical step due to the resolution required for the fingers. In the two following two steps (6 and 7) it is represented the etching of the piezoelectric material to separate the resonator from the rest of the substrate. However, due to the scandium doping, the AlN become heavier and much more resistant to etchants, hence an hard mask is required to sustain the whole process. In order to try to remove the hard mask and ease this process some test will be performed and explained in the next sections. Finally, the last step (8) consists in the release of the suspended device by removing the silicon underneath the resonator using Xenon difluoride $XeF_2$.

## 4.2 Trench filling test

The step 2) of the image 4.1 is important since it allow to define a release area confinement. In fact the $SiO_2$, during the step 8) form a barrier which prevent the Silicon outside the release area to be etched. This is crucial since, in case of single device tested, it allow a correct probing of the pads (see layout in the next chapter) without the risk of collapsing and, in case another structures are present on the wafer, it is going to preserve the structural properties of the substrate ensuring their correct fabrication. An important requirement of this solution is that the trenches should be deep enough to allow the $XeF_2$ gas to completely release the structure without compromising the surrounding area. Considering the device for the n28 band (the biggest present in the layout discussed in the next chapter) the required depth is around $60\mu m$, but at the same time, the trench should be as small as possible in order to limit the quantity of $SiO_2$ on the surface that has to be removed after filling the trench. Therefore an high aspect ratio is required and so in this test it is necessary: to measure the thickness of the $SiO_2$ at the end of the trenches and to understand the minimum trench thickness allowing the required aspect ratio and enough conformality. It is also important to notice that the oxide must be deposited and cannot be obtained by oxidation due to the necessity to preserve the backside marks. Finally, as a last remark, it is necessary to check the clogging at the top of the trench, because, if it is above the surface of Silicon, another mask is required to preserve the $SiO_2$ barrier during the removal of the oxide over the surface.

### 4.2.1 Step in the test

Knowing the requirements presented above the test can be subdivided in four main steps visible in figure 4.2 :

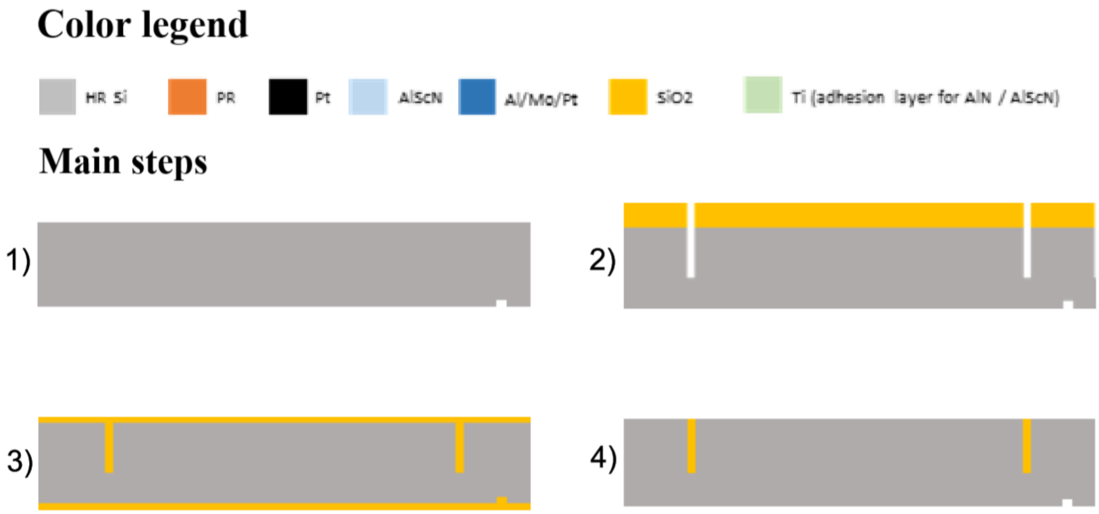


**Figure 4.2:** Main steps for the trench filling test

Here the explanation of each step and the respective substeps is presented:

1. Exposure, etching and photoresist strip to make the backside alignment marks.

2. Deposition of $1.5\mu m$ of sputtered $SiO_2$ as an hard mask to withstand the deep reactive ion etching (DRIE) process for the definition of the relase area. Exposure of the trench mask (in the test it has been done with UV laser writing), etching of the hard mask and finally realization of the high aspect ratio trenches with DRIE.

3. Hard mask strip and RCA cleaning before sending the wafer into the furnace where the $2\mu m$ of $SiO_2$ has been deposited exploiting the TEOS ( Tetra Ethyl Ortho Silicate) as a gas for the reaction.

4. Exposure with the ASML PAS 5500/350C DUV stepper to verify the correct alignment even with $2\mu m$ on the backside and oxide removal with BHF.

5. Cleaving of the sample and analysis at the Scanning electron microscope (SEM).

To perform the test, in order to analyze different aspect ratios and if there are any differences regarding the height at which the trenches become clogged, an apposite layout, presenting different trench thickness grouped in lines of ten, has been developed and can be observed in figure 4.3.

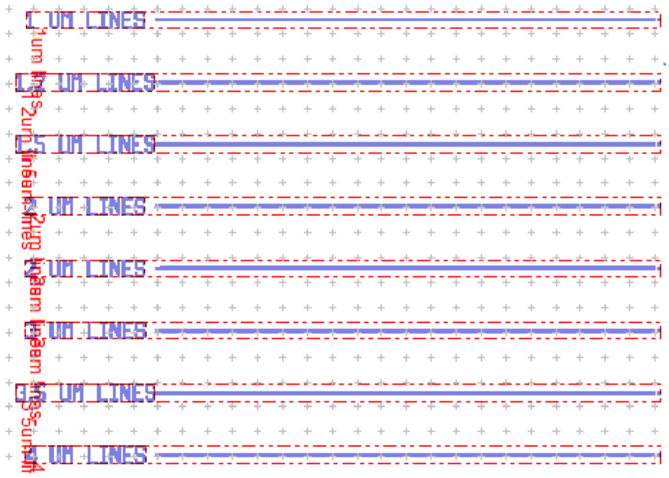


**Figure 4.3:** Test layout for the trench filling test (positive polarity).

It is important to notice that the trench designed in this layout have been drawn with the length of several centimeters in order to be visible without the requirement of a microscope to ease the cleaving process.

### 4.2.2 SEM analysis of the sample

To properly analyze the filling of the trenches without the risk of etching also inside of them (the BHF recipe still has to be finely defined) the wafer has been cut in the step 4) just after the misalignment test before the removal of the oxide. To start the analysis the trenches of the smallest size have been observed (figure 4.4). From a first glance, the conformality obtained through the TEOS in the furnace seems to be extremely good. In fact, even considering the smallest possible apertures the oxide is present also at the bottom of the holes. Another important observation is related to the global depth of the trenches, whose value is 48 *umm* instead of the 60$\mu m$ expected. This result make sense since the effectiveness of the DRIE decreases significantly with high aspect ratio, and so, to get deeper trenches a longer process is required. Considering the obtained value of 48$\mu m$, it is already sufficient to obtain the wanted barrier layer, in fact, a small over etch under the trenches will not affect the metal pads or the structures surrounding the device. Hence, in the following images, the attention has been put on this set of trenches since they allow to deposit less oxide reducing so the overall cost of fabrication and the time that will be required to remove the oxide above the silicon substrate.

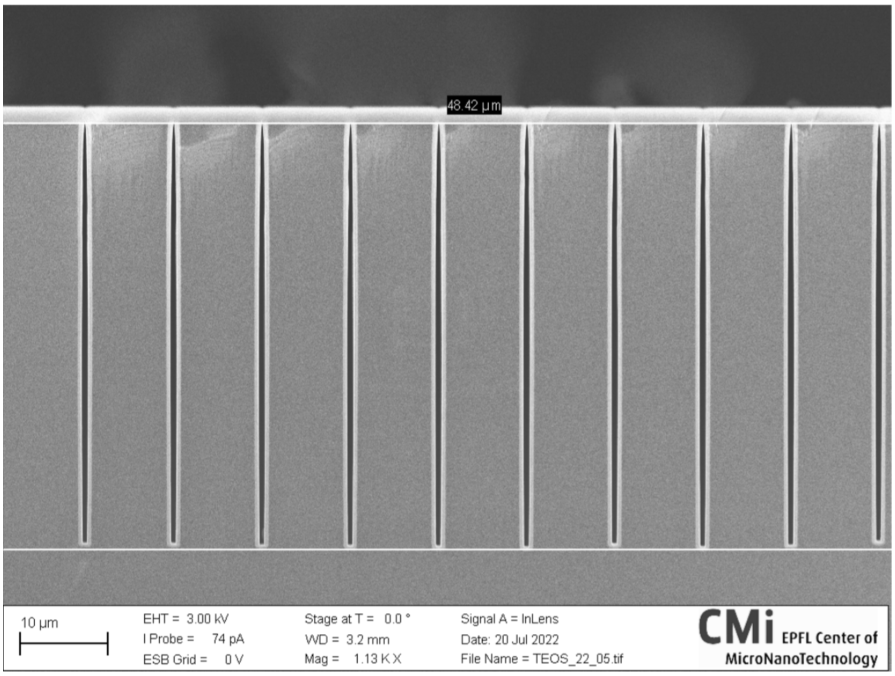


**Figure 4.4:** SEM image of the group of the smallest test cells

To verify the previous considerations a zoom on the bottom part of one of the smallest trenches have been performed:

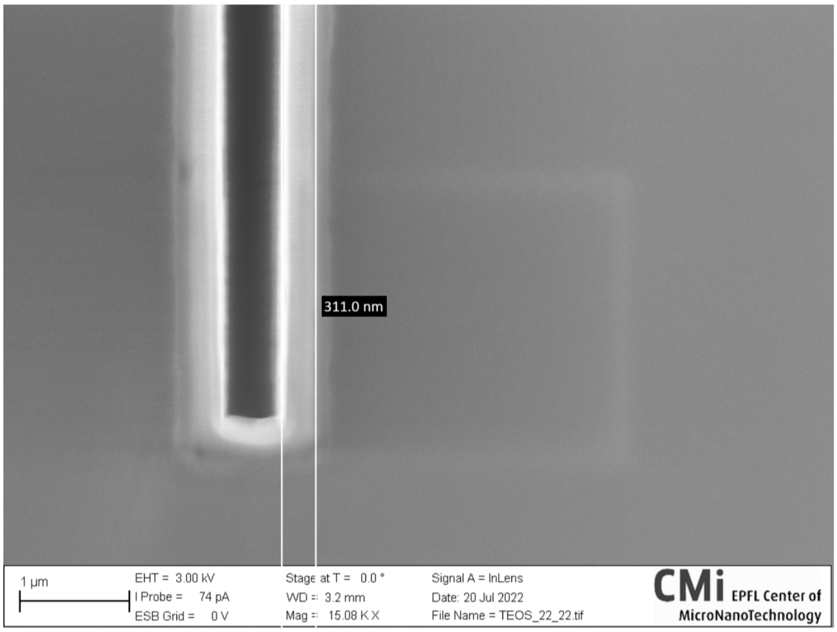


**Figure 4.5:** SEM image of the bottom part of one the smallest cells.

As it is possible to see the from the figure 4.5, the thickness of the oxide is still sufficient to constitute a good barrier also at the bottom of the trench, therefore the deposition of Silicon oxide with TEOS can be inserted in the process flow without remarks. At this point, to obtain the missing information, a zoom have been performed on the top of the same trench of figure 4.5:

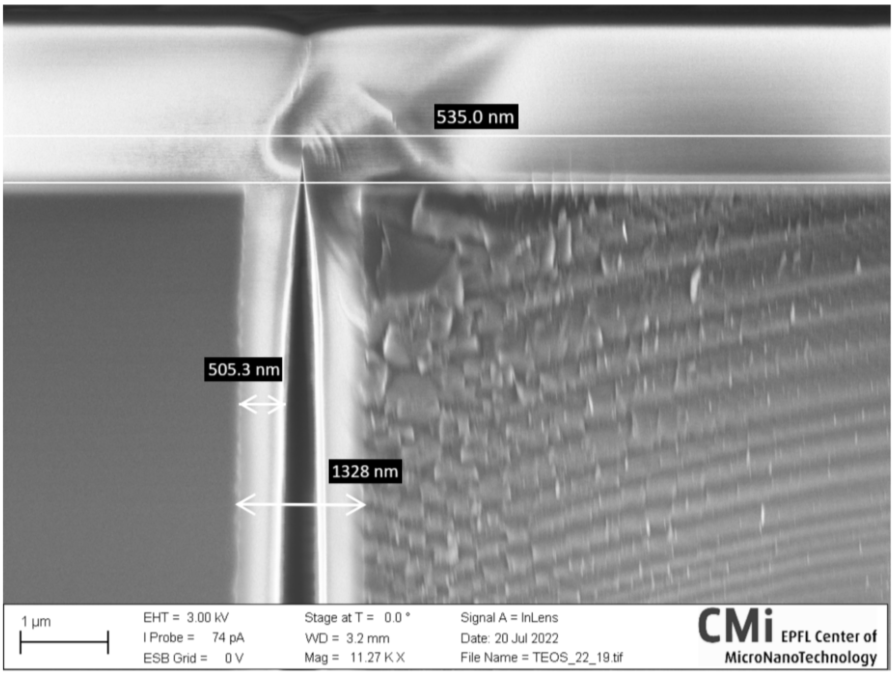


**Figure 4.6:** SEM image of the higher part of one the smallest cells.

As it is possible to see from the image 4.6, having a value of $1.3\mu m$ instead of $1\mu m$, the real dimension of the hole is bigger than expected. This different result is related to the resolution limit of the tool used for the test (UV laser writing with Heidelberg MLA150) and will not happen in the real process with the DUV stepper. Moreover the size change does not affect the validity of the result since it will just require few time more in the furnace. Concerning the other measurements, the thickness of the barrier layer is, as expected, higher than the one at the bottom and so, it is sufficient for the devoted purpose. The only problem highlighted in this image is represented by the fact that the two $SiO2$ walls come into contact at a significant height (400-500 nm) above the surface of the silicon substrate. This means that, during the removal of the oxide on the surface, the acid can flow inside the trench removing the silicon oxide and making the barrier layer ineffective. To solve this issues, it is necessary to modify the process flow as shown in figure 4.7. Starting from the step 1) the trenches are completely filled, at this point the silicon oxide has to be partially removed without exposing the aperture of the trenches by finely timing the BHF etching time. Then, as illustrated in step 2), an additional lithographic step is required in order to exploit the photoresist as a protecting layer for the holes. Finally in step 3) the $SiO_2$ is completely removed exploiting BHF and the resist is stripped. It is important to notice that the silicon oxide is thinned before the lithographic process in order to reduce the difference in height between the silicon surface and the Silicon oxide one. This process is recommended to avoid a reduction of the AlScN quality that will be deposited in the following steps.

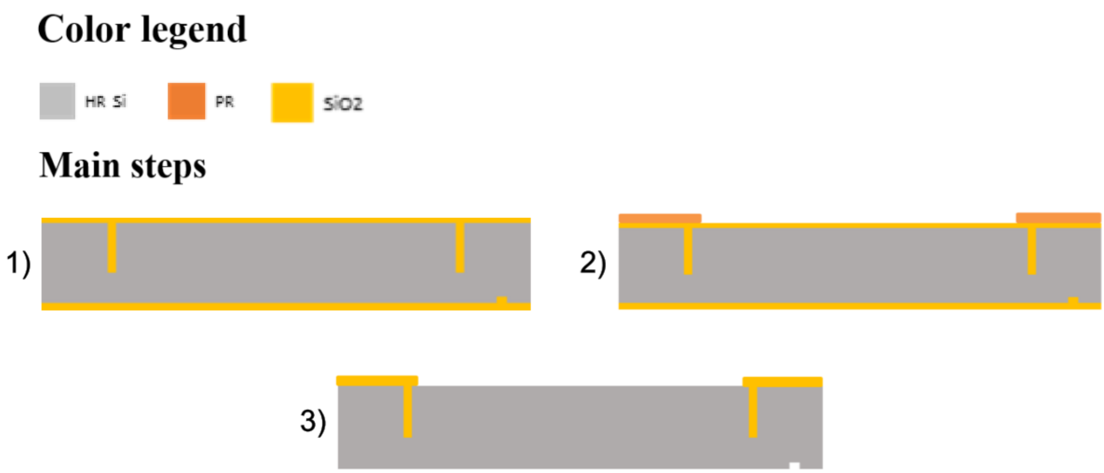


**Figure 4.7:** Modification of the steps to solve the clogging issue.

Having verified the effectiveness of the process and after solving the clogging problem, the process flow is now ready for the layout development and fabrication.

## 4.3 AlScN IBE etch test

The steps 6) and 7) of figure 4.1 currently exploit a well established plasma etching recipe on the STS Multiplex ICP tool to perform the etching of the $Al_{0.6}Sc_{0.4}N$ employed for the piezoelectric element. However in this case, due to the high percentage of scandium which is a considerably heavy metal, the etch rate is quite slow and an hard mask is required to withstand the whole process. For this reason some other solutions are currently under evaluation. Among these the ion beam etching (IBE) seems to be a promising solution to etch the AlScN. In fact, as stated in [35] (even if with lower percentage of scandium) the physical etching performed with IBE showed a good selectivity between AlScN and PR (0.5) and good results in terms of sidewalls angle (71-79 degrees). Both those result are promising for the purpose of this project since, a good selectivity might allow to perform the etching without introducing the hard mask whereas high angle sidewalls reduces the generation of spurious modes associated to the edges of the device.

### 4.3.1 Test description and results

The etching of AlScN involve the separation of the piezoelectric material on the resonator with the one which lie on the substrate. Hence the mask needed for the test requires the presence of big apertures. At the same time, since some smaller features might be added to the layout, the presence of smaller apertures can be useful. For this purpose it has been used the reticle developed during previous semester project visible in figure 4.8:

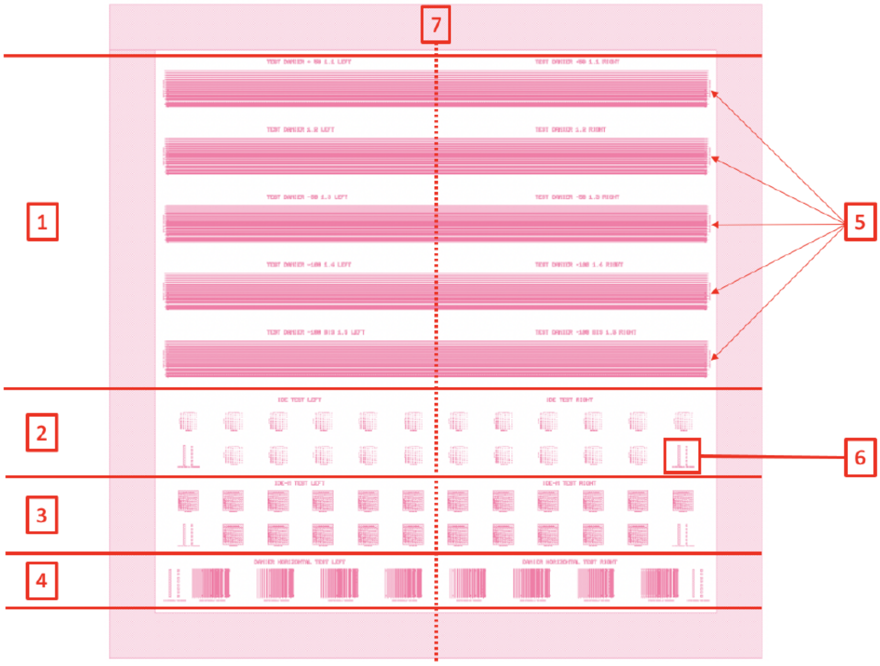


**Figure 4.8:** Reticle chip for IBE etch test.[26]

Here in the portion [1] of the reticle present many group of trenches ranging from a size of $5\mu m$ (big apertures) down to $150nm$ (small apertures) that, having a length in the centimeter scale, are easy to be detected and cleaved allowing to perform an accurate measurement. So, to start the test, an high resistive silicon wafer with 500nm of AlScN has been exposed. The DUV stepper has been used in order to exploit the M35G resist which, being $1.2\mu m$ thick and having showed a considerably high resistance respect to physical etching in some previous results, represent the suitable candidate for the purpose of the test. After the lithographic step the wafer has been cleaved to get four samples. Then each of these pieces has been attached to a silicon dummy wafer through quick stick (with particular attention to maintain a good thermal conductivity) and inserted in the Veeco Nexus IBE350 chamber. Here the wafer angle has been set to -10 degrees in order to avoid the redeposition of atoms after the etching. As a first trial a medium power etching (the voltage value are previously defined in the machine and cannot be modified) has been performed for 620 seconds. Then the wafer has been cleaved and analyzed at the SEM:

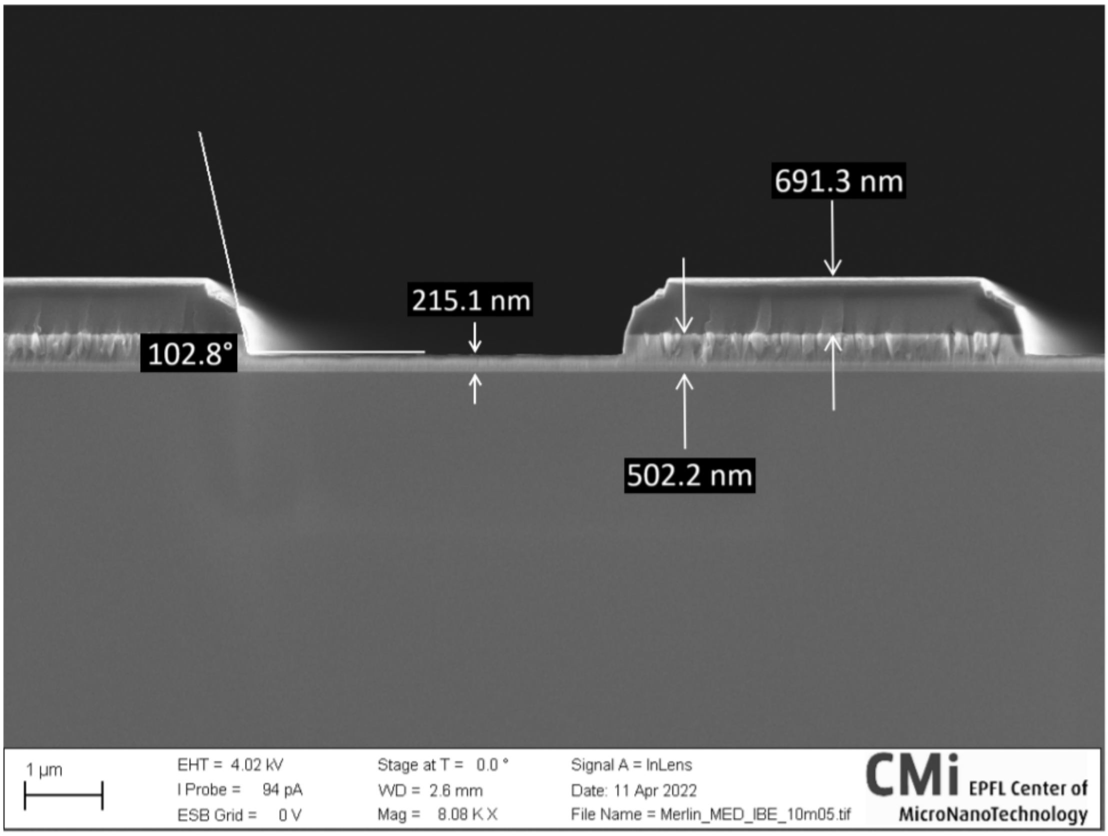


**Figure 4.9:** SEM image of the $5\mu m$ apertures after 620s of medium power IBE.

Observing the image and knowing that the initial thickness of the M35G resist is around $1.2\mu m$ it is possible to compute the remaining process time to complete the AlScN etching and how much time the photoresist is going to protect the the underlying material. The result calculated are around 18.40s to complete the etching and 24 minutes before consuming the resist. Concerning the sidewalls, the angle measured is 78 degrees which correspond to an extremely good result. To obtain further information also the $1\mu m$ trenches have been analyzed in figure 4.10. Here it is possible to see that sidewalls angle are similar, but the etch rate of AlScN is strongly reduced. This might be related to the fact that the scandium, being heavier than the other components, is partially redeposited in presence of small apertures. The consequence of this fact is that the IBE cannot be exploited to perform etching of small features.

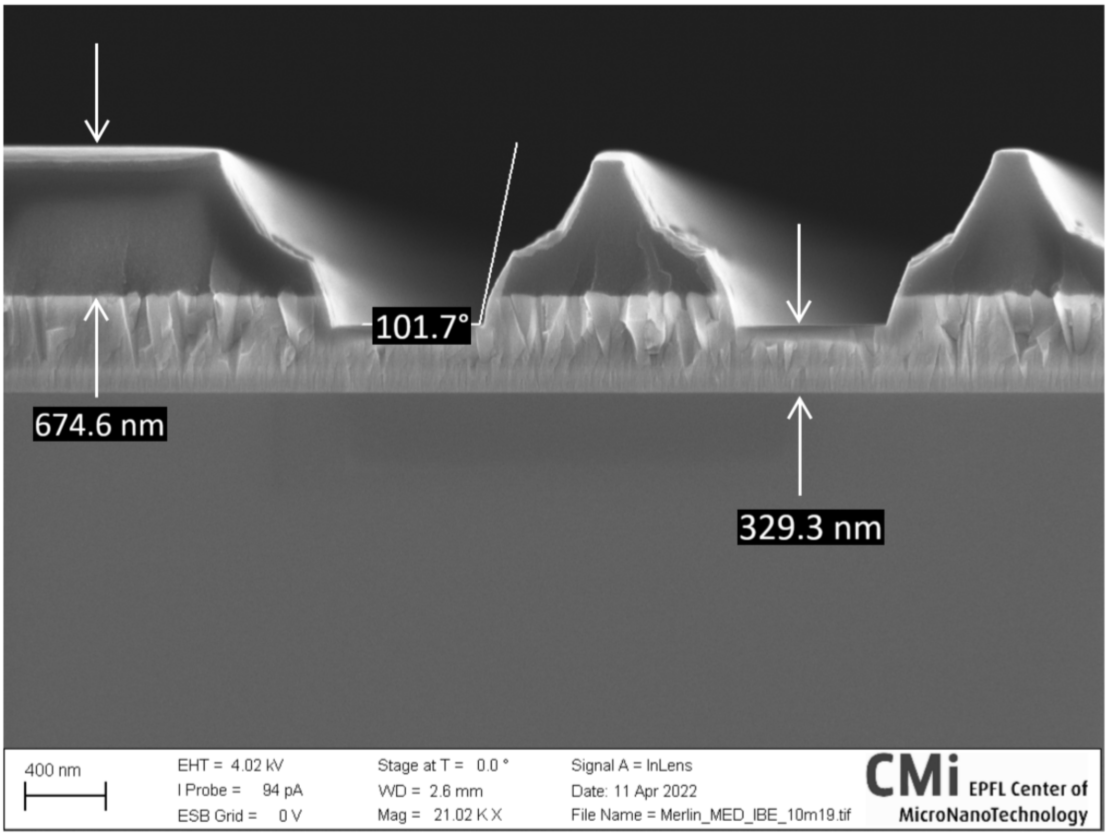


**Figure 4.10:** SEM image of the $1\mu m$ apertures after 620s of medium power IBE.

Another interesting fact is that, decreasing the space between the trenches, the resist assume a triangular shape and, over a certain limit, his height will be abruptly decreased. However, due to the design of the resonator, this fact is not relevant and the reference result is constituted by the trenches on the sides. So, what it is important to notice and is visible also in figure 4.9, is that the thickness of the resist decreases in correspondence of the trenches edges, therefore the actual etching time before the reducing the sidewalls angle is probably significantly lower than the 24 minutes previously computed. This means that an analysis with the appropriate time to etch the whole AlScN is required. To do that another sample has been processed for 18 minutes at -10 degrees with medium power obtaining:

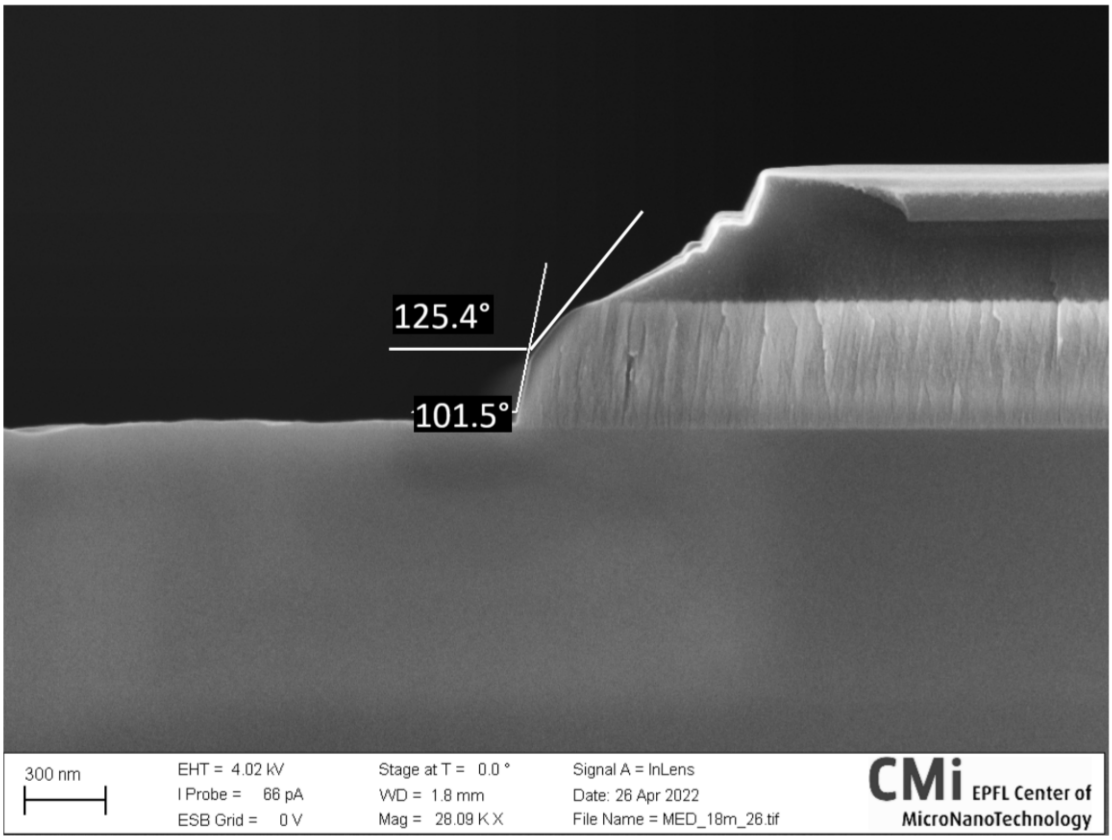


**Figure 4.11:** SEM image of the $5\mu m$ apertures after 18 minutes of medium power IBE.

From this image it is possible to verify that, as predicted a thin layer of AlScN still has to be etched, but more interesting, is the fact that the photoresist has been completely consumed at the edges of the trenches leading to a worsening of the sidewalls angle (from 80 to 55 degrees). This means that the IBE solution is not applicable without the employment of an hard mask with the actual thickness of 500nm of piezoelectric material even considering wide apertures. However it might be an interesting solution in case of thinner layer.

### 4.3.2 IBE etching with hard mask

After the previous IBE test it is possible to deduce that this kind of process is not suitable for etching small features because of the redeposition, however, before that the resist is consumed on the edges, it exhibit very interesting results in terms of sidewalls angle representing so high potentiality for the separation of the resonator respect to the rest of the substrate. Hence, since the hard mask is necessary also with the already defined process, it is worth to observe the result with the hard mask addition and to test its resistance with respect to ion etching. Hence, a $1\mu m$ $SiO_2$ hard mask has been deposited on a silicon wafer, exposed with the design of the previous cell and etched through the SPTS Advanced Plasma System obtaining almost vertical sidewalls angle (89 degrees). Then keeping the M35G resist over the mask to give a further protection, the silicon substrate was etched with the recipe of the previous tests for 20 minutes.

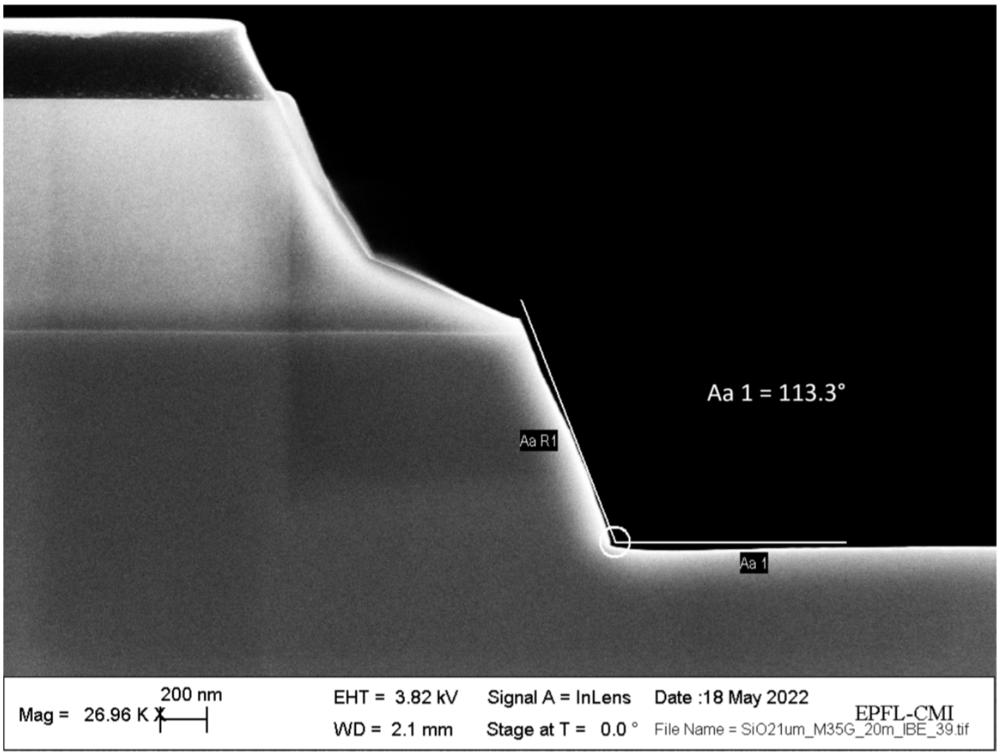


**Figure 4.12:** SEM image of the $5\mu m$ apertures after 20 minutes of medium power IBE on silicon with Hard mask protection.

As it is possible to see observing the image, the hard mask is almost totally etched but it managed to protect the material below proving that $1\mu m$ of $SiO_2$ thickness is enough to withstand the process. Concerning the sidewalls angle, the result seems to be worse than the one previously obtained (67 instead 79 degrees), moreover there is still a little bit worse angle on the top of the wall. However this test has been done etching silicon instead of AlScN and so the results might be slightly altered. Therefore we can conclude saying that the use of the ion beam etching with $500nm$ of piezoelectric thickness does not lead to extremely big improvement since it still requires the use of an hard mask. However, promising results have been obtained considering the side-walls angle in the AlScN etching.

Hence, having found the required thickness for the hard mask and being the IBE a process which does not require changes in the process flow, this etching technique will be probably tested on some samples during the device fabrication.

# Chapter 5

# Layout development and reticle fabrication

The final step of this project is devoted to the design of the final layout for a new generation of high frequency resonators for filtering applications and to the writing of a reticle for the DUV stepper. Hence, in this section the information coming from the simulation sections and from the fabrication chapter will be grouped, to take into account all the possible issues.

## 5.1 Device cell & device choices

To start the layout it is important to clarify layer by layer which are the necessary masks that have to be built in the layout. In figure 5.1 are presented the five mask needed(the alignment marks mask is provided by the CMi staff):

1. Definition of the trenches for the release area confinement

2. Trenches protection layer

3. Definition of the platinum bottom plate

4. Top metal layer patterning

5. Resonator openings definition

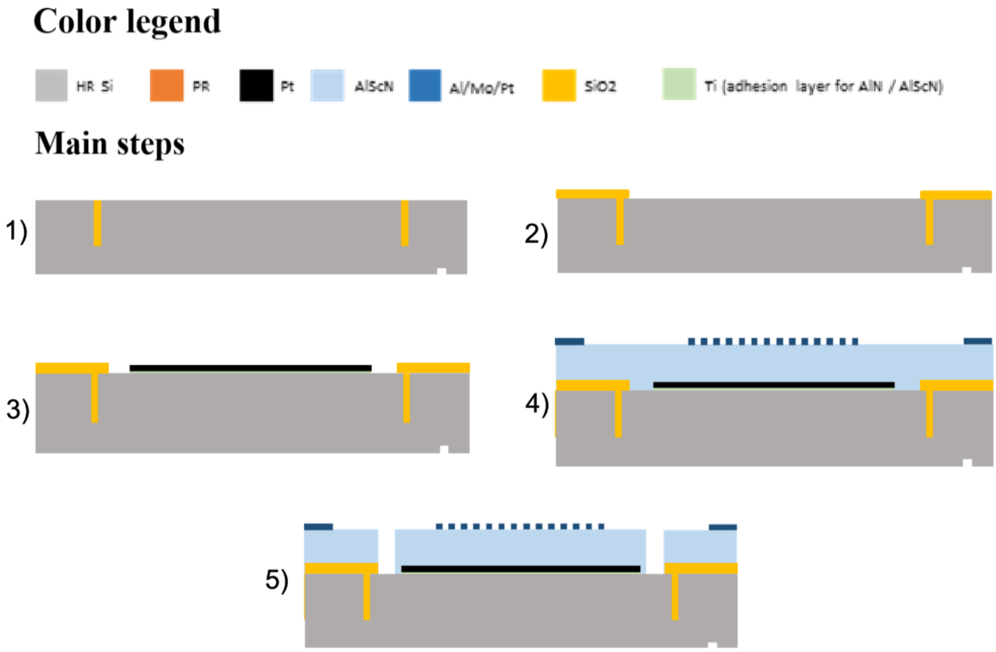


**Figure 5.1:** Lithographic steps required in the reticle.

Starting from this picture, exploiting the software L-edit the resonator cell has been built. Here as an example the cell for the n28 band is shown:

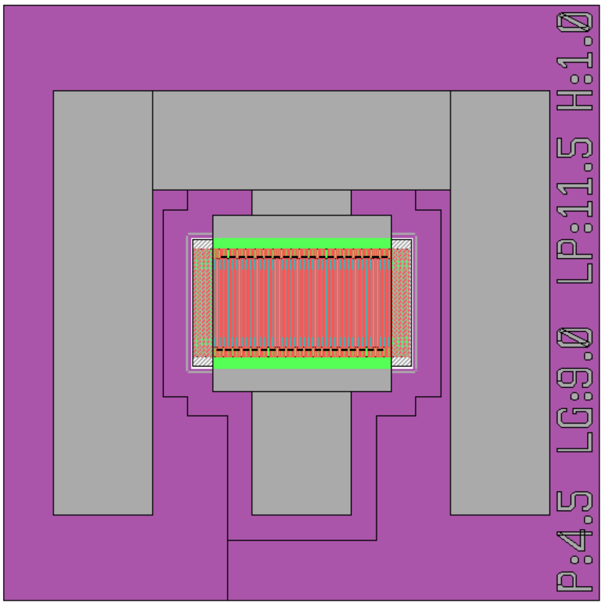


**Figure 5.2:** Example of a n28 band cell layout

To better understand and explain the the various choices the layers can be separated in the various masks:

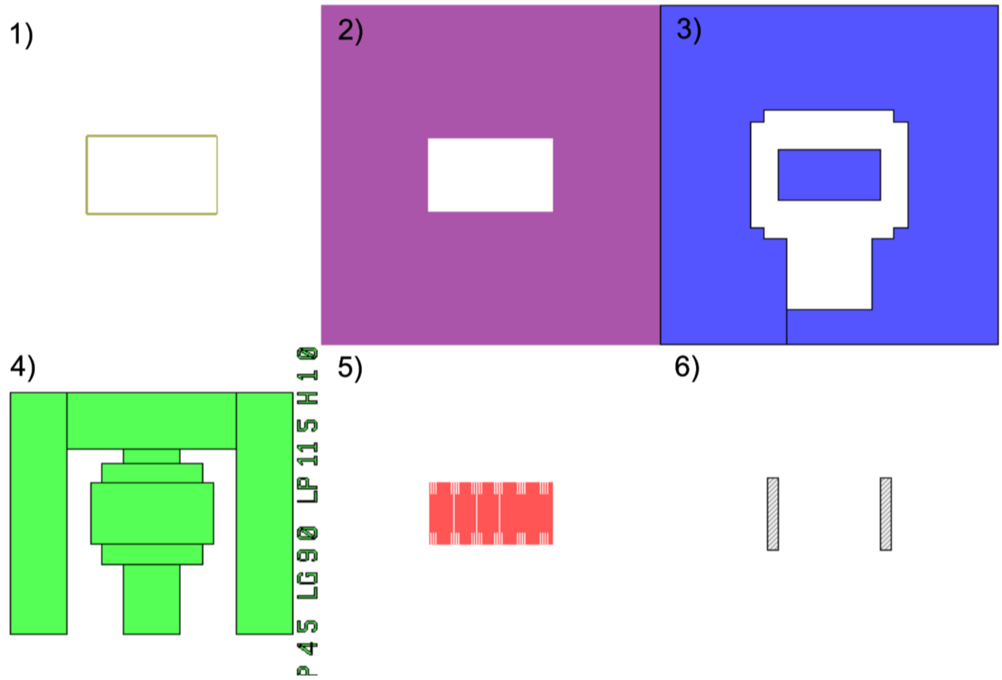


**Figure 5.3:** N28 band cell layout with separate layers.

It is important to highlight that the layers 2), 3) and 4) are built in the opposite polarity (negative) respect to the others (positive) to better visualize the device in the layout but, before writing the mask, all the layers will be set to positive polarity case. If the layers 1) is exactly as expected it is possible to make some observation concerning the other ones. Layer 2 only exposes the center of the picture instead of protecting just the trench in order to avoid the presence of two mismatch in terms of height that could decrease the quality of the piezoelectric layer. For a similar reason the mask 3) allow to remove the platinum only around the resonator, in fact, the presence of platinum, improve the growth of AlScN. Concerning the top metal layer it has been split in two different masks. This choice has been done since the top metal layer presents a big difference in terms of size between metal pads for probing of layer 4)(green) and metal fingers of layer 5) (red). Hence, the mismatch of required dose during the stepper exposure could have led to significant errors in the images on the wafers. Concerning the orientation of the cell it has been rotated by 90 degrees since, having a reticle writing tool (VPG200 from Heidelberg) which perform direct laser writing by making movements in the vertical direction it exhibit better resolution for vertical features. Therefore, being the critical dimension represented by the fingers, they have been put in the vertical

direction.
Regarding the design, the various parameters have been kept accordingly to the consideration already done in the 3D simulation chapter. The only differences are related to the number of fingers, since in the real case it is not possible to deal with a periodic cell anymore, and to the presence of the anchors. Hence, to define the correct number of fingers, considering that the device is oriented to filtering applications, the resonator need to be matched with the rest of the circuitry. To do that, a 2D periodic simulation for a single cell has been performed and the value of the admittance in the background regions (far from spurious and resonance peaks) has been taken. From this number it is possible to compute the impedance of a single cell and so, since adding more cells correspond to put in parallel more resistances, the correct number to obtain 50Ω, which is the reference value, can be computed. However, since the aim of this project is to develop a new generation device that will not be inserted with other components, the target impedance chosen is 200Ω to ease the characterization phase. Concerning the anchors, to understand their shape it is interesting to visualize the layout top metal, release area confinement and openings holes:

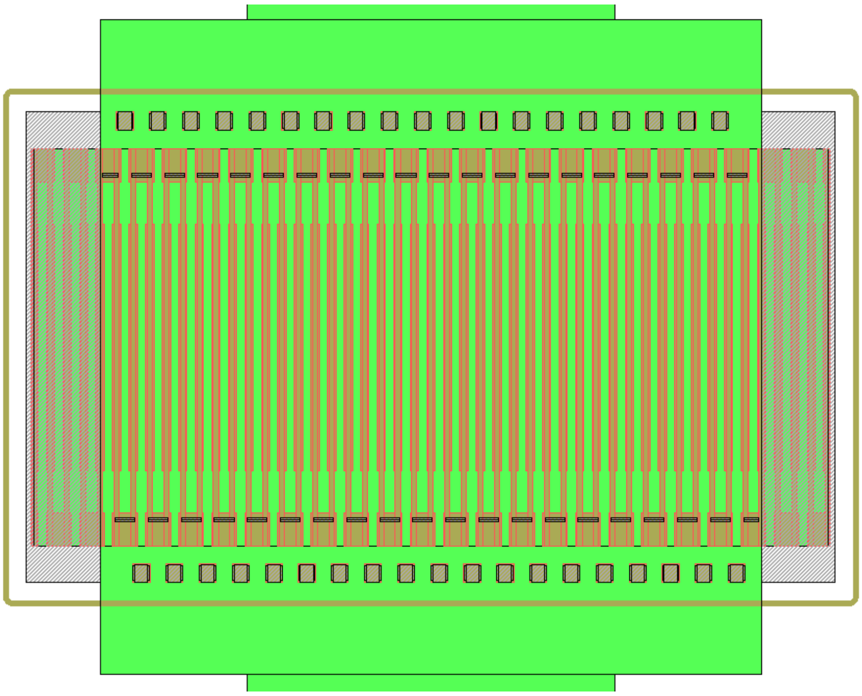

**Figure 5.4:** Zoom on a n28 band device with layers 1), 4), 5), 6) of figure 5.3.

As it is possible to see from the figure, the anchors have the same width of the bus (they are separated only by the release area confinement) which coincides with the one of the resonator. This solution is interesting since it allow to maintain the same anchor regardless the width of the resonator, however an accurate analysis about the associated losses on the substrate still has to be performed. Moreover, as it is possible to see observing the openings layer (grey), this solution imply less space to allow the entrance of xenon difluoride for the release of the structure. For this reason some holes have been placed in the bus to ease this process. It is interesting to highlight that the holes in the bus have been placed in a periodic way in front of the fingers in order to obtain a periodic structure which can be easily simulated. The last observation which can be made from the figure 5.4 is related to the fact that the fingers are larger than the resonator. In fact, four additional fingers, that will be eventually removed during the etching process, have been added to each side of the devices ensuring to have the correct number of fingers in case of misalignment and to guarantee the same illumination conditions. Otherwise, without these "dummy" fingers, the more external electrodes would have required different exposure dose in the DUV stepper being isolated lines and not part of a pattern.

## 5.2 Layout cells

In this section will be presented the main features cells which have been represented on the reticle

### 5.2.1 Primary cell

The primary cell is the one which contains the resonators. In this first reticle the focus has been set on two different objective: find the optimal configuration for the design and scale up, as much as possible, in frequency. To achieve the first goal the n28 band device has been selected since, being at a relatively low frequency, it is easier to be fabricated. Hence in this case many different devices have been placed in the layout varying gap, piston size and dimension of the holes in the gap trying to exploit all the solutions presented in the 3D simulations chapter. Moreover, to evaluate the possible design differences correlated to the pitch size and the dimension of the resonator, a similar parameter sweep have been done for a pitch size of $1\mu m$. Concerning the second objective, which consists in scaling up the frequency of the devices reducing the pitch, a simpler design without pistons and holes in the gap has been drawn. In this case the parameter modified in the various devices, besides the gap, is the length of the active area to verify if, increasing the length of the fingers, the electric resistance can constitute the bottleneck of the resonator's quality factor. Regarding the pitch size, a big pitch sweep have been performed ranging from $P = 4\mu m$ to $P = 500nm$. Hence, having applied an electric coverage value of 50%, the critical dimension of the features is $250nm$. It is important to notice that the real potentiality of the DUV stepper is $150nm$ of resolution, however it has been decided to keep a certain margin due to the fact that the reticle it has not be ordered but produced in house. Another important consideration is related to the mask 5) of image 5.3, in fact, by sweeping the pitch from $4.5\mu m$ to $500nm$ there is a very big variability in terms of size and optimal dose, that, in case of critical features such as the fingers, can induce significant problems in the design. Therefore, to solve this issue, the primary cell has been split in two different cells separated at reticle level by 4mm (space required by the stepper between two different designs) in such a way that, only for the mask 5), the pitch ranging from $1\mu m$ to $500nm$ will be exposed with a different dose ensuring a good result.

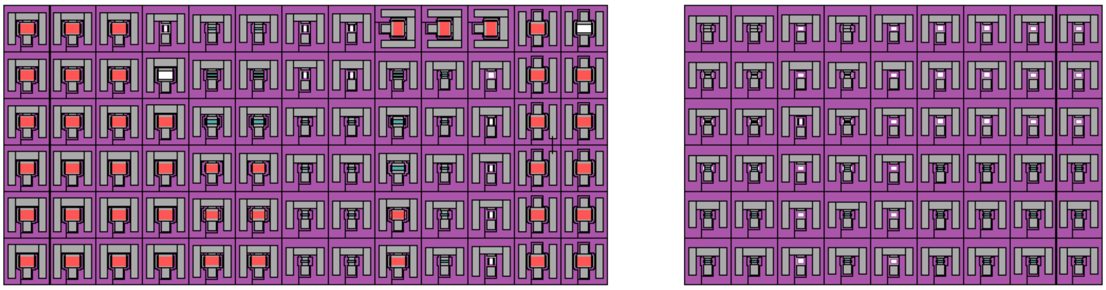

**Figure 5.5:** Primary cell with "big" pitches on the left and "small" ones on the right. Note that each colour correspond to a different image on the reticle.

## 5.2.2 Test cell

To complete the layout a test cell have been inserted (figure 5.6). This cell can be repeated few times in the wafer and can be useful to perform some fast check. Starting from the simpler things, some apertures have been inserted to test the effectiveness of the AlScN etching and some lines are present to check the fingers result. However the most important part is represented by the VSPM (alignment marks) and the vernier symbols. The VSPM, which have been added for each layer, constitute a backup alignment method that exploit an additional off axis detection system called ATHENA (an higher resolution image cannot be inserted since it is a confidential ASML material). The Vernier marks are based on a hair comb structure containing both for horizontal and vertical direction two aligned lines with some others progressively mismatched. Hence, by observing which lines are perfectly centered, they allow to measure the misalignment with a 100nm precision. For this reason they have been put for each combination of layer and constitute an efficient method to quickly verify the misalignment after each exposure.

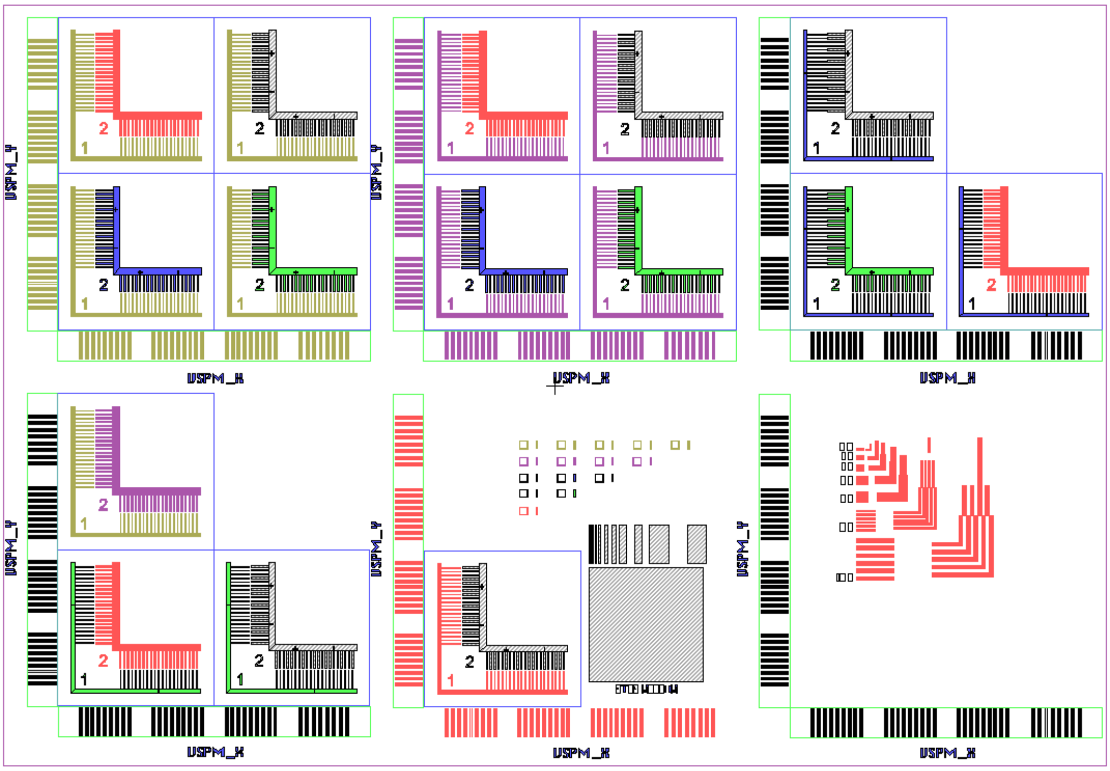

**Figure 5.6:** Test cell representation. Note that each colour correspond to a different image on the reticle.

### 5.2.3 Final layout

Inserting together all the feature previously presented the obtained result is showed in figure 5.7 (some other features are present but are not related to this project and so they will not be explained). As it is possible to observe, to have enough space, the primary cells have been distributed in the vertical direction, however this choice might lead to some lost of cells in correspondence of the external part of the wafer due to the very different angle of exposure for the various layers. The actual solution to solve this problem in industry application is to build a reticle for each layer, but being this method too expensive, to mitigate this problem, it is sufficient to put the mask with critical features (fingers and resonator openings) in the center of the reticle. Moreover, also in case of some primary cell lost, thanks to the effort in miniaturizing the cells, a high number of cell will still be available allowing to perform affordable measurement.

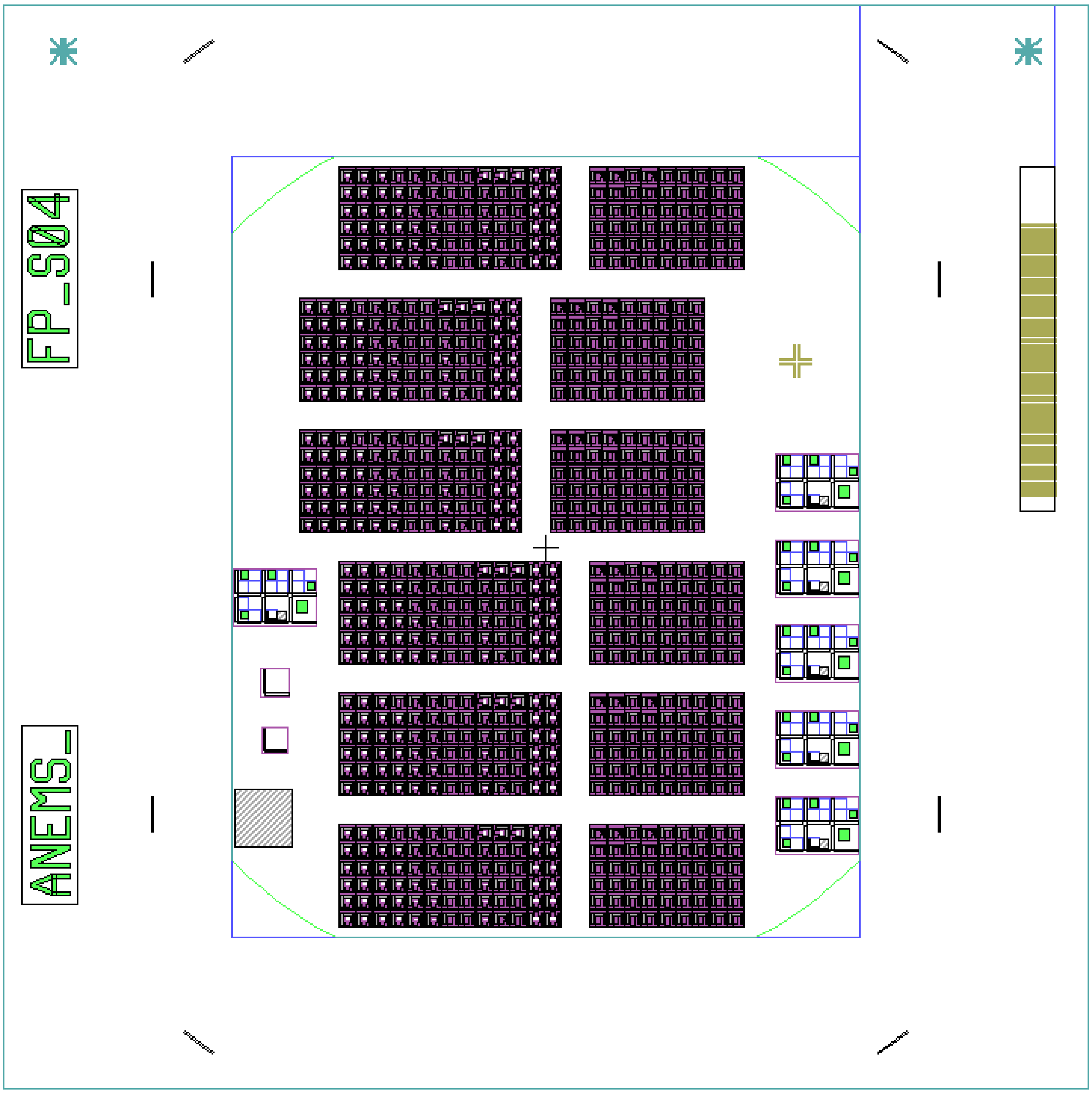


**Figure 5.7:** Final image of the layout. Note that here the layers have not been separated due to L-edit representation issue

Starting from the figure 5.7, after isolating each layer and putting everything in positive polarity, the reticle is ready for the fabrication.

## 5.3 Reticle fabrication

Having completed the definition of the layout it has been decided to fabricate the reticle without ordering it from specialized reticle manufacturer. This choice has been done because, beyond the gained knowledge, the in-house fabrication allow a faster and cheaper realization of the feature representing, in the prototyping phase, a great advantage. However, it is important to notice that, in the final stage of the project or in the case where a extremely high resolution is needed, a mask shop could represent the best solution. The utilized fabrication process is presented in the following figure 5.8:

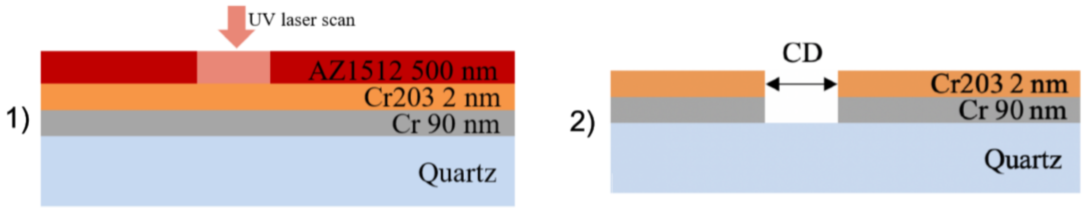


**Figure 5.8:** Process for reticle fabrication.[26]

In step 1) a Maskless lithography (MPL) is performed through a UV laser scan whereas, the second step consist in Chromium etching and resist stripping. The tool used for the first step is the Heidelberg Instruments VPG200 which perform MLP exploiting its UV laser beam with a 355(nm) wavelength and offers three different writing head with 20,10 and 4mm sizes. It is important to notice that this tool allow to write pattern with critical dimension $> 600nm$, but, being the features at reticle level four times bigger than the one on the wafer, the critical feature of 250nm can be still written. However, being $1\mu m$ not that far from the critical dimension, the 4mm write head has been chosen to get an higher resolution at the cost of a lower throughput. Regarding the development and stripping step, which represent a critical step since the critical dimension are approached and the Chromium etching is performed through an isotropic wet recipe, the employed tool is the Hamatech mask processor which complete both steps in a single process. A final important remark for mask and reticle fabrication is represented by the necessity of mirror the layout before writing the images since the Chromium will be face-up during the writing step and face-down when inserted in the DUV stepper.

### 5.3.1 Mask test

The Heidelberg VPG 200 is a tool heavily used in the cleanroom and so is calibrated every week, however this calibration need to cover a big variety of application. This means that the reference parameters provided might not be the optimal ones for the critical dimension of the considered layout, therefore a dose test is strongly suggested before proceeding. Since a blank reticle is expensive due to the presence of quartz, it is cheaper and equally affordable to perform this analysis by exploiting a common mask and writing it with the same exposure parameters. Hence a blank mask has been ordered, the 4mm write head has been inserted in the VPG 200 and the reference parameters provided by the cleanroom staff have been inserted. Among these the critical ones are pneumatic defocus (DF) that is set to zero at the surface of the resist and is progressively shifted inside the resit moving to the Chromium surface, and the dose intensity of the laser with respect to the maximum available power expressed in percentage. Since varying one of these two parameters the optimal value of the other one change, the defocus has been set to the recommended value and the dose intensity have been swept between the values of 6.5 and 12 with a step of 0.5 (the recommended value was 9%). Then after Chromium development and stripping, the mask has been analyzed in the SEM by exploiting the mask holder (this is not a standard procedure since it requires to open the main chamber). Before starting the observation it is important to remark that the images at reticle level are four times bigger than the one designed for wafer level, hence all the previously mentioned values must be multiplied by four. The first feature observed are the fingers of the 500nm pitch device, since they represent the most critical feature present in the device:

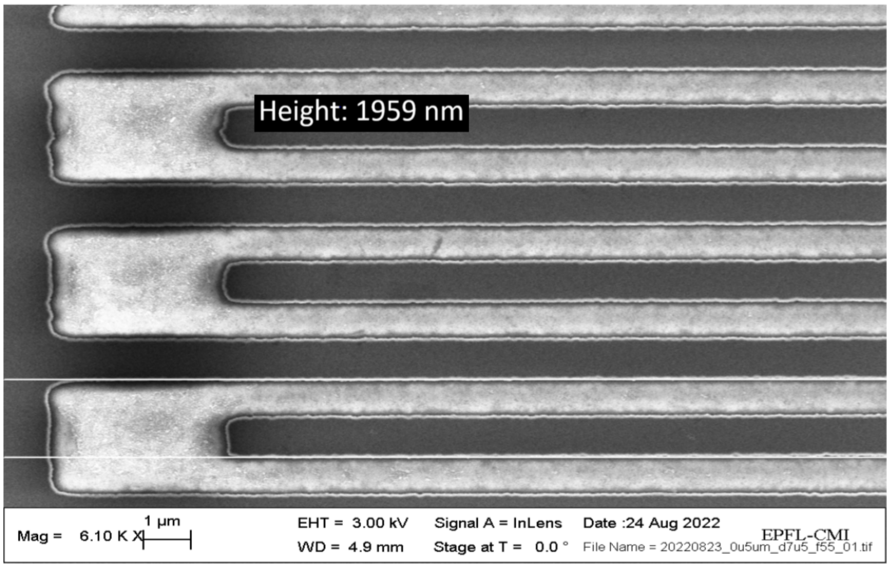


**Figure 5.9:** SEM image of fingers ($P = 500nm$) with optimal dose (7.5).

Observing the figure it is possible to see that the layout has been correctly reproduced, even if slight imprecision in the direction perpendicular respect to the fingers are present. This is related to the fact that the VPG200 move the laser only in one direction (parallel to the fingers) and is a bit imprecise in the perpendicular one, but, in this case, the error is small enough to be tolerable. Regarding the doses, many have been observed and, as a result, the one closer to the ideal case of 50% of coverage is 7.5. Another critical structure is represented by the holes in the gap because, despite being bigger than the fingers they are in the opposite direction:

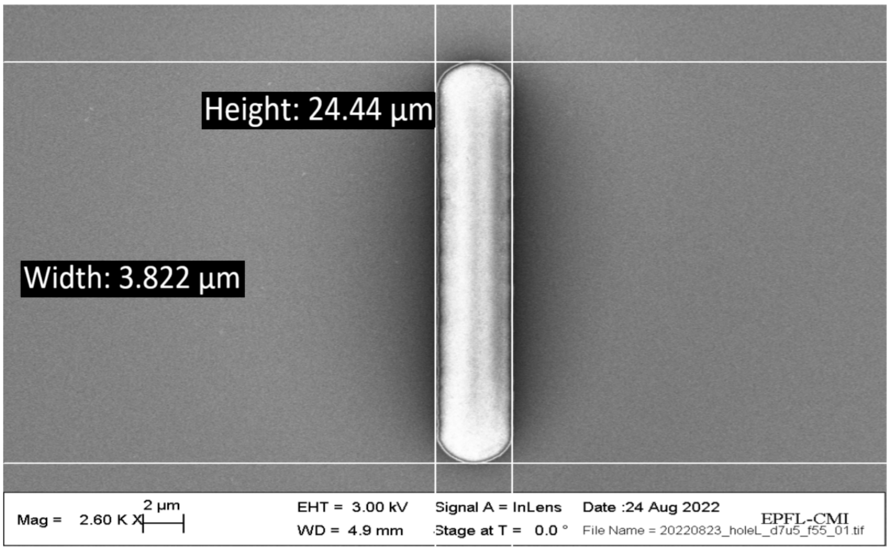


**Figure 5.10:** SEM image of gap hole in the openings layer (dose 7.5).

As it is possible to see, also in this case the design and the result are close to the one expected ($width = 3.822\mu m$ and $Height = 25.4\mu m$). A further investigation is required for the release area confinement trenches due to their relatively small size and centrality in the device fabrication:

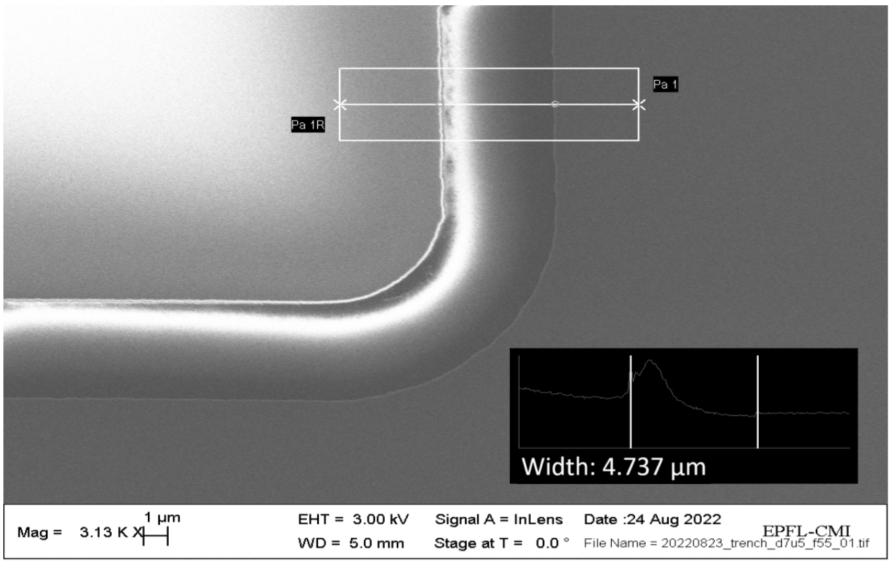


**Figure 5.11:** SEM image of the release area confinement (Dose=7.5).

Also in this case the dose of 7.5 seems to be the optimal one being almost coincident to the layout value of $1.2\mu m$ at wafer level. As a final evaluation the fingers with pistons have been observed considering two device with $P = 4.5\mu m$ and $P = 1\mu m$:

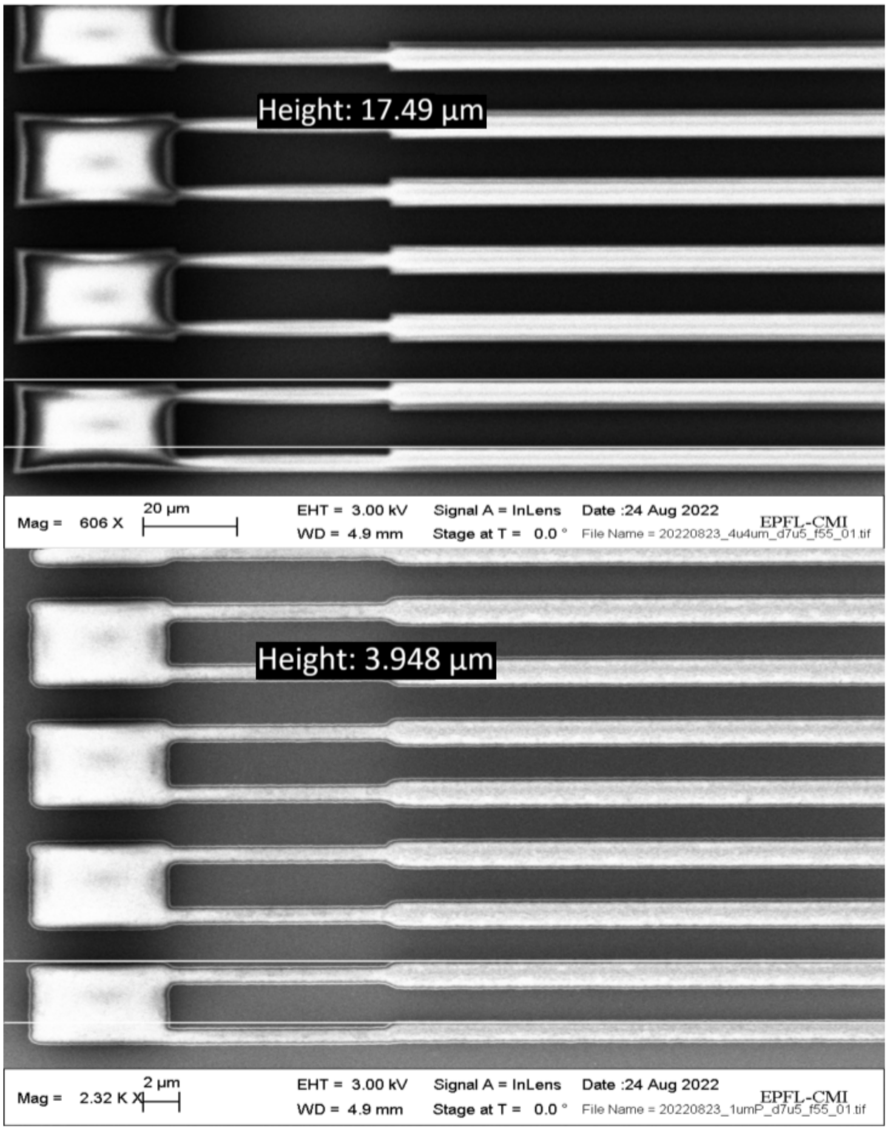


**Figure 5.12:** SEM image of fingers with pistons (Dose=7.5) having $P = 4.5\mu m$ (top) and $P = 1\mu m$ (bottom).

From figure 5.12 it is possible to observe that in both images the fingers have been represented with a good accuracy and that the pitch values are close to the ones expected. Comparing the pistons in top and bottom images a remarkable

difference is presence since, as expected, reducing the size of the features (bottom) their shape become rounded. However this fact should not affect their effect in the spurious elimination since their role is to change the phase velocity in the external area of the active region and so, a slight change of shape can be considered as a negligible aspect.
Considering all these images the result obtained with dose=7.5 are quite good, therefore it is possible to proceed with the writing of the reticle. It is important to notice that perfect results will never be obtained due to the size differences of the features and, for this reason, the reference dose have been set optimizing the smallest features, whose variations are more critical.

### 5.3.2 Final result

To write the reticle the same procedure utilized for the mask has been repeated with the only modification constituted by the insertion of the obtained intensity dose, the use of the 6 inch older for reticle and the pneumatic edge detection to manage the higher thickness of the reticle. The final is presented in figure 5.13:

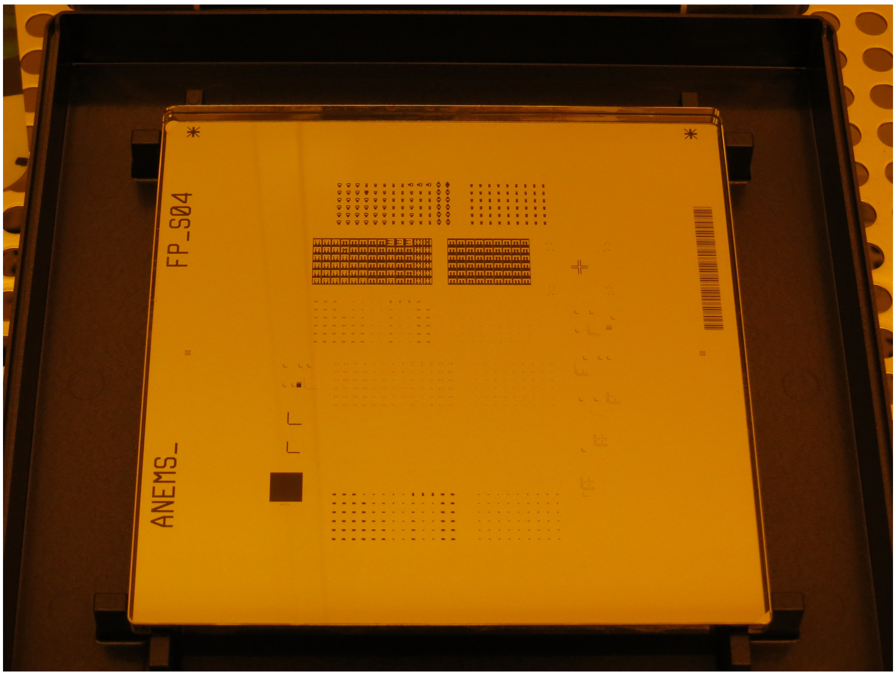


**Figure 5.13:** Image of the Fabricated reticle.

After verifying that the reticle matches the layout the reticle has been inserted in the ASML PAS 5500/350C DUV stepper and it is now employed in the photolithographic steps of the fabrication.

# Chapter 6

# Conclusions

Starting from the preliminary phase of the project an overview on the piezoelectric RF MEMS market has been performed. From this analysis the main devices present on the market and their most important characteristics have been investigated. This research allowed to individuate FBAR as the main competitor with respect to the Contour mode resonator studied in this project. By comparing these two devices, the CMRs potentiality in multi-frequency applications has been highlighted, however, at the same time two drawbacks have been found and regard: the fabrication complexity for UHF application and the lower electromechanical coupling. To solve the first issue, the employment of an advanced tool for batch production such as the ASML DUV stepper have been proposed, whereas to increase the $k_t^2$ a study on the AlScN as a piezoelectric element has been performed in advance with respect to this project. Hence, the goal of this thesis was to develop a new generation of UHF CMRs fabricated through the stepper, with a particular focus on the design optimization for $k_t^2$ maximization and spurious modes elimination. Concerning the quality factor it has not been considered as a main target, but many considerations have been taken into account to avoid detrimental effect on the device. Hence, starting from the 2D simulations, the optimal configuration to match electrical and mechanical domain have been found. Then, the spurious modes have been investigated obtaining smoother admittance results increasing the periodicity of the structure. Moreover, following the same objective, other solutions such as the spacers have been analyzed obtaining positive results. Finally, to optimize the $k_t^2$ by design, a CLMR, which exploit both $d_{33}$ and $d_{31}$ piezoelectric coefficient, has been designed by founding the optimal $T_{AlScN}/\lambda$ ratio and, at the same time, the optimal electric coverage has been found. Moving to 3D simulations, besides matching the results with the previous simulations, the impact of the additional parameters associated to the third dimension has been investigated and a new design has been developed. Then, most of the efforts have been put on the investigation of the transverse spurious modes that, thanks to the introduction of the piston mode and gap holes, have been strongly reduced. Once terminated the simulation analysis and defined a new 3D reference design in all its aspect, some process flow modification have been considered. First of all, a valid process for the definition of a release area confinement for front side release has been developed. This has led to the addition of two masks to the process: the first for the definition and filling of high aspect ratio trenches, and the second to preserve these trenches during the etching steps. Concerning the other test, the ion beam etching has been tried to remove the AlScN. The obtained result is less positive than expected since, requiring an hard mask, it did not manage to allow a simplification of the process flow. However it represent a valid alternative to the plasma etching actually performed and could potentially ease the process in case of thinner piezoelectric layer will be used in future. As a final step, the layout has been designed and studied in every aspect to exploit the potentiality of the ASML DUV stepper, and the both a primary cell and a test cell have been designed. Finally, through direct laser writing, the reticle has been fabricated enabling the possibility of a complete fabrication of the device.

## 6.1 Future improvements

This thesis has completely developed a new design, reticle and process flow for UHF applications. Despite the effectiveness of the various fabrication step has been verified (or it has been done in the past), some work still has to be done. First of all the complete process flow (which is actually on going) has to be completed and the device characterized exploiting the RF probes of the network analyzer. Then, thanks to the measurements, it will be possible to confirm or discuss the results obtained from the simulations and to determine the best design choices. Moreover, many other solution should be investigated. For the simulation part, the "spacers" solution should be considered also in the 3D case in order to understand their effective behaviour. Moreover, the spurious modes behaviour in presence of the holes in the gap has to be deeply analyzed in order to find the optimal configuration for the spurious modes attenuation. Then, having comprehended the best possible design configuration and the trade-off associated to the various parameters, it will be interesting to insert all those features in the smallest pitch layout where the use of optical proximity corrections (OPC) might be needed. Concerning the fabrication, due to the complexity for the realization of the trenches for release area confinement, the possibility of a backside release can be explored. Finally, to have a high performances device, the quality factor and the various source of losses have to be investigated. In this way many solutions can be proposed inducing an improvement of the device. Hence, a lot of work still has to be done to realize an high performance UHF device, but this thesis managed to do a considerable step in that direction.

# Bibliography


[1] P. Delbos D. Damianos J.Mouly. *Status of the MEMS Industry 2021, Market and Technology Report 2021.* URL: https://s3.i-micronews.com/uploads/2021/07/YINTR21180-Status-of-the-MEMS-Industry-2021_Sample.pdf (cit. on p. 1).

[2] J. Bausells L. G. Villanueva and J. Brugger. *Grand challenge in n/mems, Frontiers in Mechanical Engineering.* 2016 (cit. on p. 1).

[3] J. Clement. *Global mobile data traffic from 2017 to 2022.* URL: https://www.statista.com/statistics/271405/global-mobile-data-traffic-forecast/ (cit. on pp. 1, 2).

[4] R. Ruby. *A Snapshot in Time: The Future in Filters for Cell Phones.* URL: https://ieeexplore.ieee.org/document/7153041 (cit. on pp. 2, 3).

[5] R. Gruenwald. *RF Power Handling of SAW Devices.* URL: https://www.richardsonrfpd.com/docs/rfpd/SAW_Devices_Paper.pdf (cit. on p. 3).

[6] H. Campanella. *Thin-film bulk acoustic wave resonator-FBAR: Fabrication, heterogeneous integration with CMOS technology and sensor applications.* URL: https://www.tdx.cat/bitstream/handle/10803/5357/hcp1de1.pdf;sequence=1 (cit. on p. 3).

[7] Qorvo Inc. *Advanced BAW Filter Technology and Its Impact on 5G.* URL: https://www.microwavejournal.com/articles/34455-advanced-baw-filter-technology-and-its-impact-on-5g (cit. on p. 3).

[8] A. Lozzi. *AlN and AlScN contour mode resonators for MEMS-based RF front ends.* 2019 (cit. on pp. 3, 7–11, 14).

[9] wikiwand. *Thin-film bulk acoustic resonator.* URL: https://www.wikiwand.com/en/Thin_film_bulk_acoustic_resonator (cit. on pp. 4, 5).

[10] H. Campanella. *Thin-film bulk acoustic wave resonator - FBAR : fabrication, heterogeneous integration with CMOS technology and sensors applications.* Universided autonoma de Barcelona (UAB), 2007 (cit. on pp. 4, 5).

[11] G. Piazza; P. J. Stephanou; A. P. Pisano. *Piezoelectric Aluminum Nitride Vibrating Contour-Mode MEMS Resonators*. URL: https://ieeexplore.ieee.org/document/4020287 (cit. on p. 6).

[12] Andrea Lozzi, Marco Liffredo, Ernest Ting-Ta Yen, Jeronimo Segovia-Fernandez, and Luis Guillermo Villanueva. «Evidence of Smaller 1/F Noise in AlScN-Based Oscillators Compared to AlN-Based Oscillators». In: *Journal of Microelectromechanical Systems* 29.3 (2020), pp. 306–312. DOI: 10.1109/JMEMS.2020.2988354 (cit. on p. 6).

[13] G. Piazza; P. J. Stephanou; A. P. Pisano. *One and two port piezoelectric higher order contour-mode MEMS resonators for mechanical signal processing*. URL: https://www.sciencedirect.com/science/article/pii/S0038110107003413 (cit. on p. 7).

[14] Yunhong Hou, Meng Zhang, Guowei Han, Chaowei Si, Yongmei Zhao, and Jin Ning. «A review: aluminum nitride MEMS contour-mode resonator». In: *Journal of Semiconductors* 37.10 (Oct. 2016), p. 101001. DOI: 10.1088/1674-4926/37/10/101001. URL: https://doi.org/10.1088/1674-4926/37/10/101001 (cit. on p. 7).

[15] G.Graziano. *Internship report:Modeling and characterization of AlScN microresonator for 5G application*. EPFL, 2021 (cit. on pp. 8, 14, 19, 51).

[16] G. Piazza. *Contour-Mode Aluminum Nitride Piezoelectric MEMS Resonators and Filters*. Springer New York Heidelberg Dordrecht London: Springer, 2013 (cit. on p. 9).

[17] S. Moradian R. Abdolvand H. Fatemi. *Piezoelectric MEMS Resonators-Chapter 5*. Springer, 2017 (cit. on pp. 12, 13).

[18] F.Bersano. *Design and optimization of one and two ports Two-Dimensional Mode Resonators for wide band RF applications*. Politecnico di Torino, 2020 (cit. on p. 13).

[19] A.S. Nowick. *Anelastic relaxation in crystalline solids*. Elsevier, 2012 (cit. on p. 14).

[20] Kenneth E. Wojciechowski Darren W. Branch and Roy H. Olsson III. *Elucidating the Origin of Spurious Modes in Aluminum Nitride Microresonators Using a 2-D Finite-Element Model*. URL: https://www.researchgate.net/publication/262111586_Elucidating_the_Origin_of_Spurious_Modes_in_Aluminum_Nitride_Microresonators_Using_a_2-D_Finite-Element_Model (cit. on p. 15).

[21] M. A. Moram and S. Zhang. «ScGaN and ScAlN: emerging nitride materials». In: *J. Mater. Chem. A* 2 (17 2014), pp. 6042–6050. DOI: 10.1039/C3TA14189F. URL: http://dx.doi.org/10.1039/C3TA14189F (cit. on p. 15).

[22] Ferenc Tasnádi, Björn Alling, Carina Höglund, Gunilla Wingqvist, Jens Birch, Lars Hultman, and Igor A. Abrikosov. «Origin of the Anomalous Piezoelectric Response in Wurtzite $Sc_xAl_{1-x}\mathbf{N}$ Alloys». In: *Phys. Rev. Lett.* 104 (13 Apr. 2010), p. 137601. DOI: 10.1103/PhysRevLett.104.137601. URL: https://link.aps.org/doi/10.1103/PhysRevLett.104.137601 (cit. on p. 15).

[23] Morito Akiyama, Kazuhiko Kano, and Akihiko Teshigahara. «Influence of growth temperature and scandium concentration on piezoelectric response of scandium aluminum nitride alloy thin films». In: *Applied Physics Letters* 95 (2009), p. 162107 (cit. on pp. 15, 16).

[24] Vitor R. Manfrinato, Lihua Zhang, Dong Su, Huigao Duan, Richard G. Hobbs, Eric A. Stach, and Karl K. Berggren. «Resolution Limits of Electron-Beam Lithography toward the Atomic Scale». In: *Nano Letters* 13.4 (2013), pp. 1555–1558 (cit. on p. 16).

[25] Garry J. Bordonaro. «DUV Photolithography and Materials». In: *Encyclopedia of Nanotechnology*. Ed. by Bharat Bhushan. Dordrecht: Springer Netherlands, 2012, pp. 590–604. ISBN: 978-90-481-9751-4. DOI: 10.1007/978-90-481-9751-4_370. URL: https://doi.org/10.1007/978-90-481-9751-4_370 (cit. on p. 17).

[26] P.J. Croux. *DUV lithography for VHF resonator*. EPFL, 2021 (cit. on pp. 18, 68, 82).

[27] Cristian Cassella, Yu Hui, Zhenyun Qian, Gwendolyn Hummel, and Matteo Rinaldi. «Aluminum Nitride Cross-Sectional Lamé Mode Resonators». In: *Journal of Microelectromechanical Systems* 25.2 (2016), pp. 275–285. DOI: 10.1109/JMEMS.2015.2512379 (cit. on p. 38).

[28] Jie Zou, Chih-Ming Lin, Anming Gao, and Albert P. Pisano. «The Multi-Mode Resonance in AlN Lamb Wave Resonators». In: *Journal of Microelectromechanical Systems* 27.6 (2018), pp. 973–984. DOI: 10.1109/JMEMS.2018.2867813 (cit. on pp. 38, 42).

[29] Albert P. Pisano Zou Lin Jie Lin. *High-Performance Aluminum Nitride Lamb Wave Resonators for RF Front-End Technology*. URL: https://escholarship.org/uc/item/9v995545#main (cit. on p. 39).

[30] Jie Zou, Jiansong Liu, and Gongbin Tang. «Transverse Spurious Mode Compensation for AlN Lamb Wave Resonators». In: *IEEE Access* 7 (2019), pp. 67059–67067. DOI: 10.1109/ACCESS.2019.2908340 (cit. on pp. 49, 50, 53, 54).

[31] Jie Zou, Jiansong Liu, Gongbin Tang, Chih-Ming Lin, and C. S. Lam. «Transverse mode suppression in the AlN lamb wave resonators by “piston mode”». In: *2017 IEEE International Ultrasonics Symposium (IUS)*. 2017, pp. 1–4. DOI: 10.1109/ULTSYM.2017.8092899 (cit. on p. 53).

[32] M. Solal, J. Gratier, R. Aigner, K. Gamble, B. Abbott, T. Kook, A. Chen, and K. Steiner. «A method to reduce losses in buried electrodes RF SAW resonators». In: *2011 IEEE International Ultrasonics Symposium*. 2011, pp. 324–332. DOI: 10.1109/ULTSYM.2011.0078 (cit. on p. 55).

[33] A. B. Auld. *Acoustic fields and waves in solids*. Wiley-Interscience, New York, 1973 (cit. on p. 58).

[34] Andrea Lozzi, Annalisa De Pastina, Luis Guillermo Villanueva, and Ernest Ting-Ta Yen. «Release area confinement in Contour mode resonators». In: *2017 IEEE International Ultrasonics Symposium (IUS)*. 2017, pp. 1–4. DOI: 10.1109/ULTSYM.2017.8092032 (cit. on p. 61).

[35] R James, Y Pilloux, and H Hegde. «Reactive ion beam etching of piezoelectric ScAlN for bulk acoustic wave device applications». In: *Journal of Physics: Conference Series* 1407.1 (Nov. 2019), p. 012083. DOI: 10.1088/1742-6596/1407/1/012083. URL: https://doi.org/10.1088/1742-6596/1407/1/012083 (cit. on p. 67).